QUANTUM THEORY OF ELECTRON TRANSPORT THROUGH PHOTO-SYTHETIC PORPHYRINS

Mohammed Deia Noori

B.Sc, M.Sc.

Department of Physics, Lancaster University, UK

Ph.D. Thesis

This thesis is submitted in partial fulfilment of the requirements for the degree of Doctor of Philosophy

July 2017

Declaration

Except where stated otherwise, this thesis is a result of the author's original work and has not been submitted in whole or in part for the award of a higher degree elsewhere. This thesis documents work carried out between October 2013 and March 2017 at Lancaster University, UK, under the supervision of Prof. Colin J. Lambert and funded by the Ministry of Higher Education and Scientific Research (MOHESR) of Iraq in partnership with Thi-Qar University-Iraq.

Mohammed Deia Noori

July 2017

I would like to dedicate my thesis to the

memory of my late beloved mother

Abstract

Optoelectronic properties of metallo-porphyrins play a central role in photosynthesis and are therefore crucial to life on earth. This thesis presents a series of studies into the electronic and thermoelectric properties of various families of molecular junction of metallo-porphryins

Two main techniques will be included in the theoretical approach; Density Functional Theory, which is implemented in the SIESTA code, and the Green's function formalism of electron transport (Chapter 2), which is implemented in the GOLLUM code. Both techniques are used extensively to study a family of metallo-porphyrin molecules.

In this thesis, I cover three main results in the areas of electical and thermoelectrical properties of metallo-porphyrin molecular wires, in which a Co, Ni, Cu, or Zn metal ion in the center of the porphyrin skeleton is coordinated to pyridyl moieties attached to gold electrodes and demonstrate that the current-perpendicular-to-the-plane (CPP) electrical conductances of the series of Ni, Co, Cu or Zn-5,15-diphenylporphyrins increase with the atomic weight of the divalent metal ion. This supramolecularly wired arrangement with the aromatic plane perpendicular to the current is stable at room temperature and provides a unique family of high-conductance molecular wires, whose electrical transport properties can be tuned by metal substitution. I deal with the thermoelectric properties of the same metallo-porphyrin junction (CPP) in chapter four, where I demonstrate that varying the transition metal-centre of a porphyrin molecule allows the molecular energy levels to be tuned relative to the Fermi energy of the electrodes thereby creating the ability to optimise the thermoelectric properties of metallo-porphryins. In chapter six I compare thermoelectric

properties of three zinc porphyrin (ZnP) dimers and a ZnP monomer. The results show that the “edge-over-edge” dimer formed from stacked ZnP rings possesses a highest room-temperature ZT ever reported for an organic material.

Acknowledgments

Nothing would have been completed in this thesis without the collaboration, the help and guidance of many people. All my gratitude goes to my supervisor **Prof. Colin J. Lambert** for his continuous guidance and the intensive fruitful discussion over these years. I would like to thank Dr. Hatef Sadeghi, Dr.Steve Baily and Dr. Iain Grace for their continues support.

I would like also to thank my sponsor, the Ministry of Higher Education and Scientific Research (MOHESR) in Iraq, Thi-Qar University for funding my PhD study. I would like to thank the collaborating experimental groups, Prof. Ismael Díez-Pérez and Dr. Nadim Darwish from University of Barcelona for their successful experiments. I would like to thank all my friends and colleagues in Colin's group, especially Dr. Qusiy Al-Galiby, Dr. David Manrique, Dr. Laith Algharagholy, Dr. Sara Sangtarash, Alaa, Nasser, Ali, Zain, Michel and Qinqqing.

Many gratitude and unlimited thanks to my family. My father, you have done a lot to me, I hope you are proud and satisfied of me and I wish one day I will be able to serve you. My dear wife, many thanks for your support during my study. You were really very kind and without your support, I would not be able to complete the PhD study. My daughters Ayia and Zainab, you are my hope in life; I hope to be a good father to you and support you with a good life. Finally, a big thanks to my brother Sermed and sisters for the support and encouragement I received from them.

Above all, my great thanks to ALLAH for his mercy and blessing.

Mohammed

List of Publications

During my PhD studies I published the following journal articles:

1. Garcia, D., Rodriguez, L., Angeles Herranz, M., Peña, D., Guitian, E., Bailey, S.W.D., Al-Galiby, Q., **Noori, M**., Lambert, C.J., Perez, D., Martin, N. "AC 60-aryne building block: synthesis of a hybrid all-carbon nanostructure." Chemical Communications 52.40 (2016): 6677-6680.

2. **Noori Mohammed,** Albert C. Aragonès, Nadim Darwish, Steven W. D. Bailey, Qusiy Al-Galiby, Iain Grace, Lluïsa Pérez-García‖, David B. Amabilino, Arántzazu Gonzalez-Campo, Ismael Díez-Pérez, and Colin J. Lambert. "Tuning the electrical conductance of metalloporphyrin supramolecular wires". Scientific Reports, 6. (2016).

3. **Mohammed Noori**, Hatef Sadeghi and Colin J. Lambert. "High-performance thermoelectricity in edge-over-edge zinc-porphyrin molecular wires", Nanoscale 9.16 (2017): 5299-5304.

4. **Mohammed Noori**, Hatef Sadeghi, Qusiy Al-Galiby, Steven W. D. Bailey, and Colin J. Lambert "High cross-plane thermoelectric performance of metallo-porphyrin molecular junctions" Physical Chemistry Chemical Physics,(2017).

Abbreviations

ME	Molecular Electronics
DFT	Density Functional Theory
STM-BJ	Scanning Tunneling Microscopy Break Junctions
MCBJ	Mechanically Controllable Break Junctions
M-E-M	Electrode-Molecule-Electrode
TE	Thermal-electronic material
DPP	Diphenyl porphyrin
LDA	Local density approximation
GGA	Generalized gradient approximation
vdW-DF	Van der Waals density functional
DZ	Double-ξ basis set
DZP	Double- ξ polarized basis set
SIESTA	(Spanish Initiative for Electronic Simulations with Thousands of Atoms)
LCAO	Linear Combination of Atomic Orbital
BSSE	Basis set superposition error correction
CP	Counterpoise correction
DOS	Density of states
CIP	Current in plane
CPP	Current perpendicular to the plane

Contents

Chapter 1

1.1 Introduction

Molecular electronics is a branch of nanotechnology, which extends over chemistry, physics, biology and material science and its scope is involved in the study of the electronic and thermal transport properties of devices in which single molecules or assemblies of them are used as a basic building block[1]. The idea of using single molecules in electronic devices, started with theoretical research in the1970s[2], but only recently has it attracted intense scientific interest.

Molecular electronics is based on exploiting molecules as fundamental units in electronic devices which can be connected to each other efficiently and in a controllable way. In addition to their ultimately small size, they have the potential to be fast and cheap electronic circuit elements with very low power consumption. Therefore, single molecule devices are very appealing candidates for future applications.

Molecular electronics is a multi-disciplinary field which includes elements of both physics and chemistry and a combination of theory and experiment working side-by-side is needed to design and enhance future devices. Experimental groups across the world use a variety of measurement techniques (e.g. Scanning Tunneling Microscopy Break Junctions (STM-BJ) and Mechanically Controllable Break Junctions MCBJ[3,4]) to study the molecule's electronic properties. But the main problem is due to the simple fact that the size of the molecules makes it unclear to experimentalists what exactly is being measured and how the molecule is orientated or connected to the electrodes. This can be resolved by modeling the structure using Density Functional Theory (DFT) and providing an explanation of the experimental data from theoretical calculations. A second approach to theory is that it can give predictions about the molecular structure before the experiment is carried out, to determine whether a particular molecule might be suitable. Theoretical and experimental investigations have focused on electrode-molecule-electrode (EME) junctions, which will be discussed in this thesis and the main experimental technique used to study these systems is the (STM-BJ). The ability to control electron transport through a single molecule is considered to be a crucial task in this field[5-7]. Most studies in molecular electronics have focused on two-electrodes devices[8-11].

Also the ability to manage waste heat is a major challenge, which currently limits the performance of information technologies. To address this challenge, there is a need to develop novel materials and device concepts coupled with new strategies for managing and scavenging on-chip waste heat. A major target of current research is the development of new high-efficiency and low-cost thermoelectric materials and devices. Thermoelectric materials, which allow highly-efficient heat-to-electrical-energy conversion from otherwise wasted

low-level heat sources, would have enormous impact on global energy consumption. Nanoscale structures are very promising in this respect, due to the fact that transport takes place through discrete energy levels. The ability to measure thermopower in nanoscale junctions opens the way to developing fundamentally new strategies for enhancing the conversion of heat into electric energy[12].

The current focus is on finding molecules with required properties and finding ways to get reliable and reproducible contacts by major improvements in device fabrications methods. Among different organic molecules, porphyrins were an obvious class of organic molecules to investigate for molecular electronic functions[13]. Pophyrins, metallo-porphyrins, and their derivatives are prime candidates for a host of molecular electronics applications. As a class of molecule, they possess distinctive, reversible oxidation and reduction chemistry that potentiates their use as wires, switches, transistors, junctions, and photodiodes[14-16]. There is a large amount of theoretical investigation of the electronic properties of porphyrin via density functional theory (DFT)[17-25]. Also significant experimental work using both the STM method[26-33] and the STM-BJ method[34-38] has been carried out. There are also many theoretical and experimental studies that have investigated the thermoelectronic properties of the porphyrin molecule[39-44].

The work described in this thesis is based on the electronic and thermoelectric properties of porphyrins. Therefore the next few sections will introduce briefly information about porphyrins.

1.2 Basic structure of Porphyrin

The name porphyrin originated from the ancient Greek word porphura that was used to describe the colour purple (or royal purple)[45]. The parent porphyrin is porphin(e), and substituted porphin(e) is called porphyrin. Porphyrins are a group of organic compounds, the chemistry of porphyrins and related compounds dates back to eighteenth century. The first effort in giving names and directions for drawing the different isomers of porphyrins was made by Hans Fischer[46].

The basic structure of the porphyrin molecule has in common a substituted aromatic macrocyclic ring consisting of four pyrrole rings linked by methine bridges. The four pyrrole units after linking with each other give a planar structure to the porphyrin molecules with an extended conjugated 18 π-electron system being responsible for the aromatic behaver of porphyrins[47-49]. The presence of highly conjugated 18 π-electron systems is responsible for the intense color and other distinctive electronic and redox properties of porphyrins[50]. Figure (1.1) shows the structure of the porphyrin and the numbering of the ring positions .

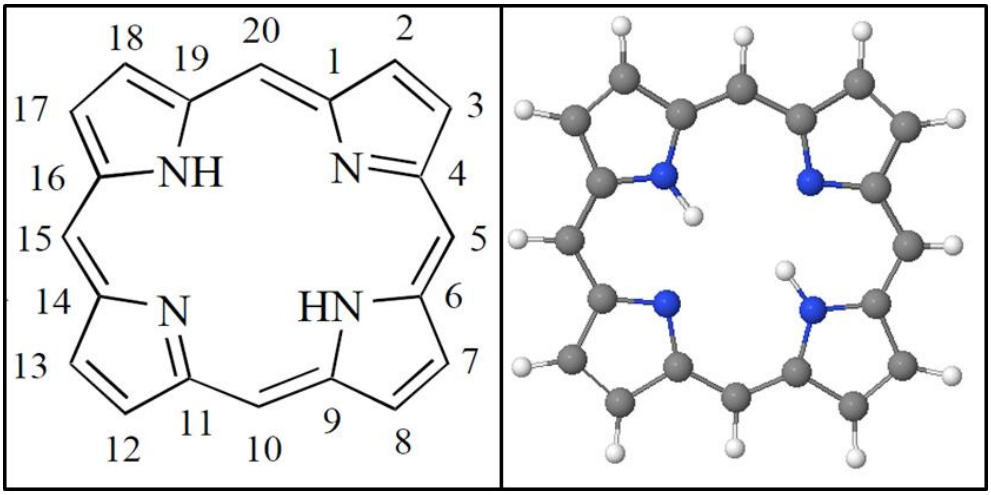

Figure 1.1 *The structure of porphyrin. Left: Molecular structure with numbering of atoms in porphyrin macrocycle, Right: 3D structure, gray: carbon, white: Hydrogen and blue: Nitrogen.*

Two distinct patterns of substituents are illustrated in figure 1. The *meso*-positions are numbered 5,10,15,20 and the *Beta*-positions are 2,3,7,8,12,17,18 [51].

The main theme in the synthesis of porphyrin is the arrangement of diverse substituents in specific patterns about the periphery of the macrocycle. The synthetic control over these substituents enables the porphyrin to be designed and tailored for specific applications.

On the basis of pattern of substituents attached to the macrocycle, porphyrin can be classified into two main categories as shown in Fig.1.2 [52]. The first one is meso-substituted porphyrins and the second is *Beta*-substituted porphyrins. The substituents at the meso-position can be alkyl, aryl, heterocyclics or organometallic groups as well as other porphyrin rings. *M*eso-substituted porphyrins are more attractive compared to the naturally occurring beta-substituted porphyrins for different applications, because of ease of synthesis and their amenability towards synthetic modifications[53-55].

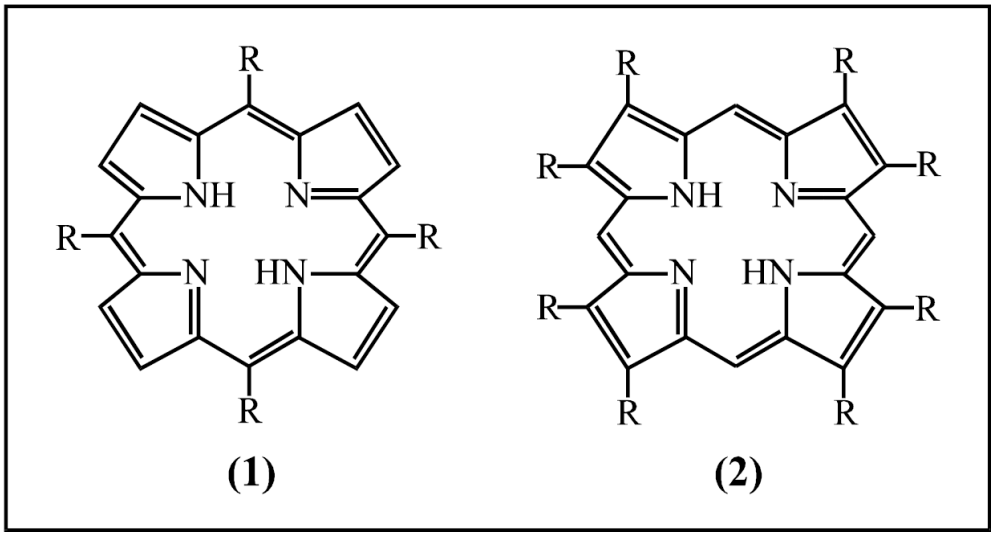

Figure 1.2 *meso*-substituted porphyrin (1) and *Beta* –substituted porphyrin (2)

One of the most well-known *meso*-substituted porphyrins is Diphenylporphyrin (DPP)[56]. DPP was first reported in 1968 by Treibs and Haberle[57].

In addition to substitution on the periphery of the core, porphyrins can be metallated at the center to give another dimension of modularity[58] in which the central core is coordinated by suitable metals; porphyrins. These are called metallo-porphyrins, as shown in Fig.1.3. whereas porphyrin in which no metal is inserted in its cavity is called a free-base porphyrin.

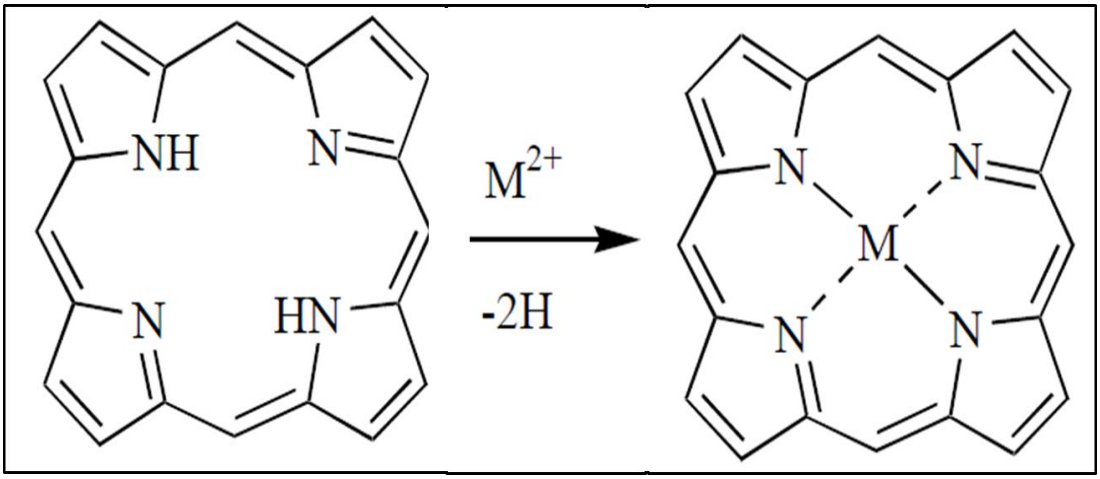

Figure 1.3 *Scheme formation of metallo-porphyrins, M is the incorporated metal atom.*

1.3 Metallo-porphyrins

The formation of metallo-porphyrins is due to the ability of free-base porphyrins to complex a huge variety of metal ions[59,60]. The size of porphyrin macrocycle cavity is perfect to bind metal ions such as Zn, Fe, Ni, and Co etc, forming metallo-porphyrins[61,62]. A large variety of metallo-porphyrins could be synthesized by the insertion of metals into the center of the porphyrin cavity, however circumstances can prevail when binding metal ions, due to the size of the incorporated metal, the molecule might not remain planar, but can be distorted[63]. Porphyrin, and its metal derivatives are of considerable spectroscopic interest because of their simplicity and unique nature of this chemistry[64].

Metallo-porphyrins have become a wide-ranging research area, which is attention-grabbing and worthwhile for research in different scientific fields[65-70].

1.4 Thesis outline

This thesis will report a theoretical study of the electrical and thermoelectrical properties of families of metallo-porphyrin molecules. To begin with, **chapter 2** gives a brief overview of density functional theory (DFT) which is used in this thesis to study and understand the electronic properties of single-molecule junctions. **Chapter 3** describes the single particle Green's function based scattering theory, and related topics such as the Landauer formula, Green's function of infinite leads. Examples of scattering calculations and a general approach to solving the surface lead Green's function are also presented.

In chapter 4 I present a study of the electrical conductance of metallo-porphyrins in a perpendicular junction and compute their electronic conductance through a DFT calculation. In **chapter 5** I introduce theoretical study thermoelectric properties of the same junction. In **chapter 6** the thermoelectrical properties for three different dimer zinc porphyrin and monomer has been studied. Finally, chapter 7 presents conclusions and future works.

Bibliography

1. Zotti, L.A., Kirchner, T., Cuevas, J.C., Pauly, F., Huhn, T., Scheer, E. and Erbe, A., 2010. Revealing the Role of Anchoring Groups in the Electrical Conduction Through Single-Molecule Junctions. small, 6(14), pp.1529-1535.
2. Aviram, A. and Ratner, M.A., 1974. Molecular rectifiers. Chemical Physics Letters, 29(2), pp.277-283.
3. R. Huber, M.T. González, S. Wu, M. Langer, S. Grunder, V. Horhoiu, M. Mayor, M.R. Bryce, C. Wang, R. Jitchati, Electrical conductance of conjugated oligomers at the single molecule level, Journal of the American Chemical Society 130 (2008) 1080-1084.
4. W. Hong, H. Valkenier, G. Mészáros, D.Z. Manrique, A. Mishchenko, A. Putz, P.M. García, C.J. Lambert, J.C. Hummelen, T. Wandlowski, An MCBJ case study: The influence of π-conjugation on the single-molecule conductance at a solid/liquid interface, Beilstein journal of nanotechnology 2 (2011) 699-713.
5. A. Aviram, M.A. Ratner, Molecular rectifiers, Chemical Physics Letters 29 (1974) 277-283.
6. R.L. Carroll, C.B. Gorman, The genesis of molecular electronics, Angewandte Chemie International Edition 41 (2002) 4378-4400.
7. C. Joachim, J. Gimzewski, A. Aviram, Electronics using hybrid-molecular and mono-molecular devices, Nature 408 (2000) 541-548.
8. J. Chen, M. Reed, A. Rawlett, J. Tour, Large on-off ratios and negative differential resistance in a molecular electronic device, Science 286 (1999) 1550-1552.
9. C. Collier, E. Wong, M. Belohradský, F. Raymo, J. Stoddart, P. Kuekes, R. Williams, J. Heath, Electronically configurable molecular-based logic gates, Science 285 (1999) 391-394.
10. S. Datta, W. Tian, S. Hong, R. Reifenberger, J.I. Henderson, C.P. Kubiak, Current-voltage characteristics of self-assembled monolayers by scanning tunneling microscopy, Physical Review Letters 79 (1997) 2530.

11. R.M. Metzger, Unimolecular electrical rectifiers, Chemical reviews 103 (2003) 3803-3834.
12. L.A. Algharagholy, Q. Al-Galiby, H.A. Marhoon, H. Sadeghi, H.M. Abduljalil, C.J. Lambert, Tuning thermoelectric properties of graphene/boron nitride heterostructures, Nanotechnology 26 (2015) 475401.
13. Shaikh, Ahson Jabbar. "Single Molecule Electronics." (2013).
14. Jurow, Matthew, et al. "Porphyrins as molecular electronic components of functional devices." Coordination chemistry reviews 254.19 (2010): 2297-2310.
15. Kang, B.K., et al., Length and temperature dependence of electrical conduction through dithiolated porphyrin arrays. Chemical Physics Letters, 2005. 412(4-6): p. 303-306.
16. Sedghi, G., et al., Single molecule conductance of porphyrin wires with ultralow attenuation. Journal of the American Chemical Society, 2008. 130(27): p. 8582.
17. Venkataramanan, N.S., et al., Electronic structures and spectra of symmetric meso-substituted porphyrin: DFT and TDDFT—PCM investigations. International Journal of Quantum Chemistry, 2011. 111(10): p. 2340-2351.
18. Liao, M.S. and S. Scheiner, Electronic structure and bonding in metal porphyrins, metal=Fe, Co, Ni, Cu, Zn. Journal of Chemical Physics, 2002. 117(1): p. 205-219.
19. Cho, S., et al., Electron delocalization in various triply linked zinc(II) porphyrin arrays: role of antiaromatic junctions between aromatic porphyrins. Physical Chemistry Chemical Physics, 2011. 13(36): p. 16175-16181.
20. Yamaguchi, Y., Theoretical prediction of electronic structures of fully piconjugated zinc oligoporphyrins with curved surface structures. Journal of Chemical Physics, 2004. 120(17): p. 7963-7970.
21. Noori, Mohammed, et al. "Tuning the electrical conductance of metalloporphyrin supramolecular wires." Scientific Reports 6 (2016).
22. Hirao, Hajime, Sason Shaik, and Pawel M. Kozlowski. "Theoretical analysis of the structural and electronic properties of metalloporphyrin π-cation radicals." The Journal of Physical Chemistry A 110.18 (2006): 6091-6099.
23. Mulya, Fadjar, et al. "Design a better metalloporphyrin semiconductor: A theoretical studies on the effect of substituents and central ions." AIP Conference Proceedings. Eds. Tri Rini Nuringtyas, et al. Vol. 1755. No. 1. AIP Publishing, 2016.

24. Chokbuunpiam, Tatiya, et al. "Molecular structure and electronic properties of porphyrin-thiophene-perylene using quantum chemical calculation." International Journal of Photoenergy 2010 (2010).
25. Sena, Alex MP, Veronika Brázdová, and David R. Bowler. "Density functional theory study of the iron-based porphyrin haem (b) on the Si (111): H surface." Physical Review B 79.24 (2009): 245404.
26. Scudiero, L., D.E. Barlow, and K.W. Hipps, Physical properties and metal ion specific scanning tunneling microscopy images of metal(II) tetraphenylporphyrins deposited from vapor onto gold (111). Journal of Physical Chemistry B, 2000. 104(50): p. 11899-11905.
27. Scudiero, L., et al., Scanning tunneling microscopy, orbital-mediated tunneling spectroscopy, and ultraviolet photoelectron spectroscopy of metal(II) tetraphenylporphyrins deposited from vapor. Journal of the American Chemical Society, 2001. 123(17): p. 4073-4080.
28. Scudiero, L., D.E. Barlow, and K.W. Hipps, Scanning tunneling microscopy,orbital-mediated tunneling spectroscopy, and ultraviolet photoelectron spectroscopy of nickel(II) octaethylporphyrin deposited from vapor. Journal of Physical Chemistry B, 2002. 106(5): p. 996-1003.
29 Deng, W.L. and K.W. Hipps, Tip-sample distance dependence in the STM-based orbital-mediated tunneling spectrum of nickel(II) tetraphenylporphyrin deposited on Au(111). Journal of Physical Chemistry B, 2003. 107(39): p. 10736-10740.
30. Muellegger, S., et al., Spectroscopic STM Studies of Single Gold(III) Porphyrin Molecules. Journal of the American Chemical Society, 2009. 131(49): p. 17740-17741.
31. Majima, Y., et al., Negative differential resistance by molecular resonant tunneling between neutral tribenzosubporphine anchored to a Au(111) surface and tribenzosubporphine cation adsorbed on to a tungsten tip. Journal of the American Chemical Society, 2013. 135(38): p. 14159-14166.
32. Kim, H., et al., Switching and sensing spin states of Co-porphyrin in bimolecular reactions on Au(111) using scanning tunneling microscopy. ACS Nano, 2013. 7(10): p. 9312-9317.

33. Yokoyama, T. and F. Nishiyama, Direct Visualization of Electronic Asymmetry within a Phenyl-Linked Porphyrin Dimer. Journal of Physical Chemistry Letters, 2014. 5(8): p. 1324-1328.
34. Noguchi, Y., et al., Fowler-nordheim tunneling in electromigrated break junctions with porphyrin molecules. Japanese Journal of Applied Physics, Part 1: Regular Papers and Short Notes and Review Papers, 2007. 46(4 B): p. 2683-2686.
35. Aragones, A. C. et al. Highly Conductive Single-Molecule Wires with Controlled Orientation by Coordination of Metalloporphyrins. Nano letters 14, 4751-4756 (2014).
36. Li, Z. and E. Borguet, Determining Charge Transport Pathways through Single Porphyrin Molecules Using Scanning Tunneling Microscopy Break Junctions.Journal of the American Chemical Society, 2012. 134(1): p. 63-66.
37. Li, Z., et al., Quasi-Ohmic Single Molecule Charge Transport through Highly Conjugated meso-to-meso Ethyne-Bridged Porphyrin Wires. Nano Letters, 2012. 12(6): p. 2722-2727.
38. Sedghi, G., et al., Long-range electron tunnelling in oligo-porphyrin molecular wires. Nature Nanotechnology, 2011. 6(8): p. 517-523.
39. Sadeghi, Hatef, Sara Sangtarash, and Colin J. Lambert. "Electron and heat transport in porphyrin-based single-molecule transistors with electro-burnt graphene electrodes." Beilstein journal of nanotechnology 6.1 (2015): 1413-1420.
40. Mohammed Noori, Hatef Sadeghi, Qusiy Al-Galiby and Colin J. Lambert "High cross-plane thermoelectric performance of metallo-porphyrin molecular junctions" Physical Chemistry Chemical Physics (2017).
41. Rincón-García, Laura, et al. "Thermopower measurements in molecular junctions." Chemical Society Reviews 45.15 (2016): 4285-4306.
42. Al-Galiby, Qusiy H., et al. "Tuning the thermoelectric properties of metallo-porphyrins." Nanoscale 8.4 (2016): 2428-2433.
43. Mohammed Noori, Hatef Sadeghi and Colin J. Lambert. "High-performance thermoelectricity in edge-over-edge zinc-porphyrin molecular wires", Nanoscale 9.16 (2017): 5299-5304
44. Suslick, Kenneth S., et al. "The materials chemistry of porphyrins and metalloporphyrins." Journal of Porphyrins and Phthalocyanines 4.4 (2000): 407-413.

45. P.E. McGovern and R. H. Michel, Acc. Chem. Res. 23 (1990) 152.
46. H. Fischer and H. Orth, Die Chemie des pyrrols, Vol III, Akad. Verlag, Leipzig (1940)
47. M. Counterman, The porphyrin, D. Dolphin (Ed), Academic, New York, Vol III, Part A, Physical Chemistry, 1978.
48. L. R. Milgrom, The colours of life: An Introduction to the Chemistry of Porphyrins and Related Compounds, Oxford University Press,1997.
49. M. Counterman, in The porphyrins, Vol.3, Ed, By D. Dolphin Academic Press, New York, 1978, pp. 1-165.
50. W. R. Scheidt, Acc. Chem. Res. 10 (1977) 339.
51. J. S,. Lindsey in 'The porphyrin Handbook' ed. K. M. Kadish, K. M. Smith, and R. Guilard, San Diego, 2000. Vol.1, pp 45-118.
52. Lindsey, J. S., In "The Porphyrin Handbook," (Ed.), Kadish, K. M.; Smith, K. M.; and Guilard, R., San Diego, 2000, Vol. 1, 45-118. (b) Smith, K. M., In "The Porphyrins," Elsevier Press, 1975, 9. (c) Boucher, L. J.; and Katz, J. J., J. Am. Chem. Soc. 1967, 89, 4703.
53. Halime, Z.; Belieu, S.; Lachkar, M.; Roisnel, T.; Richard, P.; and Boitrel, B., Eur. J .Org. Chem. 2006, 5, 1207.
54. Senge, M. O.; Shaker, Y. M.; Pintea, M.; Ryppa, C.; Hatscher, S. S.; Ryan, A.; and Sergeva, Y., Eur. J. Org. Chem. 2010, 2, 237.
55. Lindsey, J. S., Accounts of Chemical Research. 2010, 43, 300.
56. J. B. Kim, A. D. Adler, and F. R. Longo, in 'The Porphyrins', ed. D. Dolphin, 1978, Vol. 1, pp 85-100.
57. A. Treibs and N. Haeberle, Justus Liebigs Ann. Chem. 1968, 718, 183.
58. Sanders, J. K. M.; Bampos, N.; Clyde-Watson, Z.; Darling, S. L.; Hawley, J. C.; Kim, H. –J.; Mak, C. C.; and Webb, S. J., "Axial Coordination Chemistry of Metalloporphyrins. Porphyrin Handbook". 2000, 3, 1.
59. J. W. Buchler, in 'The Porphyrins', ed. D. Dolphin, 1978, Vol. 1, pp 389-483.
60. J. W. Buchler, in 'Porphyrins Metalloporphyrins', 1975, pp 157-231.
61. W. Kaim, B. Schwederski, Bioanorganische Chemie,4th edn. B. G. Teubner, Wiesbaden,2005.

62. J. L. Hoard, Science, 174 (1971) 1295.
63. Chen, Xi. "Local Optoelectronic Properties Of Zinc-Porphyrin/gold Molecular Interfaces." (2014).
64. Preethi, N. "Studies on some metalloporphyrin systems." (2010).
65. Milgrom, L. R.; and Jones, C. C., Chem. Commun. 1988, 9, 576.
66 Ivanisevic, A.; and Ellis, A. B., J. Phys. Chem. B. 1999, 103, 1914.
67. Ivanisevic, A.; Reynolds, M. F.; Burstyn, J. N.; and Ellis, A. B., J. Am.Chem. Soc. 2000, 122, 3731.
68. Adler, A. D., J. Polym. Sci. C. 1970, 29, 73.
69. Fleischer, E. B.; and Krishnamurthy, M., J. Am. Chem. Soc. 1972, 94, 1382.
70. Montanari, F.; and Casella, L., (Ed.), "Metalloporphyrins Catalyzed Oxidations", Kluwer Academic: Boston, 1994.

Chapter 2

Density Functional Theory

2.1 Introduction

The explanation and understanding of electronic properties of molecular wires can be obtained by investigating the behavior of electrons in the wires. This means solving the interacting many-body Schrödinger equation to find the eigenvalues, eigenfunctions, Hamiltonian and overlap matrices of the system. In order to solve this complex equation there are various theoretical and semi empirical techniques which are based on an 'ab-initio' method using fitted parameters with experimental data[1-5]. Density Functional theory (DFT)[6,7] is one of these techniques and is proving to be one of the most successful and promising theories used in physics, chemistry and materials science to compute the electronic structure of the ground state of many body systems[8-12]. The methodology of DFT has been applied to a large variety of systems such as atoms[13], molecules[14] and solids[15]. DFT tends to offer a good balance between calculation quality and the required computational

effort[16]. DFT is a method that calculates the local electronic density at each point in space, rather than attempting to obtain the many-particle wave function.

In this chapter I will present a brief introduction of density functional theory (DFT). I will start by presenting a short overview of DFT with the Born-Oppenheimer approximation, Kohn-Sham equations and exchange and correlation energy. The next section will deal with SIESTA (Spanish Initiative for Electronic Simulations with Thousands of Atoms)[17] that is an implementation of DFT, which I have used widely during my PhD study as a theoretical tool. The final sections will deal with pseudopotential approximations, localised basis sets and finally calculating binding energy using the counter poise method.

2.2 Density Functional theory

(DFT) was first proposed in **[6]** and extended a year later in [**7]**, both papers set out the basic theory of Density Functional theory. DFT is a first principle approach that attempts to predict the properties of a material by using as few approximations as possible. The fundamental problem in an electronic structure calculation is that the electrons in a solid interact not only with atomic nuclei but also with each other. Furthermore, the electrons are correlated. As a consequence, there is no systematic way of finding the exact wave functions of their energy eigenvalues. DFT manages to overcome this problem by writing the equations of motion for the system in terms of the ground-state density n(r), and by obtaining the ground-state density, one can in principle calculate the ground-state energy. The main aim of DFT to accurately describe a system with a number of charged nuclei

surrounded by an electron gas. In quantum theory of solids, both electrons and nuclei are described by Schrödinger equation.

$$\mathrm{H}\Psi(r_1, r_2, \dots, r_N, R_1, R_2, \dots, R_M) = E\Psi(r_1, r_2, \dots, r_N, R_1, R_2, \dots, R_M) \quad (2.2.1)$$

where H is the Hamiltonian operator of a system consisting of M nuclei and N electrons, r_i is the position of the *i-th* electron, and R_I the position of the *I-th* nucleus. A molecule is an excellent example of such a complex many-body system. Generally, the many-body Hamiltonian is constructed as the sum of five terms as follows:

$$H_{Full} = T_{el} + T_{nu} + V_{ee} + V_{nn} + V_{en} \quad (2.2.2)$$

where T_{el} and T_{nu} are the kinetic energy terms for the electron and the nuclei respectively. V_{ee} is the interaction energy terms between all electrons, V_{nn} is the interaction between the nuclei and V_{en} is the interaction between electrons and nuclei. These interactions are described by the Hamiltonian operator which is written as follows:

$$\mathrm{H} = \overbrace{\sum_{i=1}^{N}\left(-\frac{\hbar^2}{2m_i}\nabla_i^2\right)}^{T_{el}} + \overbrace{\sum_{n=1}^{I}\left(-\frac{\hbar^2}{2m_n}\nabla_n^2\right)}^{T_{nu}} + \overbrace{\frac{1}{4\pi\varepsilon_o}\frac{1}{2}\sum_{i=1}^{N}\sum_{i\neq j}^{N}\frac{e^2}{|r_i - r_j|}}^{V_{ee}} + \overbrace{\frac{1}{4\pi\varepsilon_o}\frac{1}{2}\sum_{I=1}^{M}\sum_{I\neq J}^{M}\frac{1}{|R_I - R_J|}Z_I Z_J e^2}^{V_{nn}}$$
$$- \overbrace{\frac{1}{4\pi\varepsilon_o}\sum_{i=1}^{N}\sum_{I=1}^{M}\frac{1}{|r_i - R_I|}Z_I e^2}^{V_{en}} \quad (2.2.3)$$

here *i* and *j* denote the *N*-electrons while *I* and *J* run over the *M*-nuclei in the system, m_i is the mass of the *i*-th electron, m_n the mass of the I-th nucleus, *e* and Z_I are the electron and nuclear charge respectively. ε_o is the dielectric constant of the vacuum. The position of the

electrons and nuclei are denoted as r_i and R_I respectively. If we can solve the Schrödinger equation, then we will be able to determine most of the physical properties of a system. However, the Schrödinger equation is very difficult to solve (nearly impossible) when the number of atoms become large because the interaction terms in the Hamiltonian cannot be directly uncoupled and independently solved. An approximation has to be applied to enable a separation of the nucleon and electron degrees of freedom to reduce the size of the problem. This is achieved through the Born-Oppenheimer approximation.

2.3 Born-Oppenheimer approximation

Since the mass of the electron is much smaller than that of nuclei, and in terms of their velocities, the nuclei could be considered as classical particles which creates an external potential, and the electrons as quantum particles are subjected to this potential. This concept known as the Born-Oppenheimer approximation[18] assumes the nucleon wave function is independent of the electrons positions, in other words the wave function that describes the full system can be decomposed to a nuclear wave function, and the electrons wave function. We rewrite the wave function in equation (2.2.1) as:

$$\psi(r_N, R_M) = \psi_e(r_N, R_M)\psi_N(R_M) \qquad (2.3.1)$$

Hence we can rewrite in Schrödinger equation (2.2.1) as two separate Schrödinger equations:

$$H_e\psi_e(r_N, R_M) = E_e\psi_e(r_N, R_M) \qquad (2.3.2)$$

and

$$H_N \psi_N(R_M) = E\psi_N(R_M) \qquad (2..3.3)$$

Where $E_e\,(R_M)$ is the ground state energy of the electrons for a given set of nuclei coordinates. The Hamiltonian for the electrons is $H_e = T_{el} + V_{ee} + V_{en}$ and nuclei is $H_N = T_N + V_{nn} + E_e\,(R_M)$. To find the ground state energy of the electrons E_e we need to solve equation (2.3.2). The employment of the Born-Oppenheimer approximation**,** allows the electron and nucleon degrees of freedom to be decoupled. Nevertheless, solving the Schrödinger equation for this system of nucleons and electrons still needs further approximations such as DFT.

2.4 Kohn-Sham Equations

The Kohn-Sham equation provides DFT the ability to solve the many-body problem which describes the interacting system in an external potential as a set of non-interacting particles in a new effective external potential $V_{eff}(r)$. By comparing the result of a non-interacting system and an interacting system, we can find the effective external potential. This means that the original Hamiltonian can be replaced by an effective Hamiltonian of non-interacting particles in an effective external potential, which has the same ground-state density as the original system. This new effective electron potential is identified by comparing the results from a non-interacting system to that of the interacting system. The energy functional is then written as follows:

$$E[n(r)] = F_{KS}[n(r)] + \int V_{ext}(r)\ n(r)\ dr \tag{2.4.1}$$

$$\mathrm{E}[n] = E_K[n] + E_H[n] + E_{xc}[n] + \int V_{ext}(\mathrm{r})\ n(\mathrm{r})\ d\mathrm{r} \tag{2.4.2}$$

where the functional $F_{KS}[n(r)]$ consists of the following three terms: $E_K[n(r)] + E_H[n(r)] + E_{xc}[n(r)]$. The first three terms represent the kinetic energy of electrons in the non-interacting system is described by a functional $E_K[n]$, classical Hartree potential which includes an electron self-interaction term $E_H[n]$ and finally the term $E_{xc}(n)$ which describes the exchange and correlation energy. This contribution to the energy will be explained later.

Let us now suppose that the density is perturbed by a small amount δn(r), this would cause an energy change by amount δE. The expression of this small change can be written as:

$$\delta E = \int \delta n(r)\left[V_{ext}(r) + \frac{\delta E_K}{\delta n(r)} + \frac{\delta E_H}{\delta n(r)} + \frac{\delta E_{xc}}{\delta n(r)}\right]dr \tag{2.4.3}$$

However since the number of electrons in the system is fixed

$$\int \delta n(r)dr = 0 \tag{2.4.4}$$

the quantity in square brackets in equation (2.4.3) is a constant quantity called a Lagrange multipiler, this will be labelled as μ.

In order to describe the non-interacting electron systems through the Kohn-Sham equation, we consider $E_H[n]$ and $E_{xc}(n)$ are equal to zero because the interactions between electrons in this system are equal to zero. Thus μ is given by

$$\mu = V_{ext}(r) + \frac{\delta E_K[n]}{\delta n} \tag{2.4.5}$$

But for interacting system which depend on μ,

$$\mu = V_{eff}(r) + \frac{\delta E_K[n]}{\delta n} \tag{2.4.6}$$

where $V_{eff}(r)$ is

$$V_{eff}(r) = V_{ext}(r) + \frac{\delta E_H[n]}{\delta n} + \frac{\delta E_{xc}[n]}{\delta n} \tag{2.4.7}$$

By using this potential, we can write down a single particle Hamiltonian

$$H_{KS} = E_K + V_{eff}\ (r) \tag{2.4.8}$$

The corresponding Schrodinger equation is

$$H_{KS}\psi^{K.S} = E\psi^{K.S} \tag{2.4.9}$$

Equation (2.4.9) is the Kohn-Sham equation. Density functional theory uses a self-consistent field procedure to obtain the ground state density. For example, let us suppose that this can be accurately determined. The problem is now it cannot be calculated until the correct ground state density is known and the correct density cannot be obtained from the Kohn-Sham wave functions until equation (2.4.9) is solved with the correct density. Therefore we solve this circular problem by carrying out a self-consistent cycle[19-23] as shown in figure 2.1.

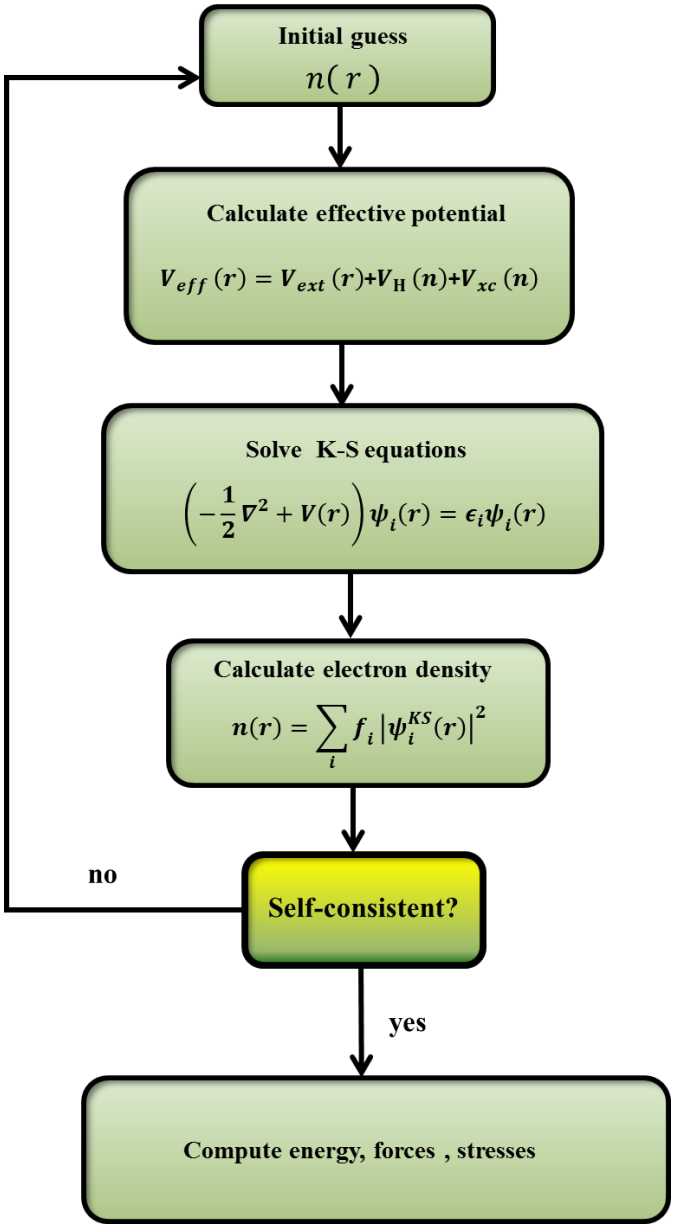

Figure 2.1*: Schematic of the self-consistent DFT cycle starting from an initial density n (r), which is used to calculate the Kohn-Sham potential V_{KS}, Hamiltonian H_e and wave functions ψ_i^{KS} of the system. This allows a new density $n_{new}(r)$ to be calculated, and the cycle is repeated until convergence is achieved.*

2.5 Exchange and correlation energy

In the previous section, we reduced the many-particle Schrödinger equation to a one-particle Schrödinger equation in the framework of the Kohn-Sham equation. The effective potential in the Kohn-Sham equation involves the exchange–correlation potential; the explicit form of the $E_{xc}(n)$ term controls the accuracy of the ground state density and energy. As there is no exact form to evaluate the exchange–correlation potential this leads to approximation methods. There are numerous proposed forms for the exchange and correlation energy in the literature. The first successful and yet simple form was the Local Density Approximation (LDA)[24] which depends only on the density, thus it is a local functional. The LDA is in some sense the simplest form one could imagine for the exchange and correlation energies. It is a simple yet powerful functional and it is known to be accurate for systems where the electron density is not rapidly changing. The first calculations obtaining the correlation energy was performed by Ceperley and Alder using the quantum Monte-Carlo method.

Then the next step was the Generalized Gradient Approximation (GGA)[25]. The GGA extends the LDA by including the derivatives of the density. It contains information about the neighborhood and therefore it is semi-local. The first calculations were proposed by Perdew, Burke and Ernzerhof . One of the latest, and most universal functional is the van der Waals density functional (vdW-DF)[26] which also contains non-local terms.

2.6 SIESTA

SIESTA[17] is an acronym derived from the Spanish Initiative for Electronic Simulations with Thousands of Atoms. . It can be considered as a "theoretical laboratory" to investigate the structures of molecules, and most electrical properties such as charge densities, band structures, and binding energies. SIESTA is a set of methods and a complete software package that can be used to perform DFT calculations on a massive number of atoms (~1000) within a lifetime. It uses the standard Kohn-Sham self-consistent functional method and a Linear Combination of Atomic Orbital Basis set (LCAOB) to perform efficient calculations[27]. All calculations in this thesis were carried out by the implementation of DFT in the SIESTA code. It is used to obtain the relaxed geometry of the discussed structures and to carry out the calculations to investigate their electronic properties.

2.7 Pesudopotential Approximation

Despite all approximations mentioned in previous sections we still need another simplification to solve the many-body Schrödinger equation for practical applications. The electrons in an atom can be split into two types: core and valence, where core electrons lie within filled atomic shells and the valence electrons lie in partially filled shells. Together with the fact that core electrons are spatially localized about the nucleus, only valence electron states overlap when atoms are brought together so that in most systems only valence electrons contribute to the formation of molecular orbitals. This allows the core electrons to be removed and replaced by a pseudopotential such that the valence electrons

feel the same screened nucleon charge as if the core electrons were still present[28-29]. This reduces the number of electrons in a system dramatically and in turn reduces the time and memory required to calculate properties of molecules that contain a large number of electrons.

2.8 Localised Basis Set

In order to perform efficient calculations, SIESTA utilizes Linear Combination of Atomic Orbital (LCAO) basis sets, which are constrained to be zero outside of a certain radius (cut-off radius), and are constructed from the orbitals of the atoms. This produces a sparse form of the Hamiltonian, because the overlap between basis functions is reduced. A LCAO basis set is constructed from the orbitals of the atoms, which enables a minimum size basis set to produce properties close to that of the studied system.

The simplest form of the atomic basis set for an atom is single-ζ, which corresponds to a single basis function per electron orbital and represented in equation (2.8.1)

$$\psi_{nlm}(r) = \phi_{nl}^{1}\mathrm{Y}_{lm}(r) \qquad (2.8.1)$$

Where $\psi_{nlm}(r)$ is the single basis function which consists of a product of one radial wave function, ϕ_{nl}^{1} and one spherical harmonic Y_{lm}. For higher accuracy (multiple-ζ) basis sets with additional radial wave functions can be included for each electron orbital. Further accuracy using multiple-ζ polarised basis sets can be obtained by including wave functions with different angular momenta corresponding to orbitals which are unoccupied in the atom. Table 2.1 shows the number of basis orbitals for a select number of atoms for single-ζ,

single-ζ polarised, double-ζ and double-ζ polarised. Throughout this thesis, I have employed a double- ζ polarized basis set in all SIESTA DFT calculations.

Atoms	SZ	SZP	DZ	DZP
H	1	4	2	5
C	4	9	8	13
N	4	9	8	13
O	4	9	8	13
S	4	9	8	13

Table 2.1: *Table showing the number of radial basis functions per atom as used within the SIESTA for different degrees of precision. For clarity, the specific orbitals are listed below each number, with ~ representing the polarization of that orbital.*

2.9 Calculating binding energy using the counter poise method

Using the DFT approach to calculate the ground state geometry of different system configurations allows us to also calculate the binding energy between different parts of the system. However, these calculations are subject to errors, due to the use of localized basis sets which are centered on the nuclei. If atoms are moved, then the basis set changes so any error arising from the incompleteness of the basis set will also change. One example of these errors is the overlapping basis sets of closed-shell atoms, where this generates synthetic short bond lengths combined with synthetic strong bonding energy which will give an inaccurate total energy of system. In the case of localized basis sets, as used in SIESTA, there is basis set superposition error (BSSE)[30] present and we have to correct for different basis sets of the two configurations. In 1970, Boys and Bernardi proposed a technique to eliminate the BSSE in molecular complexes composed of two geometric configurations so-called the counterpoise correction (CP)[31] scheme.

In figure 2.3 e, d and c represent the two isolated molecules with their individual and corresponding basis functions while the shaded gray atoms in 2.3 a and b represent the ghost states (basis set functions which have no electrons or protons). The BSSE is obtained by recalculating using the mixed basis sets realised by introducing the ghost orbitals, and then subtracting the error from the uncorrected energy to calculate the binding energy $E_{binding}$ givien by:

$$E_{binding} = E_e - (E_a + E_b) \tag{2.9.1}$$

where E_e , E_a and E_b are the total energy of (e) , (a) and (b) systems in figure (2.1) respectively. This is an important concept that has been successfully implemented in many systems to give reliable and realistic results in this thesis.

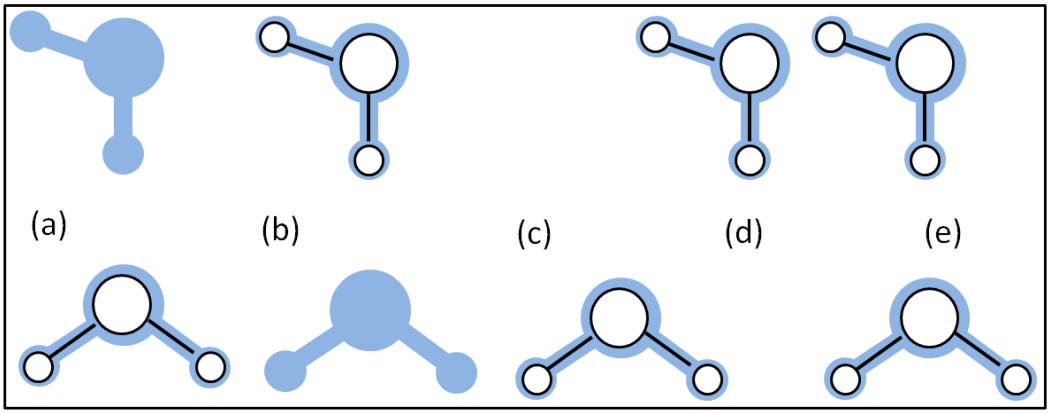

Figure 2.1*: Illustrating the counterpoise method to calculate the binding energy, the empty shapes are basis sets with atoms present and the filled grey shapes are without atoms they are ghost states. (a) and (b) represent the counterpoise correction, (c) and (d) show the basis function for the individual monomers, (e) represents the basis functions for total system.*

Bibliography

1. Pariser, R. and R.G. Parr, A Semi‐Empirical Theory of the Electronic Spectra and Electronic Structure of Complex Unsaturated Molecules. *I.* The Journal of Chemical Physics, 1953. **21**: p. 466.
2. Bingham, R.C., M.J. Dewar, and D.H. Lo, Ground states of molecules. XXVIII. MINDO/3 calculations for compounds containing carbon, hydrogen, fluorine, and chlorine. Journal of the American Chemical Society, 1975. **97**(6): p. 1307-1311.
3. Stewart, J.J., Optimization of parameters for semiempirical methods I. *Method.* Journal of Computational Chemistry, 1989. **10**(2): p. 209-220.
4. Dewar, M.J., et al., Development and use of quantum mechanical molecular models. 76. AM1: a new general purpose quantum mechanical molecular model.Journal of the American Chemical Society, 1985. **107**(13): p. 3902-3909.
5. Finch, C.M., An understanding of the the electrical characteristics of organic molecular devices. 2008, Lancaster University.
6. H Hohenberg and W, Kohn, Phys, Rev, 163, B864 (1964).
7. W. Kohen and L, J, Sham, Phys, Rev, 140, A1133 (1965).
8. Argaman, N. and G. Makov, Density Functional Theory--an introduction. arXiv preprint physics/9806013, 1998.
9. Dronskowski, R., Computational chemistry of solid state materials2005: Wiley Online Library.
10. Eschrig, H., The Fundamentals of Density Functional Theory (revised and extended version). Edition am Gutenbergplatz, Leipzig, Germany, 2003. 9.
11. Parr, R.G. and Y. Weitao, Density-functional theory of atoms and molecules. Vol. 16. 1994: Oxford University Press, USA.
12. Gross, E.K. and R.M. Dreizler, Density functional theory. Vol. 337. 1995: Springer.

13. S. Sanvito, C. J. Lambert, J. H. Jefferson, and A. M. Bratkovsky. General Green's-function formalism for transport calculations with spd hamiltonians and giant magnetoresistance in Co- and Ni-based magnetic multilayers. Phys. Rev. B, 59:11936–11948, May 1999.
14. M P Lopez Sancho, J M Lopez Sancho, J M L Sancho, and J Rubio. Highly convergent schemes for the calculation of bulk and surface Green functions. Journal of Physics F: Metal Physics, 15(4):851, 1985.
15. Wang, J.-S., Wang, J., and Lü, J. T. Quantum thermal transport in nanostructures. Eur. Phys. J. B, 62(4):381–404, 2008.
16. M Ya Amusia, A Z Msezane, and V R Shaginyan. Density functional theory versus the Hartree–Fock method: Comparative assessment. Physica Scripta, 68(6):C133, 2003.
17. Soler, J. M.; Artacho, E.; Gale, J. D.; Garcia, A.; Junquera, J.; Ordejon, P.; Sanchez-Portal, D. The SIESTA method for ab initio order-N materials simulation. J. Phys.: Condens. Matter, 2002. 14(11): p. 2745–2779.
18. M. Born and R. Oppenheimer, Ann. Phys. 84, 457 (1927).
19. Kohn, W. and L.J. Sham, Self-Consistent Equations Including Exchange and Correlation Effects. Physical Review, 1965. 140(4A): p. A1133-A1138.
20. Kohn, W. and L.J. Sham, Self-consistent equations including exchange and correlation effects1965: APS.
21. March, N.H., *Self-consistent fields in atoms.* 1975.
22. Lima, N., L. Oliveira, and K. Capelle, Density-functional study of the Mott gap in the Hubbard model. EPL (Europhysics Letters), 2007. 60(4): p. 601.
23. Eschrig, H., K. Koepernik, and I. Chaplygin, Density functional application to strongly correlated electron systems. Journal of Solid State Chemistry, 2003. **176**(2): p. 482-495.
24. Ceperley, D.M. and B.J. Alder, Ground State of the Electron Gas by a Stochastic Method. Physical Review Letters, 1980. 45(7): p. 566-569.
25. Perdew, J.P., K. Burke, and M. Ernzerhof, Generalized gradient approximation made simple. Physical review letters, 1996. 77(18): p. 3865.

26. M. Dion, H. Rydberg, E. Schröder, D. C. Langreth, and B. I. Lundqvist, _Van der Waals Density Functional for General Geometries,_ Physical Review Letters, vol. 92, pp. 22_25, June 2004.
27. Soler, J.M., et al., The SIESTA method for ab initio order-N materials simulation. Journal of Physics: Condensed Matter, 2002. 14(11): p. 2745.
28. Hamann, D., M. Schlüter, and C. Chiang, Norm-conserving pseudopotentials. Physical Review Letters, 1979. 43(20): p. 1494-1497.
29. Troullier, N. and J.L. Martins, Efficient pseudopotentials for plane-wave calculations. Physical Review B, 1991. 43(3): p. 1993.
30. Visontai, D., I. Grace, and C. Lambert, Electron transport through ribbonlike molecular wires calculated using density-functional theory and Green's function formalism. Physical review b, 2010. **81**(3): p. 035409.
31. Milani, A., et al., *Charge Transfer and Vibrational Structure of sp-Hybridized Carbon Atomic Wires Probed by Surface Enhanced Raman Spectroscopy*. The Journal of Physical Chemistry C, 2011. **115**(26): p. 12836-12843.
32. Kaliginedi, V., et al., Correlations between molecular structure and singlejunction conductance: A case study with oligo (phenylene-ethynylene)-type wires. Journal of the American Chemical Society, 2012. **134**(11): p. 5262-5275.
33. Manrique, D.Z., Theoretical analysis and design in molecular electronics, in *physics* 2011, Lancaster University. p. 240.
34. Oroszlány, L., et al., *Nonthermal broadening in the conductance of double quantum dot structures.* Physical Review B, 2007. **76**(4): p. 045318.

Chapter 3

Single Particle Transport

3.1 Introduction

One of the significant issues in molecular electronic is how to connect the molecule to metallic or semi-metallic electrodes. In principle, the molecule could be coupled to the electrodes with a weak or strong coupling strength. However, in most cases the coupling is weak. Such a system involves scattering processes either from the junction to the leads or inside the molecule itself. There are different approaches to study the electronic and vibrational properties of such junctions. In this thesis I will use the Green's function formalism.

In this chapter, I will start with a brief overview of the Landauer formula. Next, I will introduce the simplest form of a retarded Green's function for a one-dimensional tight binding chain. Following this, I will break the periodicity of this lattice at a single connection and show that the Green's function is related directly to the transmission

coefficient across the scattering region. The methods used on these simple systems will then be used to derive the transmission coefficient of mesoscopic conductors of arbitrarily complex geometry. The method that is presented in this chapter assumes negligible interaction between carriers and the absence of inelastic processes. The thermoelectroric properties and phonon transmission will be introduced in the last section.

3.2 Landauer Formula

The Landauer formula[1,2] is the standard way to describe transport phenomena in ballistic mesoscopic systems and is applicable for phase coherent systems, where a single wave function is sufficient to describe the electronic flow. The final result is a formula which relates the conductance of system to the S-matrix of a scattering region attached to two semi-infinite leads.

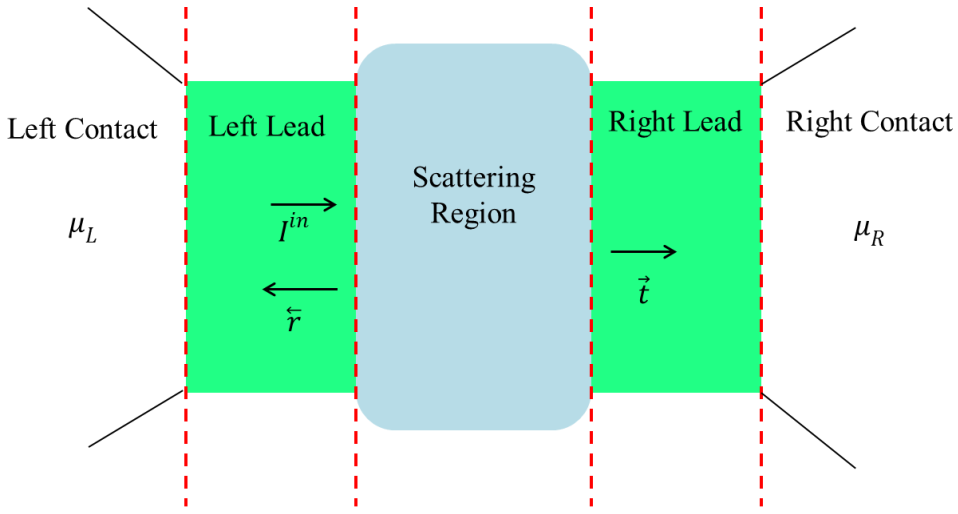

Figure 3.1: *A mesoscopic scatterer connected to contacts by ballistic leads. The chemical potentials in the left and right contacts are μ_L and μ_R respectively. If an incident wave packet hits the scatterer from the left, it will be transmitted to the right with probability T and reflected with probability R.*

To briefly introduce the main ideas behind this formula let us start by consider a mesoscopic scatterer connected to the two contacts, which behave as electron reservoirs, by means of two ideal ballistic leads (Figure 3.1). All inelastic relaxation processes are limited to the reservoirs[3]. The reservoirs have slightly different chemical potentials $\mu_L > \mu_R \Longrightarrow \mu_L - \mu_R = e\delta V > 0$, which will drive electrons from the left to the right reservoir. For one open channel the zero temperature incident electric current (δI^{in}) generated by the chemical potential difference:

$$\delta I^{in} = e v_g \frac{\partial n}{\partial E} (\mu_L - \mu_R) \tag{3.2.1}$$

here, e is the electronic charge, v_g is the group velocity and $\partial n/\partial E$ is the density of states (DOS) per unit length in the lead in the energy window defined by the chemical potentials of the contacts. Since the system is considered one dimensional, we can write:

$$\frac{\partial n}{\partial E} = \left(\frac{\partial n}{\partial k}\frac{\partial k}{\partial E}\right) = \frac{1}{h v_g} \tag{3.2.2}$$

by this and after including a factor 2 for spin, equation (3.2.1) becomes:

$$\delta I^{in} = \frac{2e}{h}(\mu_L - \mu_R) = \frac{2e^2}{h}\delta V \tag{3.2.3}$$

where δV is the voltage associated with the chemical potential mismatch. From equation (3.2.3), it is clear that in the absence of a scattering region (ideal periodic system) the conductance of a quantum wire with one open channel is $G_0 = 2e^2/h$ which is approximately $7.75 \times 10^{-5} S$ (or in other words, a resistance of $12.9 k\Omega$). This is reasonable quantity; it typically appears on the circuit boards of everyday electrical appliances.

Now if we consider a scattering region, the current is partially reflected with a probability $R = |r|^2$ and partially transmitted with a probability $T = |t|^2$ the current collected in the right contacts (δI^{out}) will be:

$$\delta I^{out} = \delta I^{in}\, T = \frac{2e^2}{h}\, T\, \delta V \Longrightarrow \frac{\delta I^{out}}{\delta V} = G = \frac{2e^2}{h}\, T \tag{3.2.4}$$

This is the well-known Landauer formula, relating the conductance *G*, of a mesoscopic scatterer to the transmission probability (T) of the electrons traveling through it. It describes the linear response conductance, hence it only holds for small bias voltages, $\delta V \approx 0$. To calculate the conductance in multi-channel system - for the case of more than one open channel- the Landauer formula has been generalized by Büttiker[2]. In this case the transmission coefficient is replaced by the sum of all the transmission amplitudes which describe electrons incoming from the left contact and arriving to the right contact. Landauer formula (equation (3.2.4)) for the multi-open channels hence becomes:

$$\frac{\delta I^{out}}{\delta V} = G = \frac{2e^2}{h} \sum_{ij} \left|t_{ij}\right|^2 = \frac{2e^2}{h} Trace\ (tt^{\dagger}) \tag{3.2.5}$$

where t_{ij} is the transmission amplitude describing scattering from the j^{th} channel of the left lead to the i^{th} channel of the right lead. Similarly, the reflection amplitudes r_{ij} which describe scattering processes where the particle is scattered from the j^{th} channel of the left lead to the i^{th} channel of the same lead. By combining reflection and transmission amplitudes one can obtain an object which is called the S matrix, it connects states coming from the left lead to the right lead and vice versa:

$$S = \begin{pmatrix} r & t' \\ t & r' \end{pmatrix} \tag{3.2.6}$$

here r and t describe electrons coming from the left, while r' and t' describe electrons coming from the right in equation (3.2.5) r, t, r' and t' are complex matrices for more than one channel, which due to charge conservation satisfy $SS^{\dagger} = I$.

3.3 One-Dimension

In order to calculate transport properties it is first necessary to describe a perfect wire. I am going to use the Green's function technique to obtain the transmission coefficient, so I will first discuss the form of the Green's function for a simple one dimensional discrete lattice (section 3.3.1) and then move on to calculate the scattering matrix of a one-dimensional scatterer (section 3.3.2).

3.3.1 Perfect One-Dimensional infinite chain

In this section I will discuss the form of the Green's function for a simple infinite one-dimensional chain with on-site energies (ε_o) and real hopping parameters ($-\gamma$) as shown in Figure 3.2. I am going to consider a simple tight binding approach (as done in [3-10]) to get a qualitative understanding of electronic structure calculations in periodic systems.

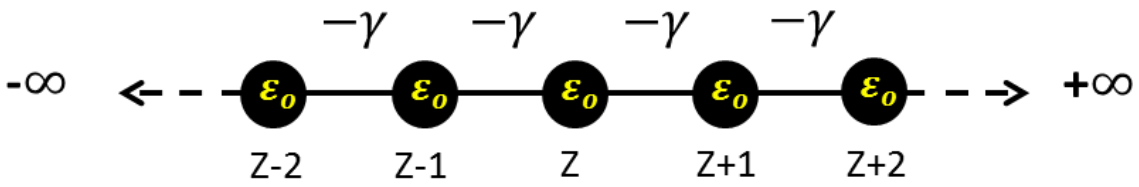

Figure 3.2*: Tight-binding model of a one-dimensional periodic lattice with on-site energies ε_o and couplings $-\gamma$.*

Before we calculate the Green's functions, let us solve the Schrödinger equation to obtain the wave functions of the whole system. The Hamiltonian in our simple one-dimensional tight binding model has the matrix form as:

$$H = \begin{pmatrix} \ddots & -\gamma & & \\ -\gamma & \varepsilon_0 & -\gamma & \\ & -\gamma & \varepsilon_0 & -\gamma \\ & & -\gamma & \ddots \end{pmatrix} \tag{3.3.1}$$

According to the time independent Schrödinger equation (Eq.3.3.2) which can be expanded at a lattice site (*z)* in terms of the energy and wave function $\Psi_{(z)}$ (Eq.3.3.3).

$$H\Psi = \mathrm{E}\Psi \;\rightarrow\rightarrow (\mathrm{E} - \mathrm{H})\Psi = 0 \tag{3.3.2}$$

Now we can write out the Schrödinger equation for row z of the Hamiltonian (H), as:

$$\varepsilon_o \Psi_{(z)} - \gamma \Psi_{(z+1)} - \gamma \Psi_{(z-1)} = E\Psi_{(z)} \tag{3.3.3}$$

The wave function for this perfect lattice takes the form of propagating Bloch state (equation (3.3.4)), normalised by its group velocity υ_g, in order for it to carry unit current flux. The substitution of this into equation (3.3.3) leads to the well-known one-dimensional dispersion relation (equation (3.3.5)).

$$\Psi_{(z)} = \frac{1}{\sqrt{v_g}} e^{ikz} \tag{3.3.4}$$

$$E = \varepsilon_o - 2\gamma \cos k \tag{3.3.5}$$

where (k) refers to the wavenumber. The retarded Green's function $g(z, z')$ is closely related to the wave function and is in fact the solution to an equation very similar to that of the Schrödinger equation:

$$(E - H)\, g(z, z') = \delta_{z,z'} \tag{3.3.6}$$

here $\delta_{z,z'}$ is kronecker delta $\delta_{z,z'} = 1, \;\; if\; z = z'$ and $\delta_{z,z'} = 0, \quad if\; z \neq z'$

Physically, the retarded Green's function, $g(z,z')$, describes the response of a system at a point z due to an excitation (source) at a point z'. Intuitively, we expect such an excitation to give rise to two waves, traveling outwards from the point of excitation, with amplitudes A^+ and A^- as shown in Figure 3.3

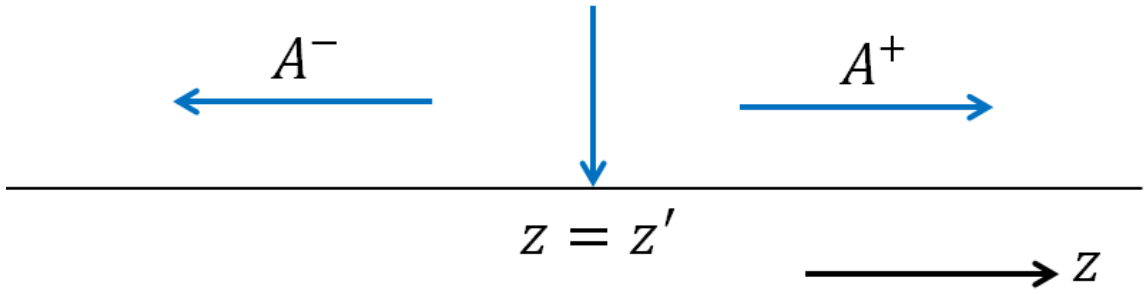

Figure 3.3: *shows the retarded Green's function of an infinite one-dimensional lattice. The source (excitation point) at $z = z'$ causes the wave to propagate left and right with amplitudes $A-$ and $A+$ respectively.*

These waves can be expressed simply as:

$$g(z,z') = \begin{cases} A^+ e^{ikz}, & z > z' \\ A^- e^{-ikz}, & z < z' \end{cases} \tag{3.3.7}$$

This solution satisfies equation (3.3.6) at every point, except at $z = z'$. To overcome this, the Green's function must be continuous (equation (3.3.7)), so we equate the two at $z = z'$:

$$[g(z,z')]_{z=z'-} = [g(z,z')]_{z=z'+} \tag{3.3.8}$$

$$A^+ e^{ikz'} = A^- e^{-ikz'} \rightarrow A^- = A^+ e^{2ikz'} \tag{3.3.9}$$

To find the solution, we write

$$A^{+} = \beta e^{-ikz'} \tag{3.3.10}$$

$$A^{-} = \beta e^{ikz'} \tag{3.3.11}$$

From Eqs (3.3.7) and (3.3.8) we get

$$\mathcal{g}(z,z') = \beta e^{ik|z-z'|} \tag{3.3.12}$$

To obtain the constant β, we use Eq. (3.3.6) which for $z = z'$ gives

$$(\varepsilon_0 - E)\beta - \gamma\beta e^{ik} - \gamma\beta e^{ik} = -1$$

$$\gamma\beta\left(2cosk - 2e^{ik}\right) = -1$$

$$\beta = \frac{1}{2i\gamma sink} = \frac{1}{ihv} \tag{3.3.13}$$

where the group velocity, found from the dispersion relation equation (3.3.5) , is:

$$v_g = \frac{1}{\hbar}\frac{\partial E(k)}{\partial k} = \frac{2\gamma sink}{\hbar} \tag{3.3.14}$$

Finally, we can simply write down the retarded Green's function for the one dimensional chain[4-6,11]. A more thorough derivation can be found in the literature [3,12,13].

$$\mathcal{g}^{R}(z,z') = \frac{1}{i\hbar v_g} e^{ik|z-z'|} \tag{3.3.15}$$

The above retarded Green's function describes electrons energy from a source at z' . If the two waves incoming from left and right inter the point z', so z$'$ is a sink not a source, then the corresponding Green's function is called the advanced Green's function and is the complex conjugate of $\mathcal{g}^{R}(z,z')$

3.3.2 One-Dimensional Scattering

In this section I will consider two one-dimensional tight binding semi-infinite leads connected by a coupling element ($-\alpha$). Both leads have equal on-site potentials (ε_o) and hopping elements ($-\gamma$) as shown in figure 3.4. as done in [9,10 and 14-17]. I will derive the transmission and reflection coefficients for a particle traveling from the left lead towards the scattering region. This simple problem is important, because it turns out that all scattering processes can be reduced to this topology of one-dimensional setups.

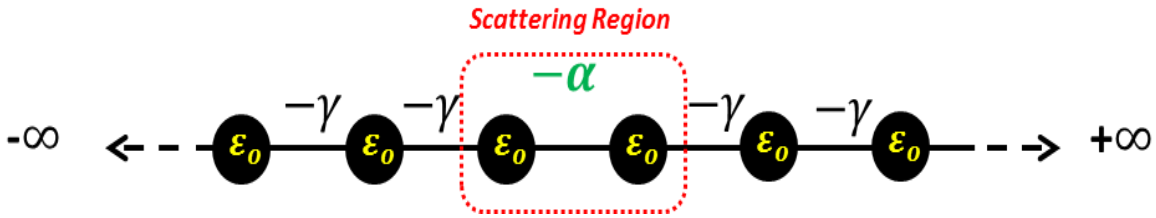

Figure 3.4: *Simple tight-binding model of a one dimensional scatterer attached to one dimensional leads.*

First, we note that the Hamiltonian, takes the form of an infinite matrix.

$$H = \begin{pmatrix} \ddots & -\gamma & & \\ -\gamma & \varepsilon_0 & -\alpha & \\ & -\alpha & \varepsilon_0 & -\gamma \\ & & -\gamma & \ddots \end{pmatrix} = \begin{pmatrix} H_L & V_c \\ V_c^{\dagger} & H_R \end{pmatrix} \tag{3.3.16}$$

here, $H_L$and H_R denote Hamiltonians for the leads which are the semi-infinite equivalent of the Hamiltonian shown in equation (3.3.16) and $V_c = -\alpha$ denotes the coupling parameter.

For real γ, the dispersion relation corresponding to the leads introduced above was given in equation (3.3.5) and the group velocity was given in equation (3.3.14). In order to obtain the scattering amplitudes we need to calculate the Green's function of the system which satisfies:

$$(E - H)G = I \tag{3.3.17}$$

The retarded Green's function for an infinite, one dimensional chain with the same parameters is defined in equation (3.3.15):

$$g^{\infty}_{z,,z'} = \frac{1}{i\hbar v_g} e^{ik|z-z'|} \tag{3.3.18}$$

In order to obtain the Green's function of a semi-infinite lead we need to introduce the appropriate boundary conditions. In this case, if the lattice is semi-infinite, and the chain terminates at a given point $(z_o - 1)$ then the Greens function for site (z_o) is zero. Therefore, we expected that the Green's function for the semi-infinite chain is the Green's function of an infinite one-dimensional chain adding a wave function which reflected from the boundary. The wave function in this case is ($g_{z,z'} = g^{\infty}_{z,z'} + \Psi^{z_o}_{z,z'}$)

where

$$\Psi^{z_o}_{z,z'} = -\frac{e^{ik(2z_o - z - z')}}{i\hbar v_g} \tag{3.3.19}$$

This vanishes at $z = z_o$ for any z' and has the following simple form at the boundary $(z = z' = z_o - 1)$:

$$\mathcal{g}_{z_o-1,z_o-1} = -\frac{e^{ik}}{\gamma} \tag{3.3.20}$$

If we consider the case of decoupled leads ($\alpha = 0$) the total Green's function of the system will simply be given by the decoupled Green's function:

$$\mathcal{g} = \begin{pmatrix} -\frac{e^{ik}}{\gamma} & 0 \\ 0 & -\frac{e^{ik}}{\gamma} \end{pmatrix} = \begin{pmatrix} \mathcal{g}_L & 0 \\ 0 & \mathcal{g}_R \end{pmatrix} \tag{3.3.21}$$

If we now switch on the interaction, then in order to obtain the Green's function of the coupled system (G). Dyson's equation is required:

$$G = (\mathcal{g}^{-1} - V)^{-1} \tag{3.3.22}$$

here the operator V describing the interaction connecting the two leads will have the form:

$$V = \begin{pmatrix} 0 & V_c \\ V_c^{\dagger} & 0 \end{pmatrix} = \begin{pmatrix} 0 & -\alpha \\ -\alpha & 0 \end{pmatrix} \tag{3.3.23}$$

The solution to Dyson's equation, equation (3.3.23) reads:

$$G = \frac{1}{\gamma^2 e^{-2ik} - \alpha^2} \begin{pmatrix} -\gamma e^{-ik} & -\alpha \\ -\alpha & -\gamma e^{-ik} \end{pmatrix} \tag{3.3.24}$$

Now we can calculate the transmission (t) and the reflection (r) amplitudes from the Green's function equation (3.3.24). This is done by making use of the Fisher-Lee relation[1,18] which relates the scattering amplitudes of a scattering problem to the Green's function of the problem. The Fisher-Lee relations in this case read:

$$r = G_{1,1} i\hbar v_g - 1 \tag{3.3.25}$$

and

$$t = G_{1,2} i\hbar v_g e^{ik} \tag{3.3.26}$$

These amplitudes correspond to particles incident from the left. Similar expressions could be used for the transmission ($\overleftarrow{t}'$) and reflection ($\vec{r}'$) amplitudes for the particles are travelling from the right. Based on these coefficients, the probability is defined as: $T = |t|^2$, $T' = |t'|^2$, $R = |r|^2$ and $R' = |r'|^2$.

Since we are now in the possession of the full scattering matrix, so we can use the Landauer formula equation (3.5) to calculate the zero bias conductance. The above procedure by which this analytical solution for the conductance of a one-dimensional scatterer was found can be generalized for more complex geometries.

To sum up the previous steps, the first step was to calculate the Green's function describing the surface sites of the leads and then the total Green's function in the presence of a scatterer is obtained by Dyson's equation. After that the Fisher-Lee relation gives us the scattering matrix from the Green's function. Finally, and by using the Landauer formula, we can then find the zero-bias conductance.

3.4 Generalization of the Scattering Formalism

In this section I will show a generalized the above approach to transport calculations following the derivation of Lambert *et al.*, presented in [4-7]. This is similar to the previous approach. First the surface Green's function of crystalline leads is computed, then the technique of decimation is introduced to reduce the dimensionality of the scattering region and finally the scattering amplitudes are recovered by means of a generalization of the Fisher-Lee relation.

3.4.1 Hamiltonian and Green's Function of the Leads

In general, a lead is a perfect crystalline object that acts as a perfect wave-guide for carrying excitations from reservoirs to the scattering region. In this section we study a general semi-infinite crystalline electrode of arbitrary complexity. Because the leads are crystalline, the structure of the Hamiltonian is a generalization of the one-dimensional electrode Hamiltonian in equation (3.3.1). Figure 3.5 shows the general system.

Instead of site energies, we have a Hamiltonian for each repeating layer of the bulk electrode (H_o), and a coupling matrix to describe the hopping parameters between these layers (H_1). The Hamiltonian for such a system has the form:

$$H = \begin{pmatrix} \ddots & H_1 & 0 & 0 \\ H_1^\dagger & H_0 & H_1 & 0 \\ 0 & H_1^\dagger & H_0 & H_1 \\ 0 & 0 & H_1^\dagger & \ddots \end{pmatrix} \tag{3.4.1}$$

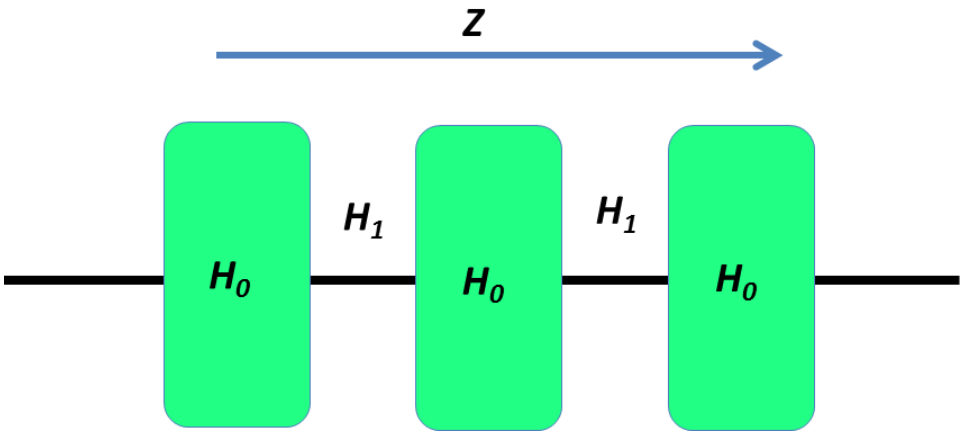

Figure 3.5: *Schematic representation of a semi-infinite generalized lead. States described by the Hamiltonian H_o are connected via a generalized hopping matrix H_1. The direction z is defined to be parallel to the axis of the chain. One can assign for each slice a label z.*

where H_o and H_1 are in general complex matrices and the only restriction is that the full Hamiltonian (H) should be Hermitian. The main aim of this section is to calculate the Green's function of such a lead for general H_1 and H_o. In order to be able to calculate the Green's function one has to calculate the spectrum of the Hamiltonian by solving the Schrödinger equation of the lead:

$$H_1^{\dagger}\Psi_{(z-1)} + H_o\Psi_{(z)} + H_1\Psi_{(z+1)} = E\Psi_{(z)} \qquad (3.4.2)$$

Here $\Psi_{(z)}$ is the wave function describing layer z. We assume the system is infinitely periodic in the z direction only, so the on-site wave function $\Psi_{(z)}$, can be represented in Bloch form; consisting of a product of a propagating plane wave and a wave function ($\Phi_{(k)}$),

which is perpendicular to the transport direction (z). If the layer Hamiltonian (H_o), has dimensions $M \times M$ (or in other words consists of M site energies and their respective hopping elements), then the perpendicular wave function ($\Phi_{(k)}$), will have M degrees of freedom and take the form of a $1 \times M$ dimensional vector. Therefore the wave function $\Psi_{(z)}$, takes the form:

$$\Psi_{(z)} = \sqrt{n_{(k)}} e^{ikz} \Phi_{(k)} \tag{3.4.3}$$

where, n_k is an arbitrary normalization parameter. Substituting this into the Schrödinger equation (equation (3.4.2)) gives:

$$(H_o + e^{ik} H_1 + e^{-ik} H_1^{\dagger} - E)\Phi_{(k)} = 0 \tag{3.4.4}$$

Typically, to find the band structure for such a problem, one would select values of k and calculate the eigenvalues $[E = E_l(k)]$, where $l = 1, \ldots \ldots, M$. Here, l denotes the band index. For each value of k, there will be M solutions to the eigenvalue problem, and so M energy values. In this way, by selecting successive values for k, it is straight forward to build up a band structure.

In a scattering problem, the problem is approached from the opposite direction; instead of finding the values of E at a given k, we find the values of k at a given E. In order to accomplish this, a root-finding method might have been used, but this would have required an enormous numerical effort since the wave numbers are in general complex. Instead, we

can write down an alternative eigenvalue problem in which the energy is the input and the wave numbers are the result by introducing the function:

$$\theta_{(k)} = e^{-ik}\Phi_{(k)} \rightarrow \Phi_{(k)} = e^{ik}\theta_{(k)} \tag{3.4.5}$$

and combining it with equation (3.4.4):

$$\begin{pmatrix} H_1^{-1}(H_0 - E) & -H_1^{-1}H_1^{\dagger} \\ I & 0 \end{pmatrix}\begin{pmatrix} \Phi_k \\ \vartheta_k \end{pmatrix} = e^{ik}\begin{pmatrix} \Phi_k \\ \vartheta_k \end{pmatrix} \tag{3.4.6}$$

For a layer Hamiltonian (H_o) of size $M \times M$, equation (3.4.6) will yield $2M$ eigenvalues (e^{ik_l}) and eigenvectors ($\Phi_{(k_l)}$), of size M. We can sort these states into four categories according to whether they are propagating or decaying and whether they are left going $z \longrightarrow -\infty$ or right going $z \longrightarrow \infty$. A state is propagating if it has a real value of k_l, and is decaying if it has an imaginary value of k_l. If the imaginary part of the wave number is positive then we say it is a left decaying state, if it has a negative imaginary part it is a right decaying state. The propagating states are sorted according to the group velocity of the state defined by:

$$v_g^{k_l} = \frac{1}{\hbar}\frac{\partial E_{k,l}}{\partial k} \tag{3.4.7}$$

If the state has positive group velocity ($v_g^{k_l}$), means it is a right propagating state, otherwise it is a left propagating state. To summarise:

Table 3.1*: Sorting the eigenstates into left and right propagating or decaying states according to the wave number and group velocity.*

	Left	**Right**
Decaying	$Im(k_l) > 0$	$Im(k_l) < 0$
Propagating	$Im(k_l) = 0\,, v_g^{k_l} < 0$	$Im(k_l) = 0, v_g^{k_l} > 0$

For convenience, from now on I will denote the wave numbers (k_l) which belong to the left propagating/decaying set of wave numbers by $\bar{k}_l$ and the right propagating/decaying wave numbers will remain plainly k_l. Thus, $\Phi_{(k_l)}$ is a wave function associated to a "right" state and $\Phi_{(\bar{k}_l)}$ is associated to a "left" state. Note that if H_1 is invertible, there must be exactly the same number (M) of left and right going states. It is clear that if H_1 is singular, the matrix in equation (3.4.6) cannot be constructed, since it relies of the inversion of H_1. However, several methods can be used to overcome this problem. The first [**19-20**] uses the decimation technique to create an effective, non-singular H_1. Another solution might be to populate a singular H_1 with small random numbers, hence introducing an explicit numerical error. This method is reasonable as the introduced numerical error can be as small as the numerical error introduced by decimation. Another solution is to rewrite equation (3.4.6) such that H_1 need not be inverted:

$$\begin{pmatrix} H_1^{-1}(H_0 - E) & -H_1^{\dagger} \\ I & 0 \end{pmatrix} \begin{pmatrix} \Phi_k \\ \vartheta_k \end{pmatrix} = e^{ikz} \begin{pmatrix} H_1 & 0 \\ 0 & I \end{pmatrix} \begin{pmatrix} \Phi_k \\ \vartheta_k \end{pmatrix} \tag{3.4.8}$$

However, solving this generalized eigen-problem is more computationally expensive. Any of the aforementioned methods work reasonably in tackling the problem of a singular H_1 matrix, and so can the condition that there must be exactly the same number (M) of left and right going states, whether H_1 is singular or not.

The solutions to the eigen-value equation (3.4.4) at a given wave number (k) will form an orthogonal basis set, however, the eigenstates ($\Phi_{(k_l)}$) obtained by solving the eigen-value equation (3.4.6) at a given energy (E) will not generally form an orthogonal set of states. This is crucial, since we will have to deal with the non-orthogonality when constructing the Green's function. It is, therefore, necessary to introduce the duals to $\Phi_{(k_l)}$ and $\Phi_{(\bar{k}_l)}$ in such a way that they obey:

$$\widetilde{\Phi}^{\dagger}_{(k_i)}\Phi_{(k_j)} = \widetilde{\Phi}^{\dagger}_{(\bar{k}_i)}\Phi_{(\bar{k}_j)} = \delta_{ij} \tag{3.4.9}$$

This yields the generalized completeness relation:

$$\sum_{l=1}^{M} \widetilde{\Phi}^{\dagger}_{(k_l)}\Phi_{(k_l)} = \sum_{l=1}^{M} \widetilde{\Phi}^{\dagger}_{(\bar{k}_l)}\Phi_{(\bar{k}_l)} = I \tag{3.4.10}$$

Once we are in possession of the whole set of eigenstates at a given energy we can calculate the Green's function first for the infinite system and then, by satisfying the appropriate boundary conditions, for the semi-infinite leads at their surface. Since the Green's function satisfies the Schrödinger equation when $z \neq z'$, we can build up the Green's function from the mixture of the eigenstates $\Phi_{(k_l)}$ and $\Phi_{(\bar{k}_l)}$:

$$\mathcal{g}(z,z') = \begin{cases} \sum_{l=1}^{M} \Phi_{(k_l)} e^{ik_l(z-z')}\, \omega_{k_l}^{\dagger}, & z \geq z' \\ \sum_{l=1}^{M} \Phi_{(\bar{k}_l)} e^{i\bar{k}_l(z-z')}\, \omega_{\bar{k}_l}^{\dagger}, & z \leq z' \end{cases} \tag{3.4.11}$$

where the M-component vectors ω_{k_l} and $\omega_{\bar{k}_l}$ are to be determined. It is important to note the structural similarities between this equation and equation (3.3.7) and also that all the degrees of freedom in the transverse direction are contained in the vectors $\Phi_{(k)}$ and ω_k.

The task now is to obtain the ω vectors. As in section 3.3.1, we know that equation (3.4.11) must be continuous at $z = z'$and should fulfill the Green's equation (equation (3.3.6)). The first condition is expressed as:

$$\sum_{l=1}^{M} \Phi_{(k_l)} \omega_{k_l}^{\dagger} = \sum_{l=1} \Phi_{(\bar{k}_l)} \omega_{\bar{k}_l}^{\dagger} \tag{3.4.12}$$

and the second:

$$\sum_{l=1}^{M} \left[(E - H_o)\Phi_{(k_l)} \omega_{k_l}^{\dagger} + H_1 \Phi_{(k_l)} e^{ik_l} \omega_{k_l}^{\dagger} + H_1^{\dagger} \Phi_{(\bar{k}_l)} e^{-i\bar{k}_l} \omega_{\bar{k}_l}^{\dagger} \right] = I$$

$$\sum_{l=1}^{M} \left[(E - H_o)\Phi_{(k_l)} \omega_{k_l}^{\dagger} + H_1 \Phi_{(k_l)} e^{ik_l} \omega_{k_l}^{\dagger} + H_1^{\dagger} \Phi_{(\bar{k}_l)} e^{-i\bar{k}_l} \omega_{\bar{k}_l}^{\dagger} + H_1^{\dagger} \Phi_{(k_l)} e^{-ik_l} \omega_{k_l}^{\dagger} \right.$$

$$\left. - H_1^{\dagger} \Phi_{(k_l)} e^{-ik_l} \omega_{k_l}^{\dagger} \right] = I$$

$$\sum_{l=1}^{N}\left[H_1^{\dagger}\Phi_{(\bar{k}_l)}e^{-i\bar{k}_l}\omega_{\bar{k}_l}^{\dagger}-H_1^{\dagger}\Phi_{(k_l)}e^{-ik_l}\omega_{k_l}^{\dagger}\right]+\sum_{l=1}^{M}\left[(E-H_o)+H_1e^{ik_l}+H_1^{\dagger}e^{-ik_l}\right]\Phi_{(k_l)}\omega_{k_l}^{\dagger}$$

$$=I$$

and since, from the Schrödinger equation (equation (3.4.4)), we know that:

$$\sum_{l=1}^{M}\left[(E-H_o)+H_1e^{ik_l}+H_1^{\dagger}e^{-ik_l}\right]\Phi_{(k_l)}=0 \tag{3.4.13}$$

This yields to:

$$\sum_{l=1}^{N}H_1^{\dagger}\left[\Phi_{(\bar{k}_l)}e^{-i\bar{k}_l}\omega_{\bar{k}_l}^{\dagger}-\Phi_{(k_l)}e^{-ik_l}\omega_{k_l}^{\dagger}\right]=I \tag{3.4.14}$$

Now let us make use of the dual vectors defined in equation (3.4.9). Multiplying equation (3.4.12) by $\widetilde{\Phi}_{(k_p)}$ we get:

$$\sum_{l=1}^{M}\widetilde{\Phi}_{(k_p)}^{\dagger}\Phi_{(\bar{k}_l)}\omega_{\bar{k}_l}^{\dagger}=\omega_{k_p}^{\dagger} \tag{3.4.15}$$

and similarly multiplying by $\widetilde{\Phi}_{(\bar{k}_p)}^{\dagger}$ gives:

$$\sum_{l=1}^{M}\widetilde{\Phi}_{(\bar{k}_p)}^{\dagger}\Phi_{(k_l)}\omega_{k_l}^{\dagger}=\omega_{\bar{k}_p}^{\dagger} \tag{3.4.16}$$

Using the continuity equation (3.4.12) and equations (3.4.15) and (3.4.16), the Green's equation (equation (3.4.14)) becomes:

$$\sum_{l=1}^{M}\sum_{p=1}^{M} H_1^{\dagger}\left(\Phi_{(\bar{k}_l)}e^{-i\bar{k}_l}\widetilde{\Phi}^{\dagger}_{(\bar{k}_l)} - \Phi_{(k_l)}e^{-ik_l}\widetilde{\Phi}^{\dagger}_{(k_l)}\right)\Phi_{(\bar{k}_p)}\omega^{\dagger}_{\bar{k}_p} = I \tag{3.4.17}$$

From which it follow:

$$\sum_{l=1}^{M}\left[H_1^{\dagger}\left(\Phi_{(\bar{k}_l)}e^{-i\bar{k}_l}\widetilde{\Phi}^{\dagger}_{(\bar{k}_l)} - \Phi_{(k_l)}e^{-ik_l}\widetilde{\Phi}^{\dagger}_{(k_l)}\right)\right]^{-1} = \sum_{p=1}^{M}\Phi_{(\bar{k}_p)}\omega^{\dagger}_{\bar{k}_p} = \sum_{p=1}^{M}\Phi_{(k_p)}\omega^{\dagger}_{k_p}$$

(3.4.18)

This immediately gives us an expressions for $\omega_k^{\dagger}$:

$$\omega_k^{\dagger} = \widetilde{\Phi}^{\dagger}_{(k)}\nu^{-1} \tag{3.4.19}$$

where ν is defined as:

$$\nu = \sum_{l=1}^{M} H_1^{\dagger}\left(\Phi_{(\bar{k}_l)}e^{-i\bar{k}_l}\widetilde{\Phi}^{\dagger}_{(\bar{k}_l)} - \Phi_{(k_l)}e^{-ik_l}\widetilde{\Phi}^{\dagger}_{(k_l)}\right) \tag{3.4.20}$$

The wave number (k) in equation (3.4.19) refers to both left and right type of states. Substituting equation (3.4.19) into equation (3.4.11) we obtain the Green's function of an infinite system:

$$\mathcal{g}^{\infty}_{z,z'} = \begin{cases}\sum_{l=1}^{M}\Phi_{(k_l)}e^{ik_l(z-z')}\widetilde{\Phi}^{\dagger}_{(k_l)}\nu^{-1}, & z \geq z' \\ \sum_{l=1}^{M}\Phi_{(\bar{k}_l)}e^{i\bar{k}_l(z-z')}\widetilde{\Phi}^{\dagger}_{(\bar{k}_l)}\nu^{-1}, & z \leq z'\end{cases} \tag{3.4.20}$$

In order to obtain the Green's function for a semi-infinite lead we have to add a wave function to the Green's function in order to satisfy the boundary conditions at the edge of the

lead, as with the one dimensional case. The boundary condition here is that the Green's function must vanish at a given place ($z = z_o$). In order to achieve this we simply add:

$$\Delta = -\sum_{l,p=1}^{M} \Phi_{\bar{k}_l} e^{i\bar{k}_l(z-z_o)} \tilde{\Phi}^{\dagger}_{(\bar{k}_l)} \Phi_{(k_p)} e^{ik_p(z_o-z)} \tilde{\Phi}^{\dagger}_{(k_p)} \nu^{-1} \tag{3.4.21}$$

To the Green's function, equation (3.4.20), $\mathcal{g} = \mathcal{g}^{\infty} + \Delta$. This yields the surface Green's function for a semi-infinite lead going left:

$$\mathcal{g}_L = \left(I - \sum_{l,p=1}^{M} \Phi_{(\bar{k}_l)} e^{-i\bar{k}_l} \tilde{\Phi}^{\dagger}_{(\bar{k}_l)} \Phi_{(k_p)} e^{ik_p} \tilde{\Phi}^{\dagger}_{(k_p)}\right) \nu^{-1} \tag{3.4.22}$$

and going right:

$$\mathcal{g}_R = \left(I - \sum_{l,p=1}^{M} \Phi_{(k_l)} e^{ik_l} \tilde{\Phi}^{\dagger}_{(k_l)} \Phi_{(\bar{k}_p)} e^{-i\bar{k}_p} \tilde{\Phi}^{\dagger}_{(\bar{k}_p)}\right) \nu^{-1} \tag{3.4.23}$$

So now we have a versatile method for calculating the surface Green's functions (equations (3.4.22) and (3.4.23)) for a semi-infinite crystalline electrode using the numerical approach in equation (4.51). The next step is to apply this to a scattering problem.

3.4.2 Effective Hamiltonian of the Scattering Region

The coupling matrix between the surfaces of the semi-infinite leads has been shown in section (3.3.2), additionally, the Dyson equation has been used to calculate the Green's function of the scatterer. However, the scattering region is not generally described simply as a coupling matrix between the surfaces. Therefore, it is useful to use the decimation method

to reduce the Hamiltonian down to such a structure[19,20]. Other methods have been developed [21,22], but in this thesis I will use the decimation method.

Consider again the Schrödinger equation:

$$\sum_j H_{ij}\Psi_j = E\Psi_i \tag{3.4.27}$$

If we separate from the equation (3.4.27) the d^{th} degree of freedom in the system:

$$H_{id}\Psi_d + \sum_{j\neq d} H_{ij}\Psi_j = E\Psi_i \ , \qquad i \neq d \tag{3.4.28}$$

Now we can examine the component Ψ_d, using the latter equation when $i = d$;

$$H_{dd}\Psi_d + \sum_{j\neq d} H_{dj}\Psi_j = E\Psi_d \tag{3.4.29}$$

From equation (3.4.29) we can express Ψ_d as:

$$\Psi_d = \sum_{j\neq d} \frac{H_{dj}\Psi_j}{E - H_{dd}} \tag{3.4.30}$$

If we then substitute equation (3.4.30) into equation (3.4.28) we get:

$$\sum_{j\neq d} \left[H_{ij} + \frac{H_{id}H_{dj}}{E - H_{dd}}\right]\Psi_j = E\Psi_i \ , \qquad i \neq d \tag{3.4.31}$$

So we can think of equation (3.4.31) as an effective Schrödinger equation where the number of degrees of freedom is decreased by one compared to equation (3.4.27). Hence we can introduce a new effective Hamiltonian ($\widetilde{H}$) as:

$$\widetilde{H}_{ij} = H_{ij} + \frac{H_{id}H_{dj}}{E - H_{dd}} \tag{3.4.32}$$

This Hamiltonian is the decimated Hamiltonian produced by simple Gaussian elimination. A notable feature of the decimated Hamiltonian is that it is energy dependent, which suits the method presented in the previous section very well[19]since we are interested in computing all quantities for given values of E without the decimation method, the Hamiltonian describing the system in general would take the form:

$$H = \begin{pmatrix} H_L & V_L & 0 \\ V_L^{\dagger} & H_{scat} & V_R \\ 0 & V_R^{\dagger} & H_R \end{pmatrix} \tag{3.4.33}$$

here, H_L and H_R denote the semi-infinite leads, H_{scatt} denotes the Hamiltonian of the scatterer and V_L and V_R are the coupling Hamiltonians, which couple the original scattering region to the leads. After decimation, we produce an effectively equivalent Hamiltonian:

$$H = \begin{pmatrix} H_L & V_c \\ V_c^{\dagger} & H_R \end{pmatrix} \tag{3.4.34}$$

here, V_c denotes an effective coupling Hamiltonian, which now describes the whole scattering process.

Now we can apply the same steps as with the one-dimensional case; using the Dyson equation (equation (3.3.25)). Hence, the Green's function for the whole system is described by the surface Green's functions (equations (3.4.25) and (3.4.26)) and the effective coupling Hamiltonian from equation (3.4.34):

$$G = \begin{pmatrix} g_L^{-1} & -V_c \\ -V_c^{\dagger} & g_R^{-1} \end{pmatrix}^{-1} = \begin{pmatrix} G_{00} & G_{01} \\ G_{10} & G_{11} \end{pmatrix} \tag{3.4.35}$$

3.5 Breit-Wigner Resonance

To have an idea for the most important features of the transport curves, it would be useful to briefly study about Breit-Wigner distribution. For electrons of energy E passing through single molecule the on resonance transmission coefficient T could be described by a Lorentzian function, via the Breit-Wigner formula:

$$T(E) = \frac{4\Gamma_1\Gamma_2}{(E - \varepsilon_n)^2 + (\Gamma_1 + \Gamma_2)^2} \tag{3.5.1}$$

where T(E) is the transmission coefficient of the electrons, Γ_1 and Γ_2 describe the coupling of the molecular orbital to the electrodes (labeled 1 and 2) and $\varepsilon_n = E - \Sigma$ is the eigenenergy En of the molecular orbital shifted slightly by an amount Σ due to the coupling of the orbital to the electrodes.

This formula shows that when the electron resonates with the molecular orbital (i.e. when $E = \varepsilon_n$), electron transmission is a maximum.

The formula is valid when the energy E of the electron is close to an eigenenergy En of the isolated molecule, and if the level spacing (differences between the eigenenergies of a quantum system) is larger than $(\Gamma_1 + \Gamma_2)$. In the case of a symmetric molecule attached symmetrically to identical leads, $\Gamma_1 = \Gamma_2$, T(E) = 1, on resonance, when $E = \varepsilon_n$.

3.6 Thermoelectric coefficients

Thermoelectricity involves the conversion between thermal and electric energies, since the early of 19th century the connection between heat, current, temperature and voltage have been known with the discovery of the Seebeck, Peltier and Thompson effects. The Seebeck effect describes the production of electrical current due to a temperature difference, whereas the Peltier and Thompson effects describe the heating or cooling of a current carrying conductor[23,24]. A more general system can be considered where there is a temperature ΔT and potential drop ΔV across the system, causing both charge and heat currents to flow. In the linear-response regime, the electric current I and heat current $\dot{Q}$ passing through a device is related to the voltage difference ΔV and temperature difference ΔT by[26,26]

$$\begin{pmatrix} I \\ \dot{Q} \end{pmatrix} = \frac{1}{h} \begin{pmatrix} e^2 L_0 & \frac{e}{T} L_1 \\ e L_1 & \frac{1}{T} L_2 \end{pmatrix} \begin{pmatrix} \Delta V \\ \Delta T \end{pmatrix} \qquad (3.5.1)$$

where T is the reference temperature. Since transport through single molecules is phase-coherent, even at room temperature, the coefficients L_n are given by $L_n = L_n^{\uparrow} + L_n^{\downarrow}$ $(n = 0, 1, 2)$, where:

$$L_n^{\sigma} = \int_{-\infty}^{\infty} (E - E_F)^n \, T^{\sigma}(E) \left(-\frac{\partial f(E,T)}{\partial E} \right) dE \tag{3.5.2}$$

In this expression, $T^{\sigma}(E)$ is the transmission coefficient for electrons of energy E, spin of σ = [↑,↓] passing through the molecule from one electrode to the other[38] and $f(E,T)$ is the Fermi distribution function defined as $f(E,T) = [e^{(E-E_F)/k_B T} + 1]^{-1}$ where k_B is Boltzmann's constant. Equation (3.5.1) can be rewritten in terms of the electrical conductance (G), thermopower (S), Peltier coefficient (∏), and the electronic contribution to the thermal conductance (κ_e):

$$\begin{pmatrix} \Delta V \\ \dot{Q} \end{pmatrix} = \begin{pmatrix} 1/G & -S \\ \prod & \kappa_e \end{pmatrix} \begin{pmatrix} I \\ \Delta T \end{pmatrix} \tag{3.5.3}$$

where

$$G = \frac{2e^2}{h} L_0 \tag{3.5.4}$$

$$S = -\frac{\Delta V}{\Delta T} = -\frac{1}{eT} \frac{L_1}{L_0} \tag{3.5.5}$$

$$\Pi = \frac{1}{e} \frac{L_1}{L_0} \tag{3.5.6}$$

$$\kappa_e = \frac{1}{hT}\left(L_2 - \frac{(L_1)^2}{L_0}\right) \tag{3.5.7}$$

$$\kappa_e \approx L_0^{\sigma} TG, \tag{3.5.8}$$

An important quantity that measures the thermoelectric efficiency of a system is a dimensionless number the figure of merit ZT[27-29]

$$ZT = \frac{S^2 GT}{\kappa} \tag{3.5.9}$$

Equation (3.5.9) shows that ZT is proportional to the square of the Seebeck coefficient (S) and the conductance (G) and inversely proportional to the thermal conductance (κ) , which has mainly two components $\kappa = \kappa_e + \kappa_{phonon}$. ZT determines how efficient it is to transform heat into electricity, ZT has to be as high as possible (closer to one or higher) in order to thermoelectric device to work effectively[30,31]. For the electronic thermoelectric figure of merit is given by[32]:

$$ZT_e = \frac{S^2 G}{\kappa_e}\, T \tag{3.5.10}$$

and by using equation (3.5.2) ZT will be:

$$ZT_e = \frac{(L_1)^2}{L_0 L_2 - (L_1)^2} \tag{3.5.11}$$

For E close to E_F, if T(E) varies only slowly with E on the scale of k_BT then these formulae take the form[33]:

$$G(T) \approx \left(\frac{2e^2}{h}\right) T(E_F), \tag{3.5.12}$$

$$S(T) \approx -\alpha e T \left(\frac{d \ln T(E)}{dE} \right)_{E=E_F}, \quad (3.5.13)$$

where $\alpha = \left(\frac{k_B}{e}\right)^2 \frac{\pi^2}{3}$ is the Lorentz number. Equation (3.5.12) demonstrates that S is enhanced by increasing the slope of ln T(E) near $E=E_F$

3.7 Phonon Transmission and Thermal Conductance

After we obtained relaxed xyz coordinate of the system, from DFT calculations, sets of xyz coordinates were generated by displacing each atom in positive and negative x, y, and z directions by $\delta q'$ The forces in three directions $q_i = (x_i , y_i , z_i)$ on each atom were then calculated by DFT without geometry relaxation. These values of the force $F_i^q = (F_i^x, F_i^y, F_i^z)$ were used to construct the dynamical matrix using the formula:

$$D_{ij} = \frac{K_{ij}^{qq'}}{M_{ij}} \quad (3.6.1)$$

where $K_{ij}^{qq'}$ for $i \neq j$ are obtained from finite differences

$$K_{ij}^{qq'} = \frac{F_i^q(\delta q_j') - F_j^q(-\delta q_j')}{2\delta q_j'} \quad (3.6.2)$$

and the mass matrix $M_{ij} = (M_i M_j)^{1/2}$. To satisfy translational invariance, the K for i = j (diagonal terms) is calculated from $K_{ii} = -\sum_{i \neq j} K_{ij}$. The phonon transmission $T_{ph}(\omega)$ then can be calculated from the relation:

$$T_{ph}(\omega) = Tr(\Gamma_L^{ph}(\omega)G_{ph}^{R}(\omega)\Gamma_R^{ph}(\omega)G_{ph}^{R_\dagger}(\omega) \quad (3.6.3)$$

In this expression, $\Gamma_{L,R}^{ph}(\omega) = i(\sum_{L,R}^{ph}(\omega) - \sum_{L,R}^{ph^\dagger}(\omega))$ describes the level broadening due to the coupling between left (L) and right (R) electrodes and the central scattering region formed from the molecule and closest contact layers of gold, $\sum_{L,R}^{ph}(\omega)$ are the retarded self-frequencies associated with this coupling and $G_{ph}^{R} = (\omega^2 I - D - \sum_{L}^{ph} - \sum_{R}^{ph})^{-1}$ is the retarded Green's function, where D and I are the dynamical and the unit matrices, respectively. The phonon thermal conductance κ_{ph} at temperature T is then calculated from[34]:

$$\kappa_{ph}(T) = \frac{1}{2\pi}\int_0^\infty \hbar\omega T_{ph}(\omega)\frac{\partial f_{BE}(\omega, T)}{\partial T}\, d\omega \quad (3.6.4)$$

where $f_{BE}(\omega, T) = (e^{\frac{\hbar\omega}{K_B T}} - 1)^{-1}$ is Bose–Einstein distribution function, $\hbar$ is reduced Planck's constant, and $k_B = 8.6 \times 10{-}5$ eV/K is Boltzmann's constant.

Bibliography

1. Landauer, R., Spatial variation of currents and fields due to localized scatterers in metallic conduction. IBM Journal of Research and Development, 1957. 1(3): p. 223-231.
2. Büttiker, M., et al., Generalized many-channel conductance formula with application to small rings. Physical Review B, 1985. 31(10): p. 6207.
3. Datta, S., Electronic transport in mesoscopic systems1997: Cambridge university press
4. C. M. Finch. An understanding of electrical characteristics of organic molecular devices. PhD thesis, Lancaster University, 2008.
5. S. Athanasopoulos. Electronic Properties of Hybrid Carbon Nanotubes. PhD thesis, Lancaster University, 2005.
6. S. Sanvito. Giant Magnetoresistance and Quantum Transport in Magnetic Hybrid Nanostructures. PhD thesis, Lancaster University, 1999.
7. L. Oroszlány. Carbon based nanodevices. PhD thesis, Lancaster University, 2009.
8. A. Theodoros Papadopoulos. Quantum Transport in Molecular Wires. PhD thesis,Lancaster University, 2007.
9. L. Algharagholy. Quantum Transport Through Nanoscale Sculpturenes. PhD thesis,Lancaster University, 2013.
10. Q. Al-Galiby. Quantum Theory of Sensing and Thermoelectricity in Molecular Nanostructures. PhD thesis, Lancaster University, 2016.
11. S. Datta. Quantum transport: atom to transistor. 2005.
12. Eleftherios, N. Economou. Green's functions in quantum physics, 1984,Springer.
13. Pier, A. Mello and Narendra Kumar Kumar. Quantum transport in meso-scopic systems: complexity and statistical fluctuations: a maximum-entropy viewpoint, volume 4. Oxford University Press, 2004.
14. T. Pope. Quantum and Classical Dynamics of Molecular-Scale Junctions. PhD thesis, Lancaster University, 2013.
15. K. Gillemot. Quantum Control of electrical and Thermpelecrical transport in Molecular-Scale structures. PhD thesis, Lancaster University, 2013.

16. D. Visontai. Quantum and Classical Dynamics of Molecular Scale Systems.PhD thesis, Lancaster University, 2013.
17. D. Manrique. Theoretical analysis and design in molecular electronics. PhD thesis, Lancaster University, 2011.
18. Fisher, D.S. and P.A. Lee, Relation between conductivity and transmission matrix. Physical Review B, 1981. 23(12): p. 6851-6854.
19. Leadbeater, M. and C.J. Lambert, A decimation method for studying transport properties of disordered systems. Annalen der physik, 1998. 7(5-6): p. 498-502.
20. Lema, F. and C. Wiecko, Multifractality of the Anderson and binary alloy localized eigenstates by the improved decimation method. Physica Scripta, 1993. 47(2): p. 129.
21. J.G. MacKinnon, H. White, Some heteroskedasticity-consistent covariance matrix estimators with improved finite sample properties, Journal of econometrics 29 (1985) 305-325.
22. D. Ryndyk, R. Gutiérrez, B. Song, G. Cuniberti, in: Energy Transfer Dynamics in Biomaterial Systems, (Springer, 2009).
23. S. Kumar, S.D. Heister, X. Xu, J.R. Salvador, G.P. Meisner, Journal of electronic materials, 42 (2013) 665-674.
24. D. Voneshen, K. Refson, E. Borissenko, M. Krisch, A. Bosak, A. Piovano, E. Cemal, M. Enderle, M. Gutmann, M. Hoesch, Nature materials, 12 (2013) 1028-1032.
25. V.M. García-Suárez, R. Ferradás, J. Ferrer, Physical Review B, 88 (2013) 235417.
26. N. Claughton, C. Lambert, Physical Review B, 53 (1996) 6605.
27. García-Suárez, Víctor M., et al. "Redox control of thermopower and figure of merit in phase-coherent molecular wires." Nanotechnology 25.20 (2014): 205402.
28. Cowen, Lewis M., et al. "Review—Organic Materials for Thermoelectric Energy Generation." ECS Journal of Solid State Science and Technology 6.3 (2017): N3080-N3088.
29. M. Noori, H. Sadeghi and Colin J. Lambert "High-performance thermoelectricity in edge-over-edge zinc-porphyrin molecular wires." Nanoscale 9.16 (2017): 5299-5304.

30. García-Suárez, Víctor Manuel, R. Ferradás, and Jaime Ferrer. "Impact of Fano and Breit-Wigner resonances in the thermoelectric properties of nanoscale junctions." Physical Review B 88.23 (2013): 235417.
31. Rincón-García, Laura, et al. "Thermopower measurements in molecular junctions." Chemical Society Reviews 45.15 (2016): 4285-4306.
32. Al-Galiby, Qusiy H., et al. "Tuning the thermoelectric properties of metallo porphyrins." Nanoscale 8.4 (2016): 2428-2433.
33. V.M. García-Suárez, C.J. Lambert, D.Z. Manrique, T. Wandlowski, Nanotechnology, 25 (2014) 205402.
34. Sadeghi, Hatef, Sara Sangtarash, and Colin J. Lambert. "Oligoyne molecular junctions for efficient room temperature thermoelectric power generation." Nano letters 15.11 (2015): 7467-7472.

Chapter 4

Tuning the electrical conductance of metallo-porphyrin supramolecular wires

In this chapter, the electrical conductance of metallo-porphyrins in a perpendicular junction will be examined both theoretically and experimentally. I demonstrate that varying the transition metal-centre of the porphyrin molecule over a range of metallic atoms allows the tuning of the electrical conductance of metallo-porphryins. The results presented in this chapter were published in: Noori M, et al. Tuning the thermoelectric properties of metallo-porphyrins supramolecular wires, 2016, Scientific Reports 6, 37352.

This study is a collaborative work and the experiment has been carried out in the University of Barcelona (Prof. Ismael Díez-Pérez group).

4.1 Introduction

Porphyrins offer a variety of desirable features as building blocks for future molecular-scale devices, including their highly-conjugated structure, rigid planar geometry, high chemical stability and their ability to form metallo-porphyrins by coordinating metal ions in the center of their macrocyclic and aromatic skeleton[1-5]. Following early work, which established their chemical and biological properties[6-9], porphyrins have become a focus of interest both for experimental and theoretical investigations of molecular electronics [10-12] and for the design of complexes using supramolecular chemistry, leading to a diverse array of structures available for nano-scale building blocks[13]. This unique combination of properties is exploited in nature, where for example metallo-porphyrins act as charge carriers in naturally occurring processes such as photosynthesis [14-17] and in the respiratory chain[18, 19]. In many of these processes, the plane of the porphyrin skeleton is stacked perpendicular to the direction of charge transport, whereas previous studies[10-12] address conductance with the plane of the porphyrin skeleton aligned parallel to the direction of charge transport. Further work has studied the "current in plane" (CIP) which is an up-right configuration (figure 4.1a), where the porphyrin skeleton was contacted to gold electrodes via thiol or pyridyl anchor groups and the electrical conductance was found to be low[10, 20] (of order nanosiemens). For the purpose of developing future single-molecule electronics and thermoelectrics, it is highly desirable to increase the electrical conductance, since this can lead to higher switching speeds and reduce the relative effect of parasitic phonons in thermoelectric devices. In what follows I develop a strategy for increasing the electrical conductance of porphyrin-based

single-molecule wires by investigating their conductance with the current perpendicular to the plane (CPP) (figure 4.1b). I report a joint experimental and theoretical study of CPP conductance trends and binding configurations across a family of 5,15-diphenylporphyrins (DPPs), with a centrally-coordinated divalent metal ion of either Co, Ni, Cu or Zn and demonstrate that their conductance and stability can be tuned through the choice of metal atom. This is an extension of previous experimental measurements[21] which showed that the CPP conductance of the flat-laying sandwiches of a Co(II)-DPP shows a large conductance value of three orders of magnitude higher than the measured in-plane conductance [10].

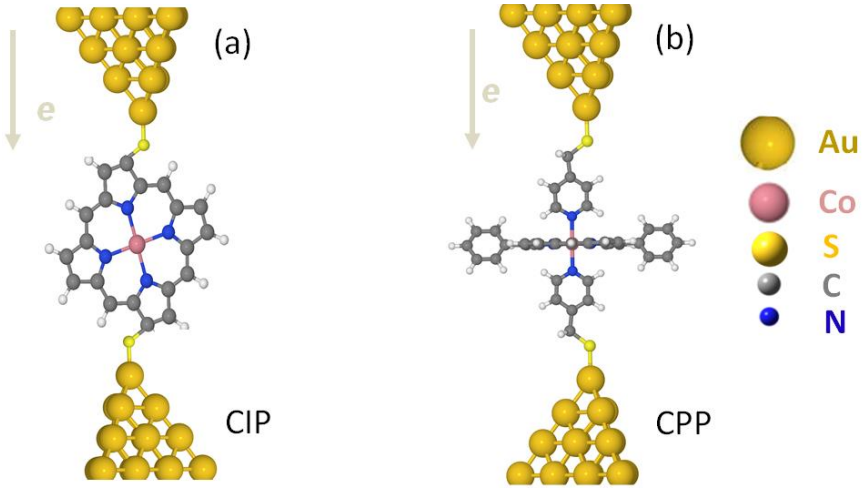

Figure 4. 1 *(a) Porphyrin skeleton aligned parallel to the direction of charge transport "current in plane" (CIP) in an up-right configuration and (b) the optimised sandwich configuration of DPP junction with the current perpendicular to the plane (CPP).*

Experimentally, the measurements were carried out by collaboration in Barcelona using a Scanning Tunneling Microscope (STM) and were performed on a system of 5,15-diphenylporphyrins with a centrally-coordinated divalent metal ion sandwiched edge-on

between gold leads, which in turn are functionalized by pyridine-4-yl-methanethiol (PY). The method used to determine the electrical conductance is described as a blinking experiment, where the blink in this study corresponds to molecular bridge formation between the pyridine-functionalized electrodes and the metallo-porphyrin molecule as shown in Figure (4.2). The spontaneous formation of junctions (blinking approach) could be envisioned as a method to momentarily freeze particular conformations in the single-molecule junction. Briefly, the STM-BJ experiments consist of repeatedly approaching and retracting the two pyridyl-functionalized electrodes, while monitoring the tunneling current flowing through the electrode-electrode STM junction under a low applied voltage bias, approximately 5000 current traces are collected and 10-15% of them are used to build a conductance histogram for each molecule, as shown in Figure 4.3 Here each of the histograms show three peaks which correspond to three different electrode separations. The high conductance peak was used to extract a most-probable value of the single-molecule conductance for the flat-stacked metallo-porphyrin[21]. The observed two low conductance peaks are commonly-observed for all porphyrins and they have been ascribed to molecular wires with more extended (tilted) conformations of the porphyrin bridging the gap at longer electrode-electrode separations[25]. The fact that the free-based DPP uniquely displays the low conductance features is evidence that such conformations arise from the interaction between the PY and the porphyrin ring moieties. The conductance values extracted from Gaussian fits to the conductance histograms for each metallo-porphyrin (Fig. 4.3) has been also supported by a static blinking STM approach, where the spontaneous formation of the porphyrin bridge is attained while holding a fixed electrode-electrode distance.

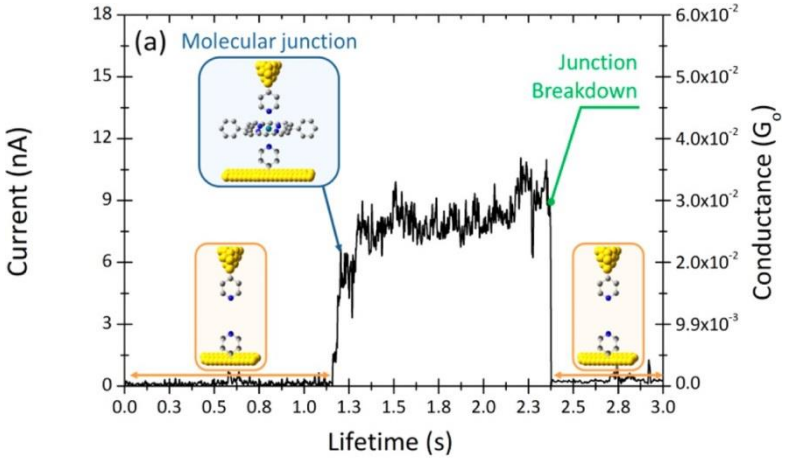

Figure 4.2 *Representative "blink" due to the spontaneous formation of a single-molecule junction with the Co-DPP molecule* [21].

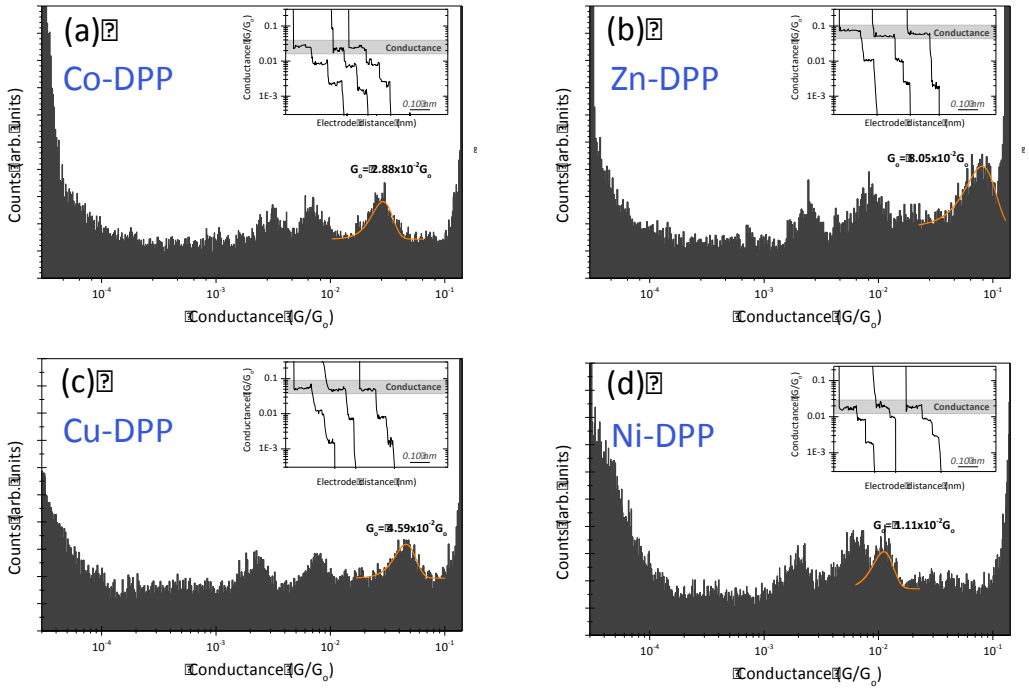

Figure 4.3 *(a, b, c and d) show the semi-log conductance histograms for the experimental STM single-molecule transport experiment for the Co-DPP, Zn-DPP, Cu-DPP and Ni-DPP systems, respectively. The inset shows representative single current decay curves used to build the conductance histograms. The applied BIAS was set to +25mV. The sharp increase in counts in both left and right sides of the histograms correspond to the current amplifier baseline and saturation respectively.*

4.2 Binding energies and relaxed configurations

The first stage in the theoretical modelling is to calculate the optimum geometry of the porphyrins between gold electrodes and to do this I minimize the binding energy. To calculate theoretical results for binding energies and relaxed configurations, spin-polarised DFT calculations were carried out using SIESTA[22] with the local density functional approximation parameterised by Ceperley and Adler[23]. Initially the geometry of each isolated porphyrin was optimised to a force tolerance less than 20 meV/Å using an extended double zeta polarised basis set of pseudo atomic orbitals for all atoms, and a mesh cutoff of 200Ry to define the real space grid. To model the electrode geometry, the optimized geometry of an isolated PY unit was obtained and then the geometry of a PY bound to a gold electrode via the thiol atom was computed. To explore the binding-energy landscape of the PY-functionalised gold tip above the plane of the M(II)-DPP, I performed, without further relaxation, a three dimensions scan of a PY-functionalised gold tip over 500 possible binding locations above the planes of the Co-DPP, Zn-DPP, Cu-DPP and Ni-DPP. For each location the binding energy E^B (see section 2.9) of the top PY with respect to the porphyrin was calculated using the counterpoise method[24, 25]. I find that the energetically-most-favorable configuration occurs when the PY nitrogen atoms are located above the metal atom of the porphyrin, as shown in Figure 4.4 for Co and figures Figure 4.5 for all the other metallo-porphyrins.

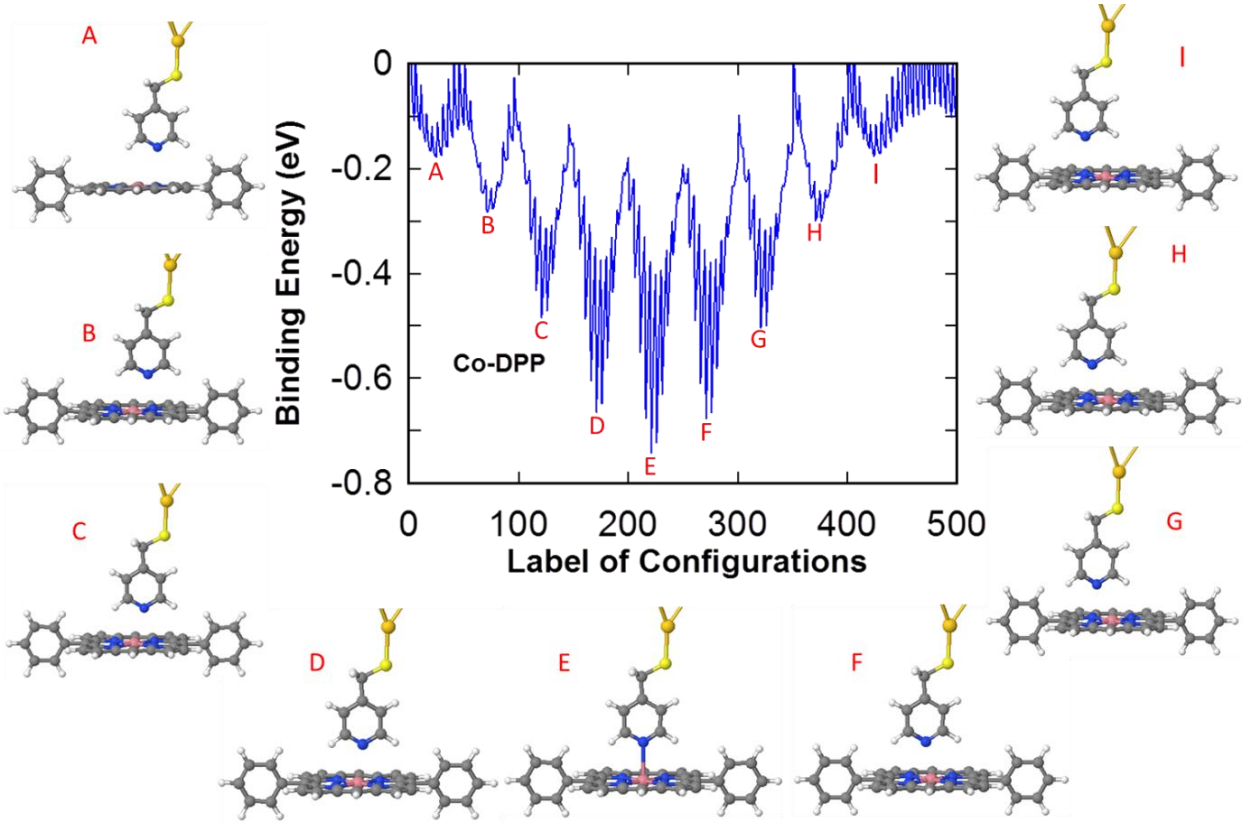

Figure 4.4 *The binding energies E^B for 500 positions of the PY-functionalized gold tip over the Co-DPP molecule surfaces. The closely-spaced oscillations are a result of varying the gold-PY-functionalised tip height above the surface, whereas the slow oscillations correspond to changes in the tip position parallel to the plane of the porphyrin.*

Next, I perform more detailed scans of the PYs along a vertical line through the metal atoms of the porphyrins without further relaxation and then at the final stage, allow further relaxation to determine more accurate values for their binding energies. Without further relaxation, the binding energy between each metallo-porphyrin and a single PY unit is computed as a function of the vertical distance of the nitrogen from the metal atom of the metallo-porphyrin, whilst holding the geometries of the PY and porphyrin fixed. To obtain

the lowest energy configurations, I performed further relaxation starting from the unrelaxed energy minima, the optimum distances and binding energies are shown in Figure 4.6.

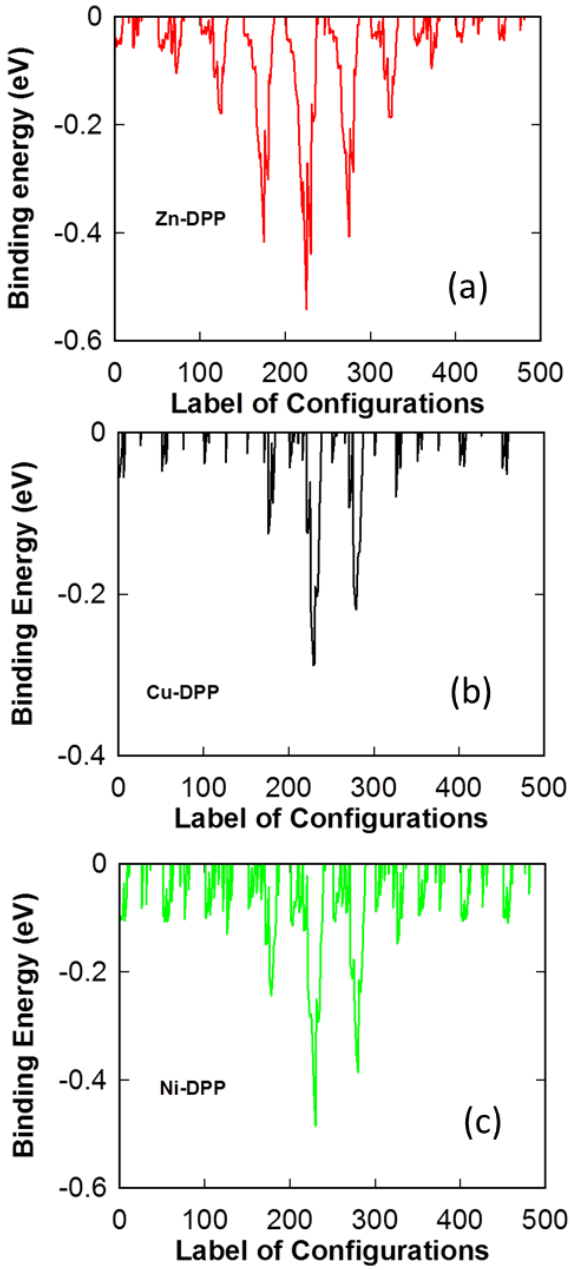

Figure 4.5 *The binding energies E^B for 500 positions of the PY-functionalized gold tip over the (a) Zn-DPP, (b) Cu-DPP and (c) Ni-DPP molecule surfaces.*

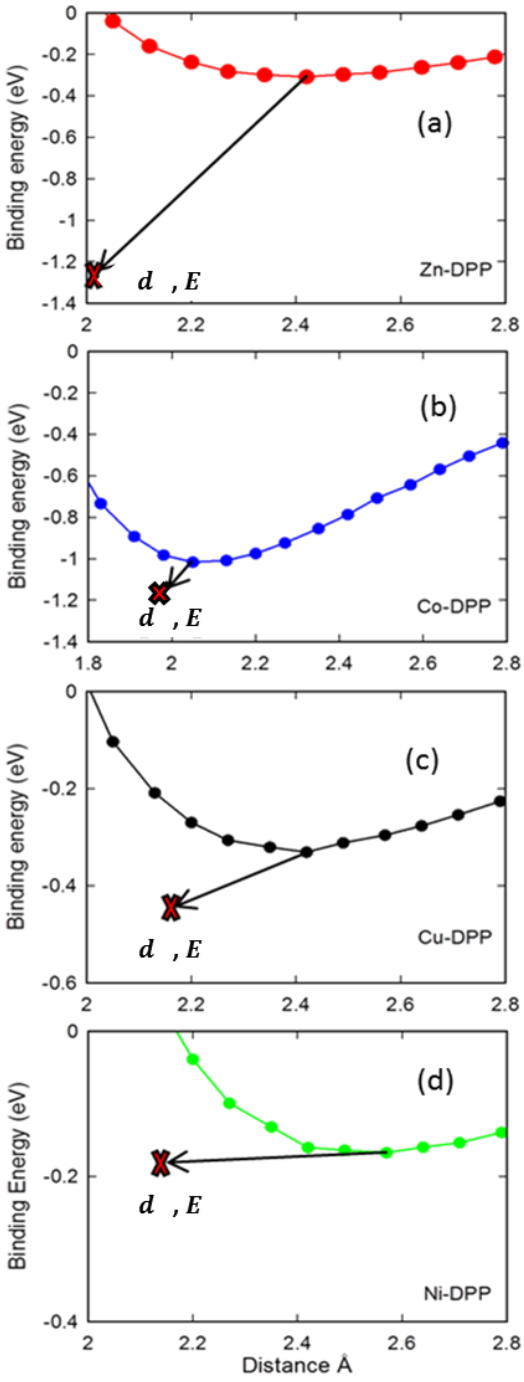

Figure 4. 6 *Figures (a, b, c and d) show DFT calculations of binding energies as a function of distance (d) for Zn, Co, Cu and Ni respectively. d, E are the position and binding energy of the fully-relaxed complex with a single PY.*

For all four metallo-porphyrins, I find that the energetically-most-favorable configuration occurs when the PY nitrogen atoms are located above the metal atom of the porphyrin. For this most-favorable position of the PY nitrogen atoms, the results for all four binding energies and the corresponding nitrogen-metal distances are shown in table 4.1.

Table 4.1: *Shows optimum distance*(d)*, and binding energies* E^B *for all four metallo-porphyrins.*

Metal	d Å	E^B eV
Zn	2.06	-1.21
Cu	2.17	-0.45
Co	1.97	-1.20
Ni	2.17	-0.17

4.3 Conductance calculations

To model an example of a blinking experiment in which the electrodes are held at a fixed separation, I choose the PY-functionalised gold electrodes to have a separation corresponding of 4.6 Å between the terminal nitrogen atoms of the PYs, as shown in figure 4.7. This distance is chosen to be slightly larger than the highest value of the distances d in table 4.1, such that all molecules can be accommodated within the electrode gap. I then allowed the porphyrin molecule to bind to the lower PY, with a N-to-metal-atom distance of

d (see table 4.1). The PY of the upper gold electrode is therefore more weakly bound to the metal atom of the porphyrin, as would be the case in a blinking experiment.

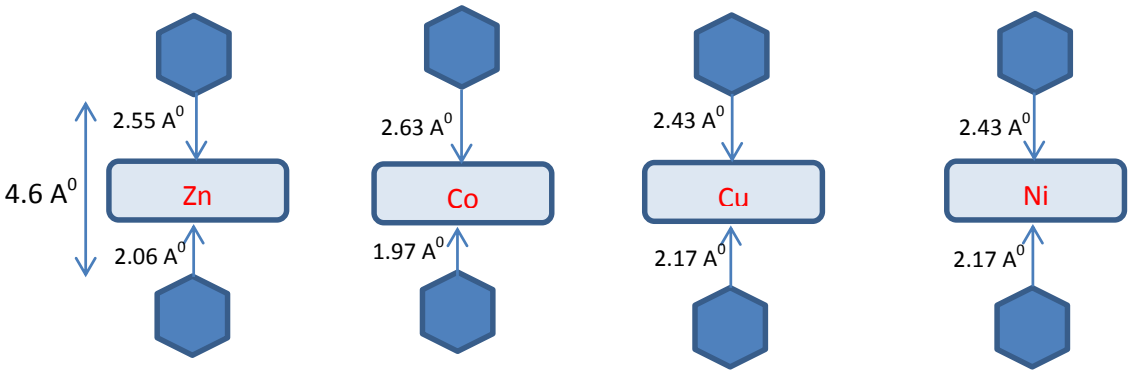

Figure 4.7 *Scheme of contact of pyridine anchor above the porphyrin molecule. The lower PY nitrogen is a distance d from the metal atoms, while the the upper PY nitrogen is placed a distance 4.6 Å above the lower PY nitrogen.*

Before computing transport properties, I first examined the spin state of the metallo-porphyrins. Numerous studies have examined the effect of the axial ligand on the redox [28, 29] and photovoltaic properties of metallo-porphyrins[30]. Nickel porphyrin with coordinating axial ligands are paramaganetic (S=1) in contrast to four-coordinate species (S=0) [31, 32]. Therefore, to accurately calculate the transport properties of these molecules, spin polarized transport calculations must be carried out. I find in the case of the zinc-metallo-porphyrin where there is no spin dependence the up spin and down spin transmission curves are almost identical. Figure 4.8a-d shows the spin-up, spin down and total transmission coefficient as a function of energy for Zn-DPP, Cu-DDP, Co-DPP and Ni-DDP.

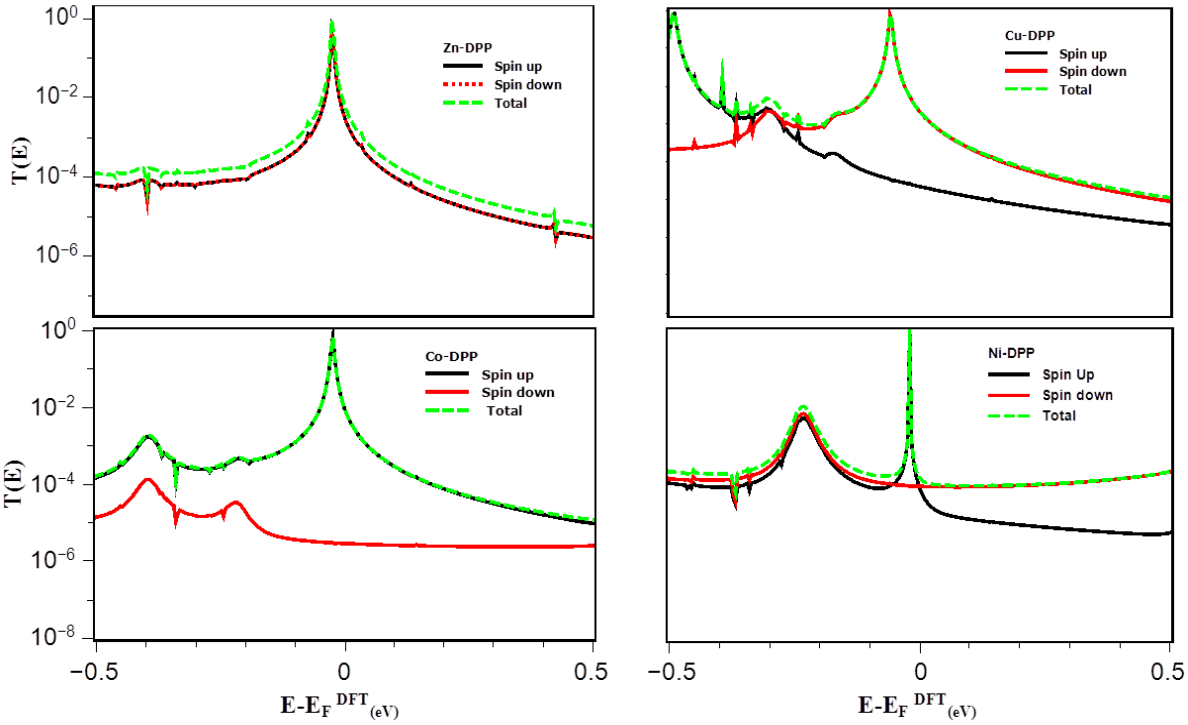

Figure 4.8 *The spin-up, spin down and total transmission coefficient as a function of energy for (a) Zn-DPP, (b) Cu-DDP, (c) Co-DPP and (d) Ni-DDP. Each PY-porphyrin is in its relaxed configuration, with the metal atom a distance d_1' from the N of the lower PY. The upper PY-functionalised gold electrode was then positioned such that distance between the upper and lower PY nitrogens was fixed at 4.6 Å.*

The conductance was then calculated using the Gollum quantum transport code[33], which utilizes the mean-field Hamiltonians provided by DFT. Starting from the SIESTA Hamiltonian, I use Gollum to calculate the transmission coefficient $T^{\sigma}(E)$, describing electrons of energy E, spin σ = [↑,↓] passing from one electrode to the other via the porphyrin, from which the finite-temperature electrical conductance G is obtained using the Landauer formula

$$G = G^{\uparrow} + G^{\downarrow} \qquad (4.1)$$

where $$G^{\sigma} = G_0 \int_{-\infty}^{\infty} dE\, T^{\sigma}(E) \left(-\frac{\partial f(E,T)}{\partial E}\right) \qquad (4.2)$$

In this expression, $f(E,T)$ is the Fermi distribution function defined as $f(E,T) = [e^{(E-E_F)/k_B\mathrm{T}} + 1]^{-1}$ where k_B is Boltzmann's constant and $G_0 = \left(\frac{2e^2}{h}\right)$ is the quantum of conductance.

Figure 4.8 shows the spin-up, spin down and the total transmission coefficients as a function of energy for Zn-DPP, Cu-DPP, Co-DPP and Ni-DPP respectively. The corresponding room-temperature conductances versus Fermi energy E_F are shown in Figure 4. 9a. Since the Fermi energy E_F^{DFT}predicted by DFT is not necessarily accurate[34], to compare theory with experiment, I treat the Fermi energy E_F as a single free parameter, chosen to determine four conductances, which are closest to the experimental trend. Figure 4. 9b shows that the experimentally-measured order Ni < Co < Cu < Zn is obtained by choosing a Fermi energy $E_F - E_F^{DFT} = -0.03eV$.

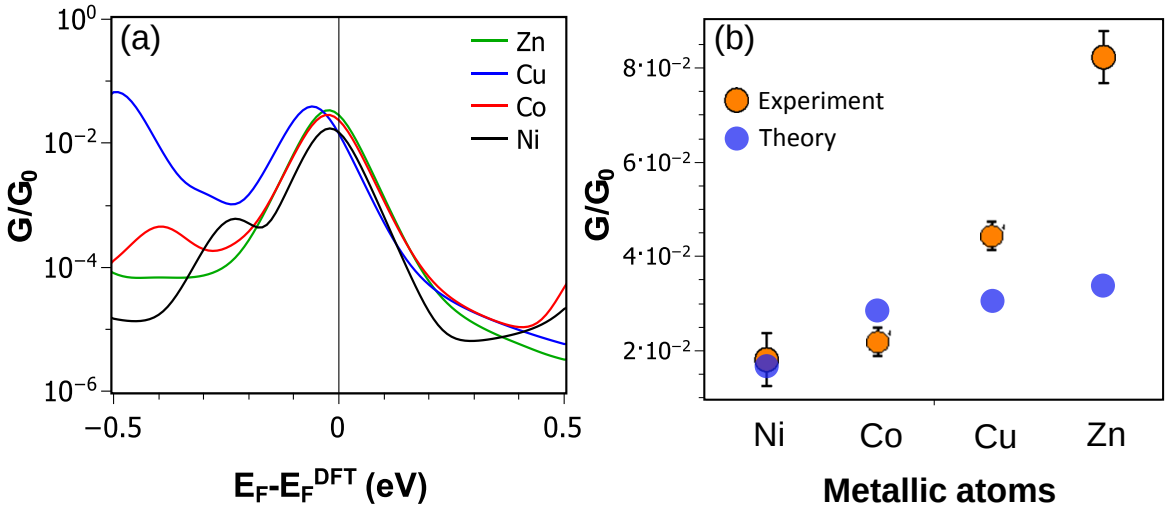

Figure 4.9 *The calculated room-temperature electrical conductances for Zn-DPP, Co-DPP, Cu-DPP and Ni-DPP, obtained from figure 4.9. (b) Comparison between experimental (orange circles) and theoretical conductances (blue circles) obtained by choosing an optimum values of* E_F - E_F^{DFT} = *-0.03 eV. The error bars in the experimental points (orange circles) represent the full width at half maximum from the corresponding conductance histogram peak in Fig. 4.3, which were obtained from the accumulation of hundreds of individual traces for every system.*

Figure 4.9b shows that the chosen junction separation captures the experimental ordering of the Ni-DPP, Co-DPP, Cu-DPP and Zn-DPP. Furthermore, the computed magnitudes of the conductances are of the same order as the measured values and these conductances are far higher than those measured for CIP junctions, which are typically less than 10^{-4} G_0.

4.4 Conclusions

I have investigated the electrical conductance with the current perpendicular to the plane (CPP) of supramolecular metall-oporphyrin wires. Both theory and experiment reveal that the variation in conductance across this family of molecules increases in the order Ni < Co < Cu < Zn. Experimentally the conductance of Zn-DPP is found to be a factor of 4 greater than that of Ni-DPP. Crucially the CPP conductances are three orders of magnitude greater than their CIP counterparts. For example as reported in [10] for Zn-porphyrins, the CIP conductance is $2.7 \cdot 10^{-5}\ G_0$, which is more than three orders of magnitude lower than our measured CPP conductance. Similarly in [2] the reported CIP conductances for Cu, Co and Ni porphyrins were $3.6\ 10^{-5}\ G_0$, $2.5\ 10^{-5}\ G_0$ and $1.9\ 10^{-5}\ G_0$ respectively. This supramolecularly-wired arrangement with the aromatic plane perpendicular to the current is therefore stable at room temperature and provides a unique family of high-conductance molecular wires, whose electrical conductances and binding energies can be tuned by metal substitution. From the point of view of stability, I find that the binding energies of Zn-DPP and Co-DPP are significantly higher than those of Ni-DPP and Cu-DPP and therefore in view of its higher conductance, I identify Zn-DPP as the favoured candidate for high-conductance CPP single-molecule devices.

Bibliography

1 Li, Z., Smeu, M., Ratner, M. A. & Borguet, E. Effect of anchoring groups on single molecule charge transport through porphyrins. The Journal of Physical Chemistry C 117, 14890-14898 (2013).

2 Liu, Z.-F. et al. Control of Single-Molecule Junction Conductance of Porphyrins via a Transition-Metal Center. Nano letters 14, 5365-5370 (2014).

3 Suslick, K. S., Rakow, N. A., Kosal, M. E. & Chou, J.-H. The materials chemistry of porphyrins and metalloporphyrins. Journal of Porphyrins and Phthalocyanines 4, 407-413 (2000).

4 Cárdenas-Jirón, G. I. Aza nitrogens effect on the electronic properties of cobalt porphyrine and derivatives. Journal of the Chilean Chemical Society 49, 101-104 (2004).

5 Auwärter, W., Écija, D., Klappenberger, F. & Barth, J. V. Porphyrins at interfaces. Nature chemistry 7, 105-120 (2015).

6 Dorough, G., Miller, J. & Huennekens, F. M. Spectra of the Metallo-derivatives of α, β, γ, δ-Tetraphenylporphine. Journal of the American Chemical Society 73, 4315-4320 (1951).

7 Gust, D. & Roberts, J. D. Nitrogen-15 nuclear magnetic resonance studies of porphyrins. Journal of the American Chemical Society 99, 3637-3640 (1977).

8 Vasilopoulou, M. et al. Large work function shift of organic semiconductors inducing enhanced interfacial electron transfer in organic optoelectronics enabled by porphyrin aggregated nanostructures. Nano Research 7, 679-693 (2014).

9 Cudia, C. C. et al. Electronic structure and molecular orientation of a Zn-tetra-phenyl porphyrin multilayer on Si (111). Surface science 600, 4013-4017 (2006).

10 Sedghi, G. et al. Long-range electron tunnelling in oligo-porphyrin molecular wires. Nature nanotechnology 6, 517-523 (2011).

11 Li, Y., Yao, J., Zhong, S. & Zou, Z. Theoretical investigations on the orientational dependence of electron transport through porphyrin molecular wire. Current Applied Physics 11, 1349-1353 (2011).

12 Ferradás, R., García-Suárez, V. M. & Ferrer, J. Symmetry-induced quantum interference effects in metalloporphyrin wires. Journal of Physics: Condensed Matter 25, 325501 (2013).

13 Beletskaya, I., Tyurin, V. S., Tsivadze, A. Y., Guilard, R. & Stern, C. Supramolecular chemistry of metalloporphyrins. Chemical reviews 109, 1659-1713 (2009).

14 McDermott, G. et al. Crystal structure of an integral membrane light-harvesting complex from photosynthetic bacteria. Nature 374, 517-521 (1995).

15 Zhang, Z. et al. Electron transfer by domain movement in cytochrome bc1. Nature 392, 677-684 (1998).

16 Regan, J. J., Ramirez, B. E., Winkler, J. R., Gray, H. B. & Malmström, B. G. Pathways for electron tunneling in cytochrome c oxidase. Journal of bioenergetics and biomembranes 30, 35-39 (1998).

17 Jurow, M., Schuckman, A. E., Batteas, J. D. & Drain, C. M. Porphyrins as molecular electronic components of functional devices. Coordination chemistry reviews 254, 2297-2310 (2010).

18 Gray, H. B. & Winkler, J. R. Electron flow through metalloproteins. Biochimica et Biophysica Acta (BBA)-Bioenergetics 1797, 1563-1572 (2010).

19 Allen, J. W., Watmough, N. J. & Ferguson, S. J. A switch in heme axial ligation prepares Paracoccus pantotrophus cytochrome cd1 for catalysis. Nature Structural & Molecular Biology 7, 885-888 (2000).

20 Simbeck, A. J., Qian, G., Nayak, S. K., Wang, G.-C. & Lewis, K. M. Gold–sulfur bond breaking in Zn (II) tetraphenylporphyrin molecular junctions. Surface science 606, 1412-1415 (2012).

21 Aragones, A. C. et al. Highly Conductive Single-Molecule Wires with Controlled Orientation by Coordination of Metalloporphyrins. Nano letters 14, 4751-4756 (2014).

22 Soler, J. M. et al. The SIESTA method for ab initio order-N materials simulation. Journal of Physics: Condensed Matter 14, 2745 (2002).

23 Ceperley, D. M. & Alder, B. Ground state of the electron gas by a stochastic method. Physical Review Letters 45, 566 (1980).

24 Jansen, H. & Ros, P. Non-empirical molecular orbital calculations on the protonation of carbon monoxide. Chemical Physics Letters 3, 140-143 (1969).

25 Boys, S. F. & Bernardi, F. d. The calculation of small molecular interactions by the differences of separate total energies. Some procedures with reduced errors. Molecular Physics 19, 553-566 (1970).

26 Song, X.-Z. et al. Representation of nonplanar structures of nickel (II) 5, 15-disubstituted porphyrins in terms of displacements along the lowest-frequency normal coordinates of the macrocycle. Journal of the American Chemical Society 118, 12975-12988 (1996).

27 Puigmartí-Luis, J., Saletra, W. J., González, A., Amabilino, D. B. & Pérez-García, L. Bottom-up assembly of a surface-anchored supramolecular rotor enabled using a mixed self-assembled monolayer and pre-complexed components. Chemical Communications 50, 82-84 (2014).

28 Lever, A. & Wilshire, J. Redox potentials of metal phthalocyanines in non-aqueous media. Canadian Journal of Chemistry 54, 2514-2516 (1976).

29 Takahashi, K., Komura, T. & Imanaga, H. Photoelectrochemical properties of thin films of zinc porphyrin derivatives with pyridyl group. Bulletin of the Chemical Society of Japan 62, 386-391 (1989).

30 Langford, C. H., Seto, S. & Hollebone, B. R. Effect of axially coordinated pi-acid ligands on photovoltaic properties of Zn-tetraphenylporphyrin. Inorganica chimica acta 90, 221-224 (1984).

31 Dommaschk, M. et al. Coordination-Induced Spin-State Switching with Nickel Chlorin and Nickel Isobacteriochlorin. Inorganic chemistry 54, 9390-9392 (2015).

32 Thies, S. et al. Coordination‐Induced Spin Crossover (CISCO) through Axial Bonding of Substituted Pyridines to Nickel‐Porphyrins: σ ‐Donor versus π ‐Acceptor Effects. Chemistry‐A European Journal 16, 10074-10083 (2010).

33 Ferrer, J. et al. GOLLUM: a next-generation simulation tool for electron, thermal and spin transport. New Journal of Physics 16, 093029 (2014).

34 Lambert, C. Basic concepts of quantum interference and electron transport in single-molecule electronics. Chemical Society Reviews 44, 875-888 (2015).

Chapter 5

High cross-plane thermoelectric performance of metallo-porphyrin molecular junctions

In this chapter, the thermoelectric properties of metallo-porphyrins in perpendicular junction has been examined theoretically. The thermoelectric properties to be tuned by the divalent metal substitution. By varying the transition metal-centre over the family Ni, Co, Cu, and Zn. The results presented in this chapter were published in Mohammed Noori, et al 'High cross-plane thermoelectric performance of metallo-porphyrin molecular junctions' Physical Chemistry Chemical Physics 2017.

5.1 Introduction

Thermoelectric materials utilize the Seebeck effect [1] to generate electricity from a temperature gradient, and the Peltier effect for on-chip cooling of electronic devices [2-5]. Nowadays, a great deal of effort is aimed to improve the efficiency of these effects and identifying the parameters that control the thermoelectric performance of materials and devices [6-12] . The efficiency of a thermoelectric device for power generation is characterized by the dimensionless figure of merit ($ZT = S^2GT/\kappa$) where S is the Seebeck coefficient, G is the electrical conductance, T is the temperature and κ the thermal conductance [12, 13]. Although most common thermoelectric materials are inorganic, there is growing interest in the development of organic thermoelectric materials [6-10, 18-22], partly because many widely-deployed inorganic thermoelectric materials are toxic, expensive to process and have limited global supplies. Since the thermoelectric performance of inorganic materials can be enhanced by taking advantage of nanostructuring [14-20], it is interest to utilize the natural nanostructuring associated with single-molecules attached to nanogap electrodes, or self-assembled monolayers of such molecule sandwiched between planar electrodes [21].

Porphyrins are attractive as building blocks for molecular-scale devices, because they are conjugated, rigid, chemically stable molecules and their properties could be modified by coordinating a variety of metallic ions (metallo-porphyrins) [22-30]. In what follows my aim is to explore the potential of metallo-porphyrin-based molecular junctions (fig. 5.1a) for high-efficiency thermoelectricity . From chapter four since the in-plane electrical conductance of porphyrins is rather low, I consider CPP “cross-plane” (current-perpendicular to the plane)

junctions in which the current flows perpendicular to the porphyrin plane[31]. A shown in figure 5.1, a porphyrin plane is contacted to gold electrodes via thiol or pyridyl anchor groups, with the plane of the porphyrin stacked perpendicular to the direction of charge transport. From the point of view of optimising thermoelectric properties, junctions formed from these molecules are of interest, because by varying the metal atom (denoted χ in figure 5.1) residing in the core of the organic porphyrin framework, I tune the molecular energy levels relative to the Fermi energy E_F of the electrodes. If energy levels happen to be close enough to E_F, then this should lead to transport resonances, which enhance the thermopower [32]. In what follows, I shall demonstrate that this is indeed the case and that large positive and negative thermopowers are achievable. Moreover, my calculations show that although the thermal conductance due to the phonons dominates the total thermal conductance, high values of ZT are achievable.

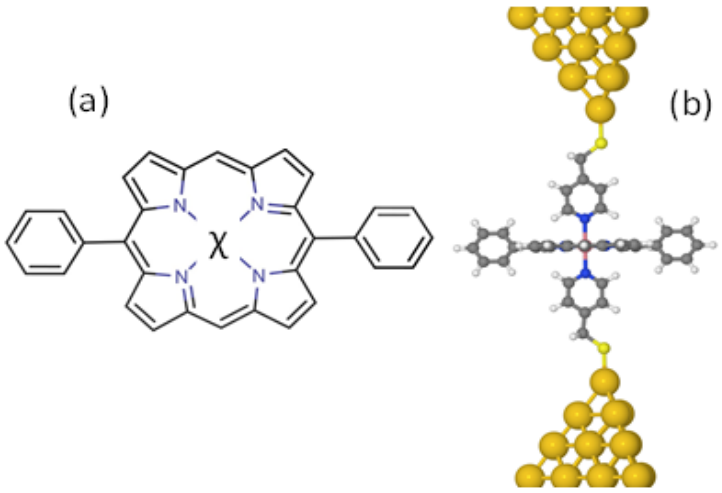

Figure 5.1 *Diphenylporphyrins -based molecular structures (a) with metallic atom, (b) an example of an optimized configuration of the system containing a single molecule χ -DPP sandwiched between two gold leads which in turn are activated by pyridine-4-yl- methanethiol with different metallic atoms, where χ = Co, Cu, Ni and Zn.*

The experiments and theory of chapter four show that the conductance of the metallo-porphyrins are enhanced when they are sandwiched between two gold electrodes with pyridine-4-yl- methanethiol anchors (fig. 5.1b) [31, 33]. Since large G is desirable, metallo-porphyrins studied in this work consist of four different metal atoms χ = Co, Cu, Ni and Zn coordinated in a flat-stacked 5,15-diphenylporphyrins-based molecular structures (Fig. 5.1a). Our aim in this work is to investigate the thermoelectric properties of these metallo-porphyrins devices by varying the metal atom χ over the series of χ = Co, Cu, Zn, and Ni.

5.2 Methods

To calculate the electronic and vibrational properties of each metallo-porphyrin, I used the spin density functional (DFT) code SIESTA[34] which employs Troullier-Martins pseudopotentials to represent the potentials of the atomic cores[35], and a local atomic-orbital basis set. I used a double-zeta polarized basis set for all atoms and the local density functional approximation (LDA-CA) by Ceperley and Adler [36]. The Hamiltonian and overlap matrices are calculated on a real-space grid defined by a plane-wave cutoff of 150 Ry. Each molecule was relaxed to the optimum geometry until the forces on the atoms are smaller than 0.02 eV/Å. To calculate the vibrational modes of each metallo-porphyrin I use the harmonic approximation method discussed in chapter three, to construct the dynamical matrix D After obtaining the relaxed geometry of each structure, as shown in Fig. 5.1. From these relaxed xyz coordinates, a set of the xyz coordinates were generated by displacing each atom in positive and negative x, y, and z directions by $\delta q' = 0.01$ Å. The forces in three directions q_i = (xi , yi , zi) on each atom were then calculated by DFT with the same parameters as the relaxed system but without geometry relaxation. These set of the force

$F_i^q = (F_i^x , F_i^y , F_i^z)$ vectors are used to construct the dynamical matrix(equation 3.6.1 see section 3.6). By using GOLLUM[37] the electronic and phononic transmission coefficients have been calculated.

5.3 Results and Discussion

For each metallo-porphyrin χ-DPP in figure 5.1b, figure 5.2a-d shows total electronic transmission coefficients as a function of energy for DPP with Co, Cu, Zn and Ni, respectively. The spin-dependent and total electronic transmission coefficients as a function of energy for all χ –DPP in Chapter 4 (Fig 4.8). Due to the thiol anchor all junctions show HOMO dominated transport where DFT Fermi energy is very close to the HOMO resonance. By using the Landauer formula equation (3.5.5), the electrical conductance could be calculated from the transmission coefficient shown in fig. 5.2. The electrical conductance is higher in Zn-DPP and lower in Ni-DPP (fig 4.9a Chapter 4) where $G_{Zn} > G_{Cu} > G_{Co} > G_{Ni}$ in agreement with the experimental values of Zn-DPP 8.2×10^{-2} , Cu-DPP 4.4×10^{-2} , Co-DPP 2.2×10^{-2} and Ni-DPP 1.8×10^{-2}. [33]

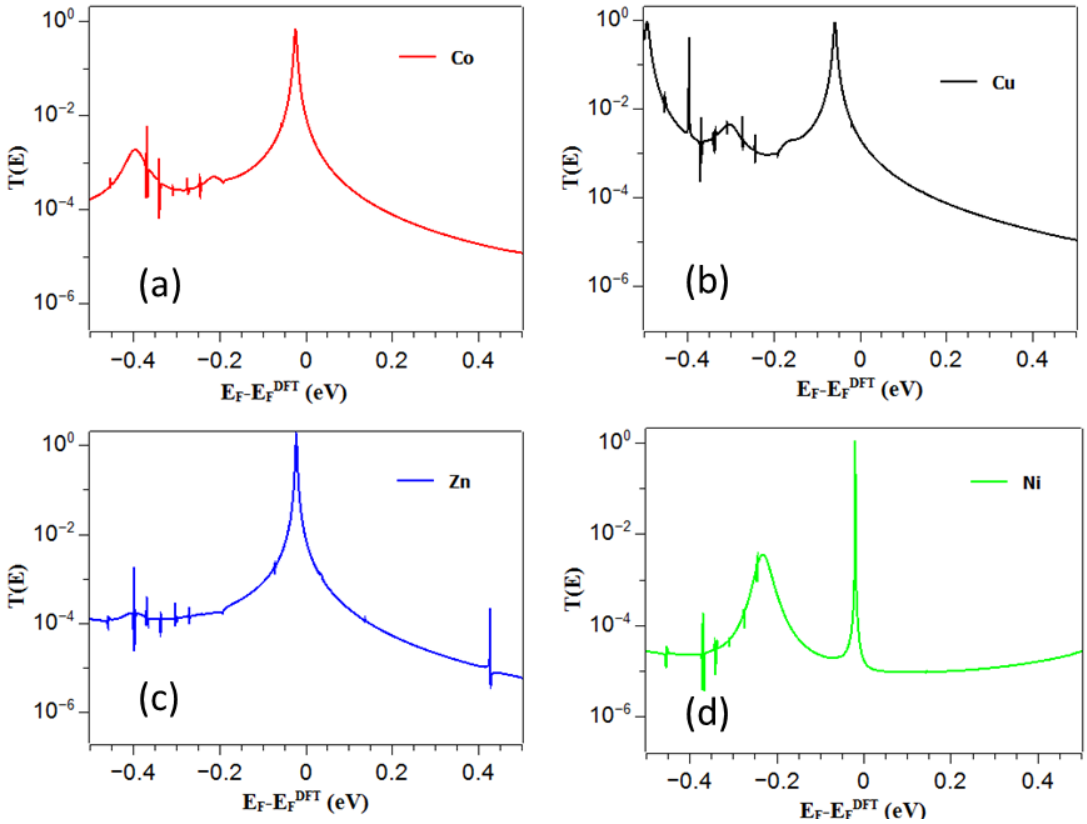

Figure 5.2 *(a, b, c, and d) show the electronic transmission coefficients as a function of energy for DPP with Co, Cu, Zn and Ni, respectively*

The wave function (φ) and the frequencies ω corresponding to the vibrational modes are the eigenvectors of the dynamical matrix D, which satisfies:

$$D\varphi = \omega^2\varphi \qquad (5.1)$$

The normal modes of vibration have amplitude $\varphi_{i\,\alpha}^{(\omega)}$ where $\alpha = 1,2,3$ labels x, y, z degrees of freedom and i=1,….N labels the atoms. This satisfies the normalization condition

$$\sum_{i=1}^{N}\sum_{\alpha=1}\left(\varphi_{i\,\alpha}^{(\omega)}\right)^2 = 1 \qquad (5.2)$$

To analyse the spatial distribution of a normal mode, it is useful to define a participation ratio PR, which describes the intensity of a normal mode on a sub-set $\{i', \alpha'\}$ of degrees of freedom from:

$$\mathrm{PR}^{(\omega)} = \sum_{\mathrm{i},\alpha\in\{\mathrm{i}',\alpha'\}} \left(\varphi_{\mathrm{i}\,\alpha}^{(\omega)}\right)^2 \tag{5.3}$$

If $\mathrm{PR}^{(\omega)} = 1$ then the normal mode of frequency ω resides entirely on the chosen sub-set of degrees of freedom.

$$PR^{tot} = \sqrt{PR_x^2 + PR_y^2 + PR_z^2} \tag{5.4}$$

Where PR_x, PR_y and PR_z represent intensity of a normal modes in x, y, z degrees of freedom respectively.

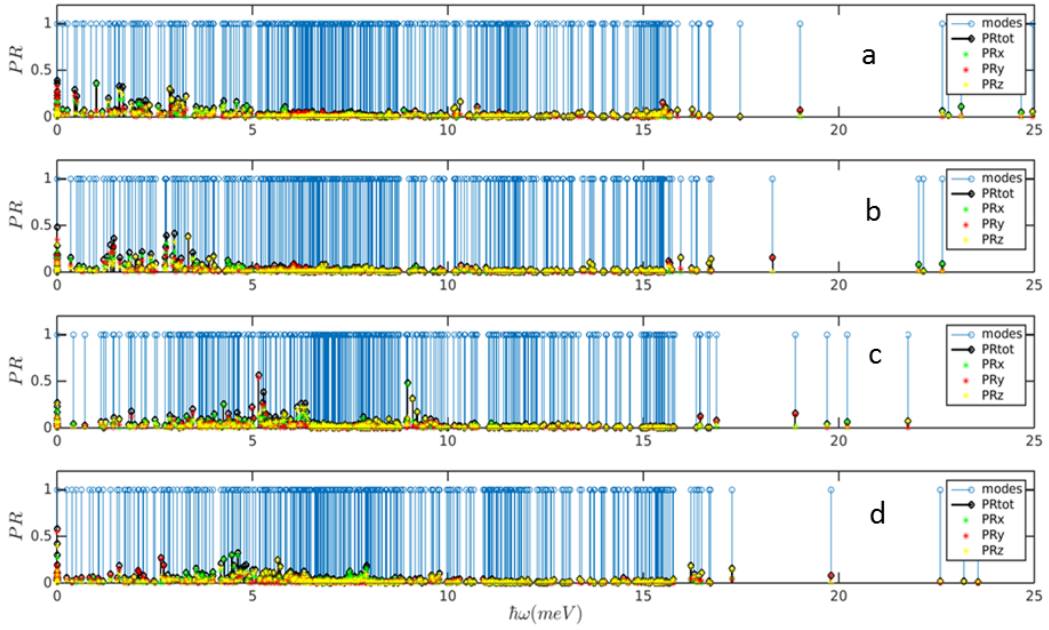

Figure 5.3. *Participation ratio of the molecular for (a) Cu-DPP, (b) Ni-DDP, (c) Co-DPP and (d) Zn-DDP.The number of modes between ħω =0 and 3meV is 35 for Co, 53 for Zn, 52 for Ni and 53 for Cu.*

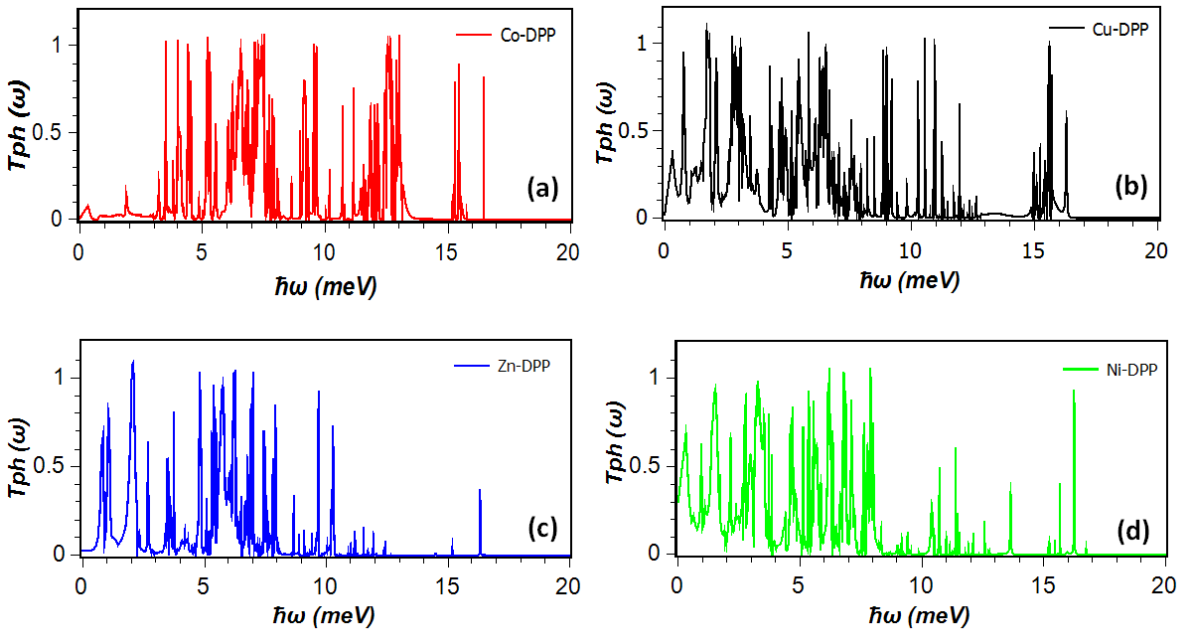

Figure 5.4 *(a, b, c, and d) show phonon transmission coefficient as a function of ħω for DPP with Co, Cu, Zn and Ni, respectively.*

Figure 5.3 Participation ratio of the molecular cores consisting of the χ -DPP on the modes associated with whole of the molecule attached to the surface of the gold electrodes. Figures 5.4 (a-d) shows phonon transmission coefficients as a function of phonon energy $\hbar\omega$ for DPP with Co, Cu, Zn and Ni, respectively. Figure 5.4a shows that the low energy phonons (smaller than 4 meV) are not transmitted. The binding energy in Co-DPP is higher than other metallo-porphryins studied in Chapter 4 table 4.1 [Ref.33].

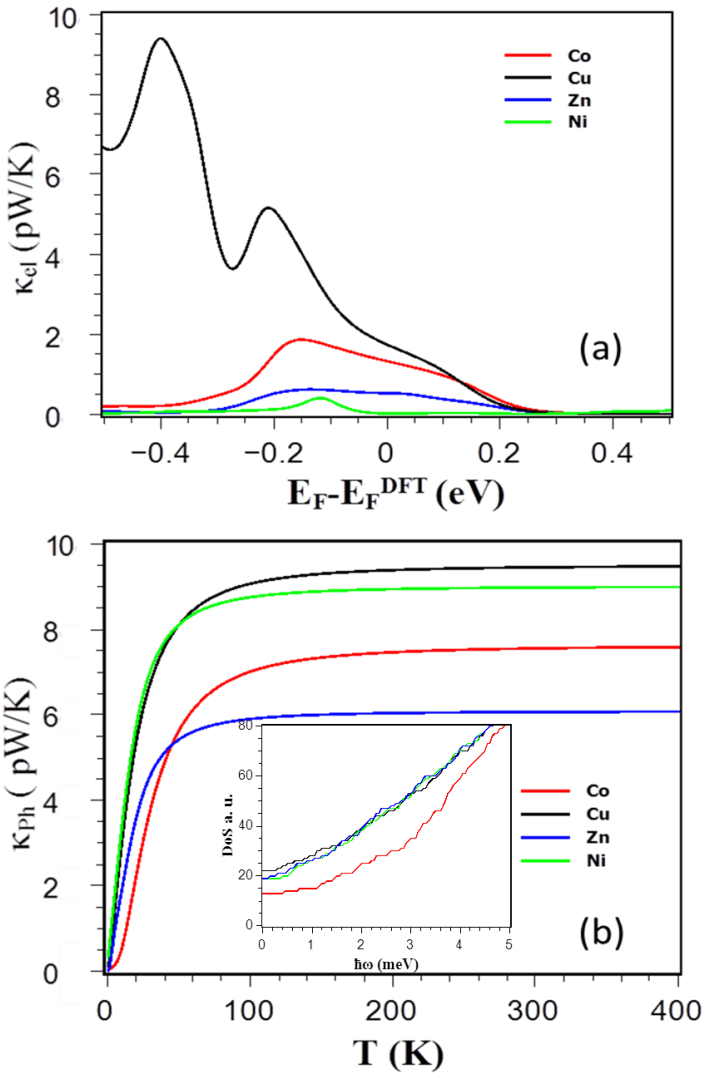

Figure 5.5 *(a) Show electronic contribution of the thermal conductance κel, inset figure shows the cumulative distribution of eigenvalues (integrated density of states) and (b) show phononic contribution of the thermal conductance κ_{ph} for DPP with Co, Cu, Zn and Ni.*

The thermal conductance of the junction ($\kappa = \kappa_{ph} + \kappa_{el}$) is obtained by summing the contributions from both electrons (κ_{el}) and phonons (κ_{ph}). The electronic (phononic) thermal conductances are calculated from the electronic (phononic) transmission coefficients (as described in (3.6) chapter three and Ref [32]). Comparison between figures 5.5a and 5.5b

shows that in the vicinity of DFT Fermi energy, the main source of the thermal conductance in these junctions is due to phonons, whose room-temperature contribution is relatively insensitive to the choice of metal atom, varying between 6 and 10 pW/K depending on the choice. The inset of figure 5.5b shows the cumulative distribution of eigenvalues (integrated density of states) of each molecule and reveals that the lower frequency modes of the Co porphyrin in the region 0 to 1.5meV are pushed to higher frequencies, leading to a low-frequency transmission gap below 3meV. This reflects the higher binding energy of a single pyridyl group to the Co metal atom compared with the other. (these follow the trend Co=-1.2eV, Zn=-1.2eV, Cu=-0.4eV and Ni=-0.17eV). Consequently the low-frequency cumulative distribution of Co and the low-temperature thermal conductance initially lies below that of the others and then rises with a steeper slope. Figure 5.4c shows that Zn also has a low-frequency transmission gap below 1meV, which supresses the low-temperature phonon thermal conductance.

Figure 5.6 shows Seebeck coefficient S (thermopower) and total figure of merit over a range of Fermi energies at room temperature for each metallo-porphyrins. Figure 5.6a demonstrates that both the magnitude and sign of thermopower S are sensitive to the metal atoms at the centre of the DPP, which determine the location of transport resonances relative to the Fermi energy. Since the Fermi energy from DFT is not necessarily reliable, I have presented the thermopower for a range of Fermi energies (fig. 5.6a).

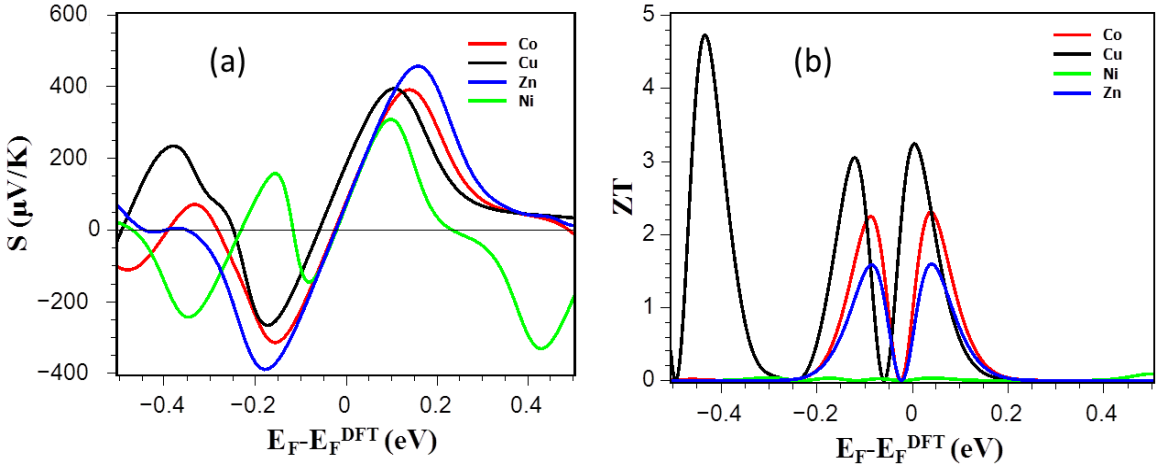

Figure 5.6 *Show (a) Seebeck coefficient S (thermopower) and (b) total figure of merit ZT over a range of Fermi energies at room temperature for each metallo-porphyrin.*

For the junctions discussed in this work, the conductances have been measured experimentally in chapter four, so I have estimated the Fermi energy by comparing these measurements with our calculated conductances. This yields a value of E_F = -0.03 eV, compared with the DFT-predicted Fermi energy. Table 5.1 shows the thermopower of porphyrins in the presence of Cu, and then Co, Zn and Ni at E_F = -0.03 eV. The predicted trend is $S_{Cu} > S_{Ni} > S_{Zn} > S_{Co}$ and when combined with the higher Cu CPP the yield room-temperature values of ZT range from 1.66 for Cu porphyrin to 0.01 for Ni porphyrin, as shown in figure 5.6b

Table 5.1. *Seebeck coefficient S (thermopower) and total figure of merit ZT at E_F - E_F^{DFT} = -0.03 eV[33]*

Metallic	**S (μV/K)**		**ZT**	
	E_F=-0.03 eV	**E_F=0.0 eV**	**E_F=-0.03 eV**	**E_F=0.0 eV**
Cu	+90	+182	1.66	3.22
Co	-16	+77	0.05	0.92
Zn	-23	+72	0.07	0.56
Ni	-32	+66	0.018	0.05

5.4 Conclusion

The room-temperature Seebeck coefficients of these junctions are rather high, ranging from 90 μV/K for Cu-porphyrin to -16 μV/K for Co-porphyrin. The corresponding room-temperature values of ZT range from 1.66 for Cu porphyrin to ~ 0.02 for Ni porphyrin. These values could be further increased by shifting molecular energy levels relative to the Fermi, either by doping or gating, which moves the Fermi energy closer to the regions of higher thermopower in figure 5.6. These results demonstrate that metallo- porphyrins are attractive building blocks for molecular-scale thermoelectricity and by passing thermal and charge currents perpendicular to the plane of the porphyrins, large values of the Seebeck coefficient and figure of merit are possible

Bibliography

1. Seebeck, T. J. *Annalen der Physik* **1826,** 82, (3), 253-286.
2. Chen, X.; Chen, L.; Guo, J.; Chen, J. *international journal of hydrogen energy* **2011,** 36, (10), 6099-6104.
3. Kumar, S.; Heister, S. D.; Xu, X.; Salvador, J. R.; Meisner, G. P. *Journal of electronic materials* **2013,** 42, (4), 665-674.
4. Ismail, B. I.; Ahmed, W. H. *Recent Patents on Electrical & Electronic Engineering (Formerly Recent Patents on Electrical Engineering)* **2009,** 2, (1), 27-39.
5. Voneshen, D.; Refson, K.; Borissenko, E.; Krisch, M.; Bosak, A.; Piovano, A.; Cemal, E.; Enderle, M.; Gutmann, M.; Hoesch, M. *Nature materials* **2013,** 12, (11), 1028-1032.
6. C. M. Finch, S. Sirichantaropass, S. W. Bailey, I. M. Grace, V. M. Garcia-Suarez, C. J. Lambert, *J. Phys. Condens. Matt*. 20, 022203 (2008)
7. Chaikin, P.; Kwak, J. *Review of Scientific Instruments* **1975,** 46, (2), 218-220.
8. Ke, S.-H.; Yang, W.; Curtarolo, S.; Baranger, H. U. *Nano letters* **2009,** 9, (3), 1011-1014.
9. Evangeli, C.; Gillemot, K.; Leary, E.; González, M. T.; Rubio-Bollinger, G.; Lambert, C. J.; Agrait, N. *Nano letters* **2013,** 13, (5), 2141-2145.
10. Balandin, A. A. *Nature materials* **2011,** 10, (8), 569-581.
11. Sadeghi, H.; Sangtarash, S.; Lambert, C. J. *Scientific reports* **2015,** 5, 9514.
12. Sadeghi, H.; Sangtarash, S.; Lambert, C. J. *Beilstein journal of nanotechnology* **2015,** 6, (1), 1176-1182.
13. Zimbovskaya, N. A. *Journal of Physics: Condensed Matter* **2014,** 26, (27), 275303.
14. Venkatasubramanian, R.; Siivola, E.; Colpitts, T.; O'quinn, B. *Nature* **2001,** 413, (6856), 597-602.
15. Harman, T.; Taylor, P.; Walsh, M.; LaForge, B. *Science* **2002,** 297, (5590), 2229-2232.

16. Poudel, B.; Hao, Q.; Ma, Y.; Lan, Y.; Minnich, A.; Yu, B.; Yan, X.; Wang, D.; Muto, A.; Vashaee, D. *Science* **2008,** 320, (5876), 634-638.
17. Liu, X.; Wang, D.; Shi, J. In *Thermoelectric transport in graphene with tunable mobility*, APS Meeting Abstracts, 2011; 2011; p 30013.
18. Yanagi, K.; Kanda, S.; Oshima, Y.; Kitamura, Y.; Kawai, H.; Yamamoto, T.; Takenobu, T.; Nakai, Y.; Maniwa, Y. *Nano letters* **2014,** 14, (11), 6437-6442.
19. Kambili, A.; Fagas, G.; Fal'ko, V. I.; Lambert, C. *Physical Review B* **1999,** 60, (23), 15593.
20. Fagas, G.; Kozorezov, A.; Lambert, C.; Wigmore, J.; Peacock, A.; Poelaert, A.; Den Hartog, R. *Physical Review B* **1999,** 60, (9), 6459.
21. Lambert, C. J.; Sadeghi, H.; Al-Galiby, Q. H. *Comptes Rendus Physique* **2016**.
22. Dorough, G.; Miller, J.; Huennekens, F. M. *Journal of the American Chemical Society* **1951,** 73, (9), 4315-4320.
23. Sedghi, G.; García-Suárez, V. M.; Esdaile, L. J.; Anderson, H. L.; Lambert, C. J.; Martín, S.; Bethell, D.; Higgins, S. J.; Elliott, M.; Bennett, N. *Nature nanotechnology* **2011,** 6, (8), 517-523.
24. Gust, D.; Roberts, J. D. *Journal of the American Chemical Society* **1977,** 99, (11), 3637-3640.
25. Li, Z.; Smeu, M.; Ratner, M. A.; Borguet, E. *The Journal of Physical Chemistry C* **2013,** 117, (29), 14890-14898.
26. Li, Z.; Borguet, E. *Journal of the American Chemical Society* **2011,** 134, (1), 63-66.
27. Liu, Z.-F.; Wei, S.; Yoon, H.; Adak, O.; Ponce, I.; Jiang, Y.; Jang, W.-D.; Campos, L. M.; Venkataraman, L.; Neaton, J. B. *Nano letters* **2014,** 14, (9), 5365-5370.
28. Li, Y.; Yao, J.; Zhong, S.; Zou, Z. *Current Applied Physics* **2011,** 11, (6), 1349-1353.
29. Ferradás, R.; García-Suárez, V. M.; Ferrer, J. *arXiv preprint arXiv:1208.3157* **2012**.
30. Beletskaya, I.; Tyurin, V. S.; Tsivadze, A. Y.; Guilard, R.; Stern, C. *Chemical reviews* **2009,** 109, (5), 1659-1713.
31. Aragonès, A. C.; Darwish, N.; Saletra, W. J.; Pérez-García, L.; Sanz, F.; Puigmartí-Luis, J.; Amabilino, D. B.; Díez-Pérez, I. *Nano letters* **2014,** 14, (8), 4751-4756.
32. Sadeghi, H.; Sangtarash, S.; Lambert, C. J. *Nano letters* **2015,** 15, (11), 7467-7472.

33. Noori, M.; Aragonès, A. C.; Di Palma, G.; Darwish, N.; Bailey, S. W.; Al-Galiby, Q.; Grace, I.; Amabilino, D. B.; González-Campo, A.; Díez-Pérez, I. *Scientific reports* **2016,** 6, 37352.

34. Soler, J. M.; Artacho, E.; Gale, J. D.; García, A.; Junquera, J.; Ordejón, P.; Sánchez-Portal, D. *Journal of Physics: Condensed Matter* **2002,** 14, (11), 2745.

35. Troullier, N.; Martins, J. L. *Physical Review B* **1991,** 43, (3), 1993.

36. Ceperley, D. M.; Alder, B. *Physical Review Letters* **1980,** 45, (7), 566.

37. Ferrer, J.; Lambert, C. J.; García-Suárez, V. M.; Manrique, D. Z.; Visontai, D.; Oroszlany, L.; Rodríguez-Ferradás, R.; Grace, I.; Bailey, S.; Gillemot, K. *New Journal of Physics* **2014,** 16, (9), 093029.

Chapter 6

High-performance thermoelectricity in edge-over-edge zinc-porphyrin molecular wires.

In this chapter, I have compared thermoelectric properties of three zinc porphyrin (ZnP) dimers and a ZnP monomer and find the "edge-over-edge" dimer formed from stacked ZnP rings possesses highest room-temperature ZT ever reported for an organic material.

The results presented in this chapter were published in Mohammed Noori, et al. "High-performance thermoelectricity in edge-over-edge zinc-porphyrin molecular wires", Nanoscale 9.16 (2017): 5299-5304.

.

6.1 Introduction

As mentioned in chapter five, thermoelectric materials, which convert heat to electrical energy, could have enormous impact on global energy consumption, but at present their efficiency is too low and the most efficient materials are toxic and have limited global supply. Recently, in an effort to overcome these limitations, thermoelectric effects in low-dimensional structures and molecular-scale systems have begun to be investigated[1-14]. Nanostructures are promising, because transport takes place through discrete energy levels and in molecular-scale junctions, this leads to room-temperature quantum interference, which opens further avenues for enhancing the conversion of heat into electric energy[15].

The efficiency of a thermoelectric (TE) material or device is determined by the dimensionless thermoelectric figure of merit $ZT = GS^2T/\kappa$, where G is the electrical conductance, T is temperature, S is the thermopower (Seebeck coefficient) and $\kappa = \kappa_{el} + \kappa_{ph}$ is thermal conductance due to electrons (κ_{el}) and phonons (κ_{ph}). The Seebeck coefficient characterizes the ability of a thermoelectric material to convert heat to electricity and is defined as $S=-\Delta V/\Delta T$, where ΔV is the voltage difference generated between the two ends of the junction when a temperature difference ΔT is established between them[7, 16-19]. Enhancing the efficiency of TE materials is not easy, because all parameters are correlated. For example at a fundamental level, the electronic properties G, S and κ_{el} are related, because as described in chapter three, they are all derived from the transmission coefficient $T_{el}(E)$ describing electrons of energy E passing from one electrode to the other through a molecule (see methods section 6.2). In

particular at low-temperatures the Seebeck coefficient S is approximately proportional to the slope of the $ln\ T_{el}(E)$, evaluated at the Fermi energy E_F, whereas the electrical conductance is proportional to $T_{el}(E_F)$. Therefore, if the Fermi energy lies in a region of high slope, close to a transmission resonance then both G and S are enhanced[20]. On the other hand, to decrease the thermal conductance κ, which appears in the denominator of ZT, both electron and phonon transport must be engineered. Therefore, simultaneous consideration of both electron and phonon transport is needed to develop new materials for thermoelectricity.

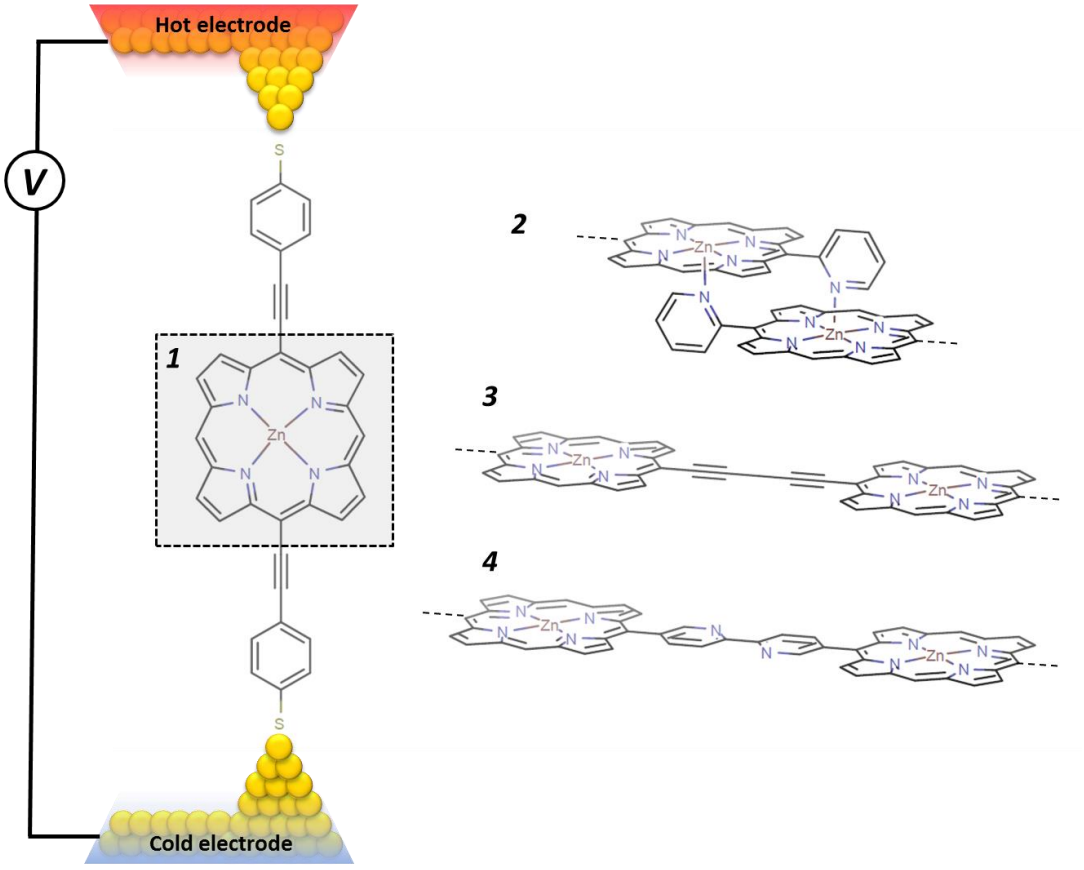

Figure 6.1 *The device structures investigated consist of four different zinc porphyrin (ZnP) monomer structures. (**1**) edge-over-edge ZnP, (**2**) A ZnP-dimer linked by an oligoyne chain, (**3**) A ZnP-dimer linked by two pyridyl rings (**4**).*

Since only a few groups worldwide are able to measure the thermal conductance of single molecules, theoretical investigation is needed to identify new strategies to simultaneously suppress phonons and enhance *S* and *G*. Recent proposals to reduce phonon transport in molecular junctions include weakening the overlap between the continuum of vibrational states in the electrodes and discrete vibrational modes of the molecules [21], taking advantage of the weak interaction between different parts of the molecules, as in π−π stacked structures [19] and using the low Debye frequency of electrodes to filter high-frequency phonons[20]. The challenge is to identify new materials and device structures in which such strategies can be realized in the laboratory. In this work, I present a comparative theoretical study of thermoelectric properties of four different zinc porphyrin structures and elucidate a new strategy for simultaneously increasing their thermopower and reducing their thermal conductance leading to a high value of *ZT*.

6.2 Methods

The geometry of each structure consisting of the gold electrodes and a single zinc porphyrin molecule was relaxed to a force tolerance of 20 meV/Å using the SIESTA [28] implementation of density functional theory (DFT), with a double-ζ polarized basis set (DZP) and generalized gradient functional approximation (GGA-PBE) for the exchange and correlation functionals [30, 31], which is applicable to arbitrary geometries. A real-space grid was defined with an equivalent energy cutoff of 150 Ry. From the relaxed *xyz* coordinate of the system, sets of *xyz* coordinates were generated by displacing each atom in positive and negative *x*, *y*,

and *z* directions by $\delta q'$ = 0.01 Å. The forces in three directions $q_i = (x_i , y_i , z_i)$ on each atom were then calculated by DFT without geometry relaxation. These values of the force is combined with the method described in [20] to calculate dynamical matrix and thermal conductance due to the phonons.

To calculate electronic properties of the molecules in the junction, from the converged DFT calculation, the underlying mean-field Hamiltonian *H* was combined with our quantum transport code, GOLLUM [29] to calculate the transmission coefficient $T_{el}(E)$ for electrons of energy E passing from the source to the drain. As discussed in chapter three, the electrical conductance $G_{el}(T) = G_0 L_0$, the electronic contribution of the thermal conductance $\kappa_{el}(T) = (L_0 L_2 - L_1^2)/hTL_0$ = and the thermopower $S(T) = -L_1/eTL_0$ of the junction are calculated from the electron transmission coefficient $T_{el}(E)$ where$L_n(T) = \int_{-\infty}^{\infty} dE(E - E_F)^n T_{el}(E)\left(-\frac{\partial f_{FD}(E,T)}{\partial E}\right)$ and $f_{FD}(E,T)$ is the Fermi−Dirac probability distribution function $f_{FD}(E,T) = (e^{(E-E_F)/K_B T} + 1)^{-1}$, *T* is the temperature, E_F is the Fermi energy, $G_0 = 2e^2/h$ is the conductance quantum, e is electron charge, and *h* is the Planck's constant.

6.3 Results and discussion

Figure 6.1 shows four different zinc porphyrin (ZnP) structures investigated below. The first **1** is a ZnP monomer[22]. Structure **2** is an edge-over-edge ZnP dimer, in which two ZnPs are locked together by *meso*-position pyridines[23, 24]. Structure **3** comprises two ZnPs connected by an oligoyne linker[22, 25, 26], while **4** comprises two ZnPs connected through *meso*-position pyridines[27]. In this work, my aim is to demonstrate that of the above structures, the edge-

over-edge ZnP dimer **2** is by far the most efficient thermoelectric energy converter. From a structural point of view, this arises because the pyridyl rings of **2** are locked and therefore ring rotation, which would otherwise reduce the electrical conductance, is eliminated. Secondly, the edge-over-edge rigid conformation of **2** increases its rigidity, which pushes the internal vibrational modes to higher frequencies. This reduces room temperature thermal conductance, because modes with frequencies greater than ~25meV do not contribute significantly. Thirdly, longitudinal modes entering one end of the edge-over-edge molecule must convert to flexural modes to pass from one porphyrin to the other, which creates extra phonon scattering and reduces thermal conductance.

For the structures of figure 6.1, figure 6.3 shows the transmission coefficients for electrons with energy E and phonons of energy $\hbar\omega$, passing through a molecule from the left electrode to the right electrode, calculated using the method described in reference[20]. I first carry out geometry optimization of each molecule placed between two gold electrodes using the SIESTA[28] implementation of density functional theory (DFT) to find the ground state optimized positions of the atoms relative to each other (see methods). From the ground state geometry, I obtain the mean-field Hamiltonian of each system comprising both electrodes and molecule and use our transport code GOLLUM[29] to calculate the transmission coefficients $T_{el}(E)$ (see methods). In each case the optimal angle between the porphyrins is zero, which corresponds to the maximum conductance that could be obtained[22]. The electronic transport properties of **1** and **3** have been studied experimentally in the literature[22], so I used these to benchmark our calculations. As shown in table 6.1, our calculated conductances for these molecules are in good agreement with experiment. The

electron transmission of **4** is much smaller than both **1**, **2** and **3**, whereas the transmission of **2** is either equal to that of **3** near the HOMO resonance or lower in the vicinity of the middle of the HOMO-LUMO gap. As shown in figure (6.2), this is reflected in the electrical conductance as a function of temperature.

Table.6.1 *The experimental and theoretical electrical conductance and their ratio for dimer and monomer.*

Structure	**Experimental Conductance**	**Theory Conductance**
Monomer (**1**)	$2.7x10^{-5}$	$1.09x10^{-1}$
Dimer (**3**)	$1.55x10^{-5}$	$6.35x10^{-2}$
Ratio (monomer/dimer)	1.74	1.72

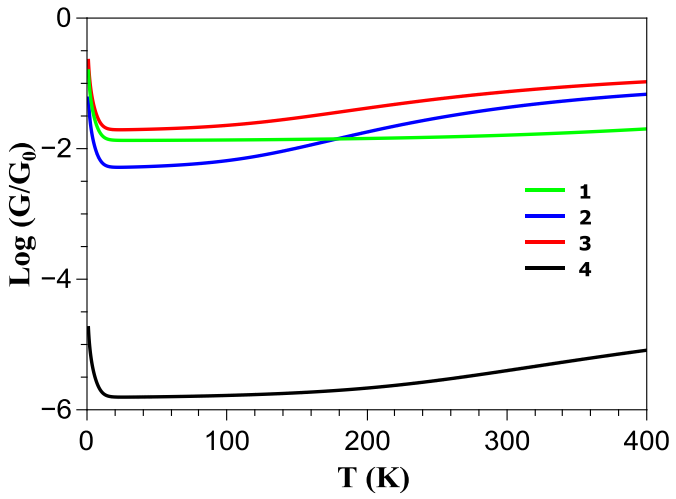

Figure 6.2 *The electrical conductance as a function of temperature for ZnP monomer (1), edge-over-edge ZnP (2), ZnP connected through an oligoyne chain (3) and ZnP-dimer connected through pyridyl rings (4).*

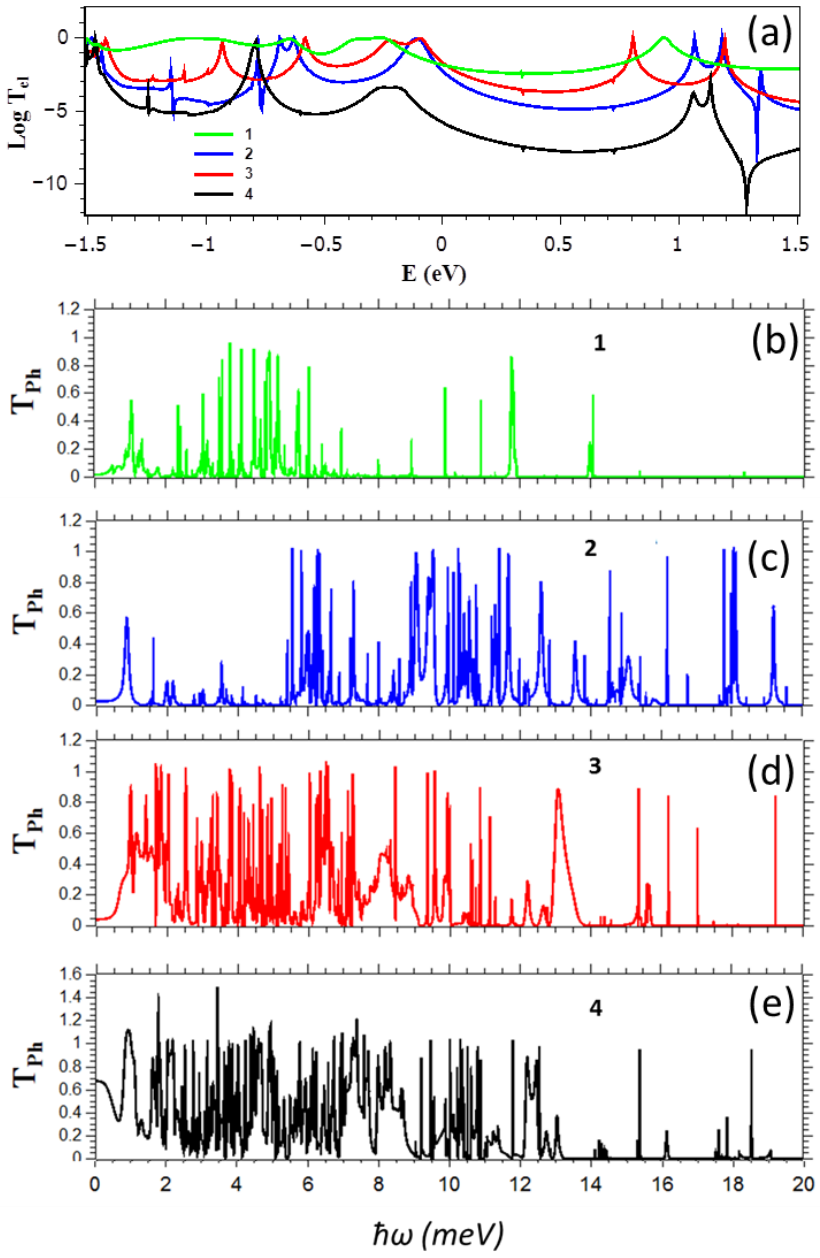

Figure 6.3 *(a) Electron transmission coefficients as a function of energy and (b-e) phonon transmission coefficients as a function of ħω (b) for the ZnP monomer **1**, (c) the edge-over-edge ZnP **2**, (d) the ZnP dimer connected via an oligoyne chain **3** and (e) ZnP dimer connected through pyridyl rings **4**.*

To calculate the vibrational properties of each structure, I again use the harmonic approximation to construct the dynamical matrix *D*. Each atom is displaced from its ground-state equilibrium position by $\delta q'$ and $-\delta q'$ in *x*, *y*, and *z* directions and the forces on all atoms calculated in each case. For 3n degrees of freedom (*n* = number of atoms), the $3n \times 3n$ dynamical matrix $D_{ij} = (F_i^q(\delta q_j') - F_j^q(-\delta q_j'))/2M_{ij}\delta q_j'$ is constructed, where *F* and *M* are the force and mass matrices, As described before in section 5.3 in chapter five the participation ratio *PR* of the molecule core (ZnPs and linkers) connected to the gold surface has also been calculated.

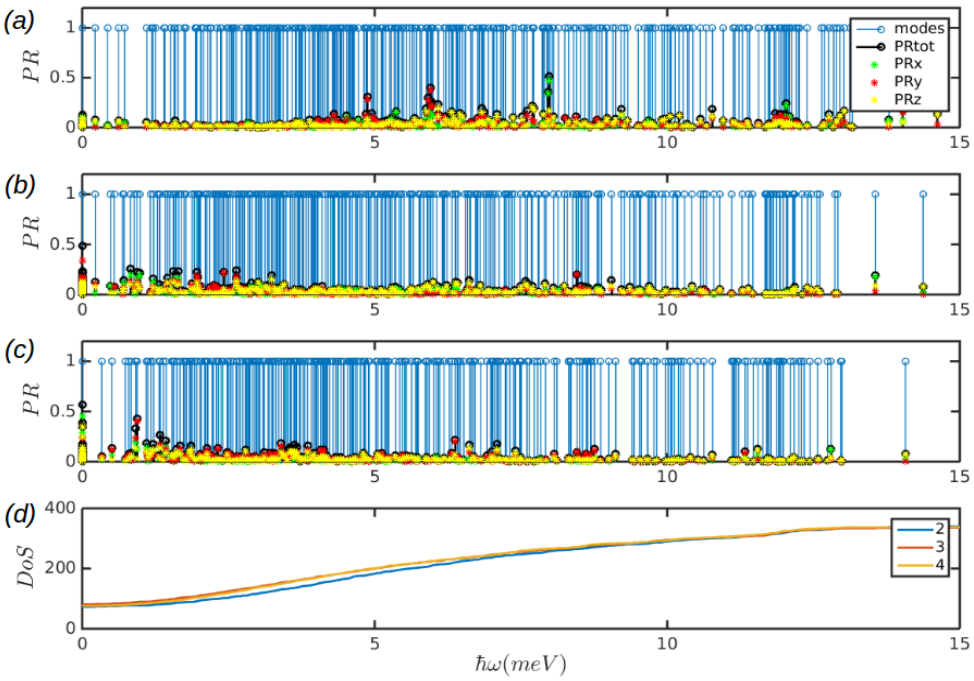

Figure 6.4. *Participation ratio of the molecular cores consisting of the ZnP(s) and linkers on the modes associated with whole of the molecule attached to the surface of the gold electrodes, (a) for the edge-over-edge structure (2), the modes have pushed to the higher energies and only in plane transverse modes are transmitted. Out-of plane transverse mode are suppressed due to the more rigid nature of (2) compared to (b) structure (3) and (c) structure (4) in out-of-plane transverse direction. (d) Shows the density of modes for (1-3).*

For a molecule within a junction, the dynamical matrix describes an open system composed of the molecule and two semi-infinite electrodes and is used to calculate transmission coefficient $T_{ph}(\omega)$ for phonons with energy $\hbar\omega$ passing through the molecule from the right to the left electrodes[20].

Figures 6.3 b-e shows $T_{ph}(\omega)$ for the four structures of figure 6.1. It is apparent that the widths of the resonances in the edge-over-edge ZnP-dimer **2** are slightly smaller than those of the other structures and the low energy phonons (in the range 2-5 *meV*) are either suppressed or pushed to the higher frequencies. This can be demonstrated using the participation ratio of the dimer molecular cores **2**, **3** and **4** and comparing the integrated density of states $Dos(\hbar\omega)$ of **2**, **3** and **4**. As shown in figure (6.4), the participation ratio of the molecule core (ZnPs and linkers) connected to the gold surface is mostly due to the in-plane (PRy) and out of plane (PRx) transverse modes in structures **3** and **4**, whereas out-of plane transverse modes are mainly suppressed or converted to in-plane transverse modes and moved to the higher frequency, reflecting the higher rigidity of the edge-over-edge structure. In addition, the integrated density of states are almost the same for **3** and **4**, whereas for low frequencies, the integrated density of states of **2** is smaller than **3** and **4**. This means the thermal conductance is reduced significantly in **2**, because transmission of the low energy modes is suppressed due to the scattering from in-plane modes to cross-plane transverse modes. In addition, some modes are pushed to higher frequency, although this is smaller effect compared with the suppression of low frequency transmission. Overall, these two effects combine to yield a lower phonon thermal conductance in **2**.

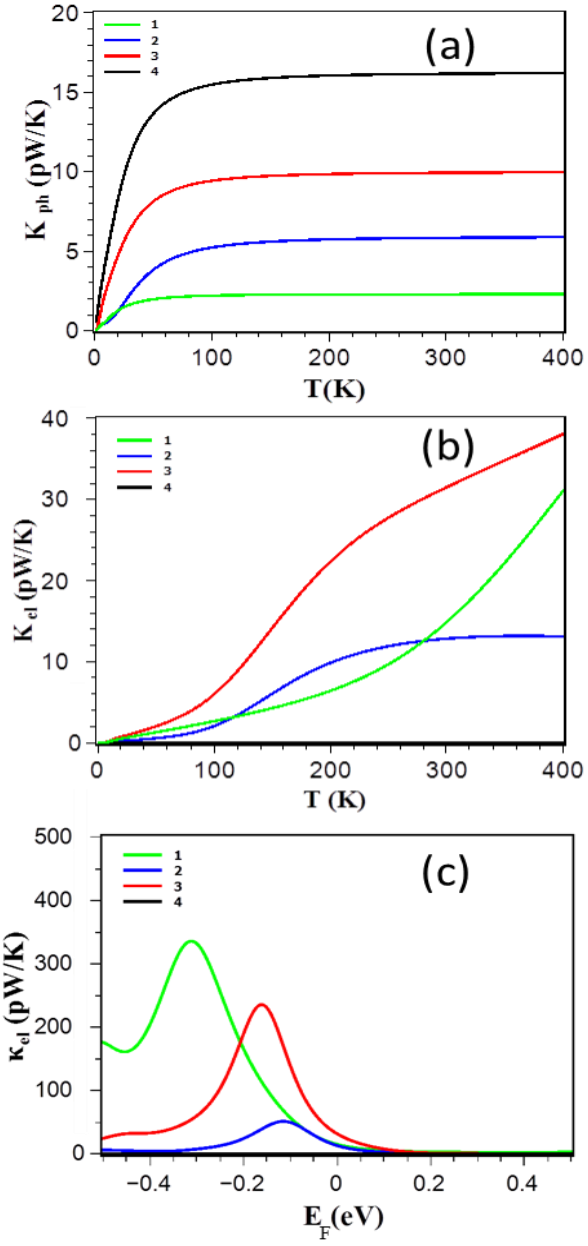

Figure 6.5 *(a) Phonon thermal conductances (b) Electronic thermal conductance as a function of temperature, (c) Room-temperature electronic thermal conductance as a function of Fermi energy EF calculated using the DFT-predicted Fermi energy. Results are shown for the ZnP monomer 1, the edge-over-edge ZnP 2, the ZnP dimer connected through an oligoyne chain 3 and the ZnP-dimer connected through pyridyl rings 4.*

The thermal conductance of the junction ($\kappa = \kappa_{ph} + \kappa_{el}$) is obtained by summing the contributions from both electrons (κ_{el}) and phonons (κ_{ph}). The electronic (phonon) thermal conductances are calculated from the electron (phonon) transmission coefficients shown in figure 6.3a-e. Figure 6.5a shows that the ZnP monomer **1** has the lowest value of κ_{ph} while **4** has the highest. This is counter-intuitive, because one would expect a higher thermal conductance for shorter molecules. However, due to the more rigid nature of the monomer, its vibrational modes are pushed to the higher frequencies and therefore their contribution to the room temperature conductance is suppressed. In addition, figure 6.5 b,c shows that the thermal conductance due to the electrons κ_{el} of the dimer ZnP **3** is higher than those of the edge-over-edge ZnP and structures **1** and **4** for a wide range of energy in the vicinity of DFT predicted Fermi energy. The crucial point is that almost for all Fermi energies, the electronic contribution to the thermal conductance is higher than the phonon contribution. This is significant, because to achieve a high-ZT material, one needs to only focus on engineering the electronic properties of structure **2**.

To examine the thermoelectric properties of **1**-**4**, I obtained the Seebeck coefficient of all structures from the electron transmission coefficient $T_{el}(E)$, as described in the methods. Figure 6.6 a shows the Seebeck coefficients as a function of Fermi energy E_F and reveals that the edge-over-edge ZnP dimer **2** has a higher Seebeck coefficient than **1**, **3** and **4** due to the higher slope of $ln\ T_{el}(E_F)$ over a wide range of Fermi energies between the HOMO and LUMO. Since the electronic contribution to the thermal conductance is higher in **1**, **2** and **3**, the contribution of the phonons is negligible. Furthermore the electrical conductance is proportional to the electronic thermal conductance, so they cancel each other in *ZT*.

Consequently as shown in figure 6.6b, due to the high Seebeck coefficient of the edge-over-edge dimer, a *ZT* as high as ≈4 is obtained when E_F lies in a wide energy window in the vicinity of the DFT-predicted Fermi energy. Figure 6.6b also shows that the less-rigid structure **4** is not promising for efficient conversion of the heat to electricity. Although all of these structures are made from ZnP, this study shows the importance of the molecular design. The more rigid edge-over-edge ZnP dimer 2 shows very high ZT, whereas the less conductive structure 3 is unattractive for thermoelectricity.

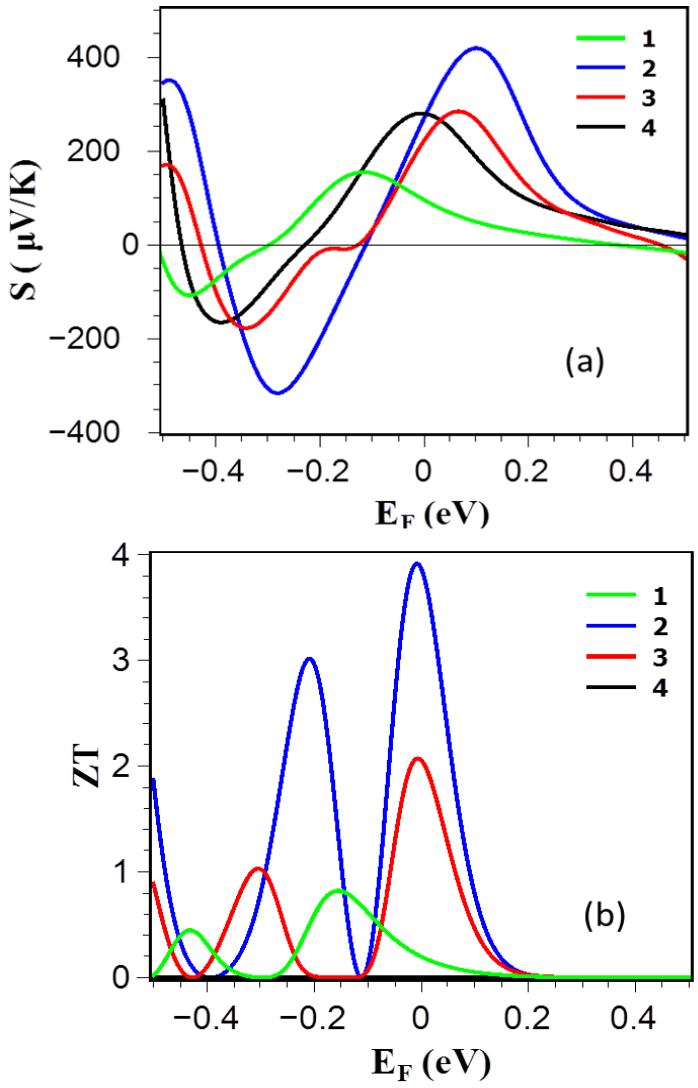

Figure 6.6 *(a) Seebeck coefficient S and (b) full thermoelectric figure of merit ZT as a function of Fermi energy for the ZnP monomer **1**, edge-over-edge ZnP **2**, ZnP connected through an oligoyne chain **3** and ZnP-dimer connected through pyridyl rings **4**.*

6.4 Conclusions

In summary, I have compared thermoelectric properties of three ZnP dimers and a ZnP monomer and find the edge-over-edge -like dimer possesses a negligible phonon thermal conductance and a high Seebeck coefficient of order 300 μV/K. These transport properties combine to yield a room-temperature figure of merit of $ZT \approx 4$, which is the highest room-temperature *ZT* ever reported for an organic material. This high *ZT* value is a consequence of low phonon thermal conductance, which arises from the edge-over-edge stacking of the porphyrin rings, which hinders phonon transport through the molecule.

Bibliography

1. Sadeghi, H.; Sangtarash, S.; Lambert, C. J. *Scientific reports* **2015,** 5.
2. Christensen, M.; Abrahamsen, A. B.; Christensen, N. B.; Juranyi, F.; Andersen, N. H.; Lefmann, K.; Andreasson, J.; Bahl, C. R.; Iversen, B. B. *Nature Materials* **2008,** 7, (10), 811-815.
3. Joshi, G.; Lee, H.; Lan, Y.; Wang, X.; Zhu, G.; Wang, D.; Gould, R. W.; Cuff, D. C.; Tang, M. Y.; Dresselhaus, M. S. *Nano letters* **2008,** 8, (12), 4670-4674.
4. Kim, W.; Singer, S. L.; Majumdar, A.; Vashaee, D.; Bian, Z.; Shakouri, A.; Zeng, G.; Bowers, J. E.; Zide, J. M.; Gossard, A. C. *Applied Physics Letters* **2006,** 88, (24), 242107.
5. Venkatasubramanian, R.; Siivola, E.; Colpitts, T.; O'quinn, B. *Nature* **2001,** 413, (6856), 597-602.
6. Hicks, L.; Harman, T.; Sun, X.; Dresselhaus, M. *Physical review B* **1996,** 53, (16), R10493.
7. Reddy, P.; Jang, S.-Y.; Segalman, R. A.; Majumdar, A. *Science* **2007,** 315, (5818), 1568-1571.
8. Hochbaum, A. I.; Chen, R.; Delgado, R. D.; Liang, W.; Garnett, E. C.; Najarian, M.; Majumdar, A.; Yang, P. *Nature* **2008,** 451, (7175), 163-167.
9. Baheti, K.; Malen, J. A.; Doak, P.; Reddy, P.; Jang, S.-Y.; Tilley, T. D.; Majumdar, A.; Segalman, R. A. *Nano letters* **2008,** 8, (2), 715-719.
10. Boukai, A. I.; Bunimovich, Y.; Tahir-Kheli, J.; Yu, J.-K.; Goddard Iii, W. A.; Heath, J. R. *Nature* **2008,** 451, (7175), 168-171.
11. Schwab, K.; Henriksen, E.; Worlock, J.; Roukes, M. L. *Nature* **2000,** 404, (6781), 974-977.
12. Uchida, K.; Takahashi, S.; Harii, K.; Ieda, J.; Koshibae, W.; Ando, K.; Maekawa, S.; Saitoh, E. *Nature* **2008,** 455, (7214), 778-781.

13. Zheng, X.; Zheng, W.; Wei, Y.; Zeng, Z.; Wang, J. *The Journal of chemical physics* **2004,** 121, (17), 8537-8541.
14. Paulsson, M.; Datta, S. *Physical review B* **2003,** 67, (24), 241403.
15. Algharagholy, L. A.; Al-Galiby, Q.; Marhoon, H. A.; Sadeghi, H.; Abduljalil, H. M.; Lambert, C. J. *Nanotechnology* **2015,** 26, (47), 475401.
16. Wierzbicki, M.; Świrkowicz, R. *Journal of Physics: Condensed Matter* **2010,** 22, (18), 185302.
17. Lau, C. S.; Sadeghi, H.; Rogers, G.; Sangtarash, S.; Dallas, P.; Porfyrakis, K.; Warner, J.; Lambert, C. J.; Briggs, G. A. D.; Mol, J. A. *Nano letters* **2015,** 16, (1), 170-176.
18. Zimbovskaya, N. A. *Journal of Physics: Condensed Matter* **2014,** 26, (27), 275303.
19. Sadeghi, H.; Sangtarash, S.; Lambert, C. J. *Beilstein journal of nanotechnology* **2015,** 6, (1), 1176-1182.
20. Sadeghi, H.; Sangtarash, S.; Lambert, C. J. *Nano letters* **2015,** 15, (11), 7467-7472.
21. Wang, R. Y.; Segalman, R. A.; Majumdar, A. *Applied Physics Letters* **2006,** 89, (17), 173113.
22. Sedghi, G.; García-Suárez, V. M.; Esdaile, L. J.; Anderson, H. L.; Lambert, C. J.; Martín, S.; Bethell, D.; Higgins, S. J.; Elliott, M.; Bennett, N. *Nature nanotechnology* **2011,** 6, (8), 517-523.
23. Stibrany, R. T.; Vasudevan, J.; Knapp, S.; Potenza, J. A.; Emge, T.; Schugar, H. J. *Journal of the American Chemical Society* **1996,** 118, (16), 3980-3981.
24. Vasudevan, J.; Stibrany, R. T.; Bumby, J.; Knapp, S.; Potenza, J. A.; Emge, T. J.; Schugar, H. J. *Journal of the American Chemical Society* **1996,** 118, (46), 11676-11677.
25. Burrell, A. K.; Officer, D. L.; Plieger, P. G.; Reid, D. C. *Chemical reviews* **2001,** 101, (9), 2751-2796.
26. Beletskaya, I.; Tyurin, V. S.; Tsivadze, A. Y.; Guilard, R.; Stern, C. *Chemical reviews* **2009,** 109, (5), 1659-1713.

27. Cheng, K. F.; Drain, C. M.; Grohmann, K. *Inorganic chemistry* **2003,** 42, (6), 2075-2083.
28. Soler, J. M.; Artacho, E.; Gale, J. D.; García, A.; Junquera, J.; Ordejón, P.; Sánchez-Portal, D. *Journal of Physics: Condensed Matter* **2002,** 14, (11), 2745.
29. Ferrer, J.; Lambert, C. J.; García-Suárez, V. M.; Manrique, D. Z.; Visontai, D.; Oroszlany, L.; Rodríguez-Ferradás, R.; Grace, I.; Bailey, S.; Gillemot, K. *New Journal of Physics* **2014,** 16, (9), 093029.
30. Perdew, J. P.; Burke, K.; Ernzerhof, M. *Physical Review Letters* **1996,** 77, (18), 3865.
31. Hammer, B.; Hansen, L. B.; Nørskov, J. K. *Physical review B* **1999,** 59, (11), 7413.

Chapter 7

Conclusions and Future Works

In conclusion, I have studied electronic and thermoelectric properties of single organic molecules (metallo-porphyrins) in different structures. In the chapter 4 in collaboration with University of Barcelona I investigate the transport properties of M(II)-5,15-diphenylporphyrin (M-DPP) single-molecule junctions (M=Co, Ni, Cu, or Zn divalent metal ions), in which the current flows perpendicular to the plane of the porphyrin. Novel STM-based conductance measurements combined with quantum transport calculations demonstrate that current-perpendicular-to-the-plane (CPP) junctions have three-orders-of-magnitude higher electrical conductances than their currentin-plane (CIP) counterparts, ranging from 2.10−2 G0 for Ni-DPP up to 8.10−2 G0 for Zn-DPP. The metal ion in the center of the DPP skeletons is strongly coordinated with the nitrogens of the pyridyl coated electrodes, with a binding energy that is sensitive to the choice of metal ion. I find that the binding energies of Zn-DPP and Co-DPP are significantly higher than those of Ni-DPP and Cu-DPP. Therefore when combined with its higher conductance, I identify Zn-DPP as the favoured candidate for high-conductance CPP single-molecule devices.

CHAPTER 7. CONCLUSIONS AND FUTURE WORKS

In chapter 5, I investigated the thermoelectric properties of a unique porphyrin based family of flat-stacked 5,15-diphenylporphyrins (DPP) molecular wires, where a divalent metal ion is coordinated by the pyridine blocks in the center of the porphyrin skeleton which allows the thermoelectric properties to be tuned by the divalent metal substitution. By varying the transition metal-centre over the family Ni, Co, Cu, and Zn I was able to tune the molecular energy levels relative to the Fermi energy of the electrodes. The room-temperature Seebeck coefficients of these junctions are rather high, ranging from 90 μV/K for Cu, Co and Ni-porphyrins to -23 μV/K for Zn-porphyrin at the DFT-predicted Fermi energy. These values could be further increased by decreasing molecular energy levels relative to the Fermi energy. In addition, the main source of the thermal conductance in these junctions in the vicinity of the DFT Fermi energy is due to phonons. Furthermore, changing the metal atom has little effect on the thermal conductance due to the phonons. The thermopower, thermal and electrical conductance are combine to yield the room-temperature values of ZT ranging from 1.6 for Cu porphyrin to ~ 0.02 for Ni-porphyrin. In chapter 6 I compared thermoelectric properties of three zinc porphyrin (ZnP) dimers and a ZnP monomer and found that the "edge-over-edge" dimer formed from stacked ZnP rings possesses a high electrical conductance, negligible phonon thermal conductance and a high Seebeck coefficient of order 300 μV/K. These combine to yield a room-temperature figure of merit of ZT≈4, which is the highest room-temperature ZT ever reported for an organic material. This high value of ZT is a consequence of the low phonon thermal conductance arising from the stacked nature of the porphyrin rings, which hinders phonon transport through the edge-over-edge molecule and enhances the Seebeck coefficient.

CHAPTER 7. CONCLUSIONS AND FUTURE WORKS

The work presented in this thesis has aimed to identify and investigate molecules exhibiting high-performance thermoelectricity. Comparison with the literature suggests that porphyrins can perform much better than molecules investigated to date. For example thiol-terminated molecules typically exhibit HOMO-dominated transport and a positive S, ranging from 6.8 to 2.4 μV/K for n-alkanedithiols, depending on the length n[1,2] , from 7 μV/K to 16 μV/K for n-benzenedithiols, depending on the number n of phenyl rings, ranging from 7 μV/K to 16 μV/K[3-9]. Positive Seebeck coefficients up to to 24 μV/K were measured for 1,4-Bis((trimethylstannyl)methyl)-n-phenyl (n=1,2,3,4), up to 10.4 μV/K[1,10,11] for 1,4-n-Phenylenediamine (PDA) (n-1,2,3) and as high as 14.8 μV/K for oligothiophenes on gold[12]. On the other hand pyridyl terminal groups promote LUMO-dominated transport leading to negative Seebeck coefficients as high as -9 μV/K and -10 μV/K respectively[11,13] 4,4'-for bipyridine and 1,2-di(4-pyridyl)ethylene respectively. Fullerenes also exhibit negative Seebeck coefficients, ranging from -10 to -30 μV/K for C_{60}[14] to -33 μV/K for C_{60} dimers[15] and up to -31.6 μV/K C_{82} endohedral fullerenes[16]. The sign of the endohedral fullerene Sc3N@C_{80} was shown to be sensitive to pressure, ranging from -25 μV/K to +25 μV/K, depending on the orientation of the molecule on a gold substrate[17].

For the future it would be of interest to explore other factors which control thermoelectric performance. For example, although most of the above studies used gold electrodes, alternative choices could include graphene[18,19], silicene[20,21], platinum[22], palladium[22], iron[23] and nickel[24], which provide a range of Debye frequencies for controlling phonon transport across the electrode-molecule boundary[24]. Systematic modification of the geometry of a molecule is known to control electrical conductance and may also be a useful method of

controlling thermoelectricity[25]. Finally the question of how to utilise molecular-scale thermoelectricity in real devices needs to be addressed, where disorder in the electrodes is inevitable[26]. One potential route is to form self-assembled monolayers of molecules, whose single-molecule thermoelectric properties have been assessed using the methods presented in this thesis. The question of how such properties translate into molecular films is a completely open question and likely to be a topic of intense interest in the future years.

Bibliography

1. J. A. Malen *et al.*, Nano Lett. **9**, 1164(2009).
2. S. Y. Guo, G. Zhou, and N. J. Tao, Nano Lett. **13**, 4326(2013).
3. A. Tan, S. Sadat, and P. Reddy, Appl. Phys. Lett. **96**, 013110(2010).
4. A. Tan *et al.*, J. Am. Chem. Soc. **133**, 8838(2011).
5. S. K. Lee *et al.*, Nano Lett **14**, 5276(2014).
6. Y. Kim *et al.*, Appl. Phys. Lett. **109**, 033102(2016).
7. M. Tsutsui, M. Taniguchi, and T. Kawai, Nano Lett. **8**, 3293(2008).
8. T. Morikawa *et al.*, Nanoscale **6**, 8235(2014).
9. S. Kaneko *et al.*, Applied Physics Express **8**, 095503(2015).
10. D. Kim, P. S. Yoo, and T. Kim, Journal of the Korean Physical Society **66**, 602(2015).
11. T. Kim *et al.*, Nano Lett. **14**, 794(2014).
12. W. B. Chang *et al.*, Chemistry of Materials **26**, 7229(2014).
13. J. R. Widawsky *et al.*, Nano Lett. **12**, 354(2012).
14. S. K. Yee *et al.*, Nano Lett. **11**, 4089(2011).
15. C. Evangeli *et al.*, Nano Lett. **13**, 2141(2013).
16. S. K. Lee *et al.*, Nanoscale **7**, 20497(2015).
17. L. Rincon-Garcia *et al.*, Nat. Mater. **15**, 289(2016).
18. H. Sadeghi, H.; Mol, J.; Lau, C.; Briggs, G. A. D.; Warner, J.; Lambert, C. J., *PNAS* ***9,*** 2658-2663 (2015)
19. C.S Lau, et al. *Nano Letters* **16**, 170-176 (2016)
20. H Sadeghi, S Bailey, C.J. Lambert, *App. Phys. Lett.* **104** (10), 103104 (2014)
21. H. Sadeghi, S. Sangtarash, C.J. Lambert, *Scientific Reports **5***, 9514 (2015)
22. V. M. García-Suárez, A. R. Rocha, S. W. Bailey, C. J. Lambert, S. Sanvito, J. Ferrer, *Phys. Rev*. **B72** 045437 (2005)
23. V M García-Suárez, C M Newman, C. J. Lambert, J M Pruneda and J Ferrer, *J. Phys.: Condens. Matter* **16** 5453 (2004)

24. H Sadeghi, S Sangtarash and CJ Lambert, *Nano Letters* **15**, 7467-7472 (2015)

25. C. M. Finch, S. Sirichantaropass, et al., *J. Phys. Condens. Matt*. 20, 022203 (2008)

26. C.J. Lambert and D. Weaire, *Metallography* 14, 307 (1981)